University of Nevada, Reno

Formation, Growth, and Interactions of Tension Twins in Magnesium

A dissertation submitted in partial fulfillment of the

requirements for the degree of

Doctor of Philosophy in Mechanical Engineering

by

Duke Culbertson

Dr. Yanyao Jiang/Dissertation Advisor

May, 2021

THE GRADUATE SCHOOL

We recommend that the dissertation
prepared under our supervision by

DUKE CULBERTSON

entitled

Formation, Growth, and Interactions of Tension Twins in Magnesium

be accepted in partial fulfillment of the
requirements for the degree of

DOCTOR OF PHILOSOPHY

Yanyao Jiang, Ph.D.
Advisor

Matteo Aureli, Ph.D.
Committee Member

Pradeep Menezes, Ph.D.
Committee Member

Bin Li, Ph.D.
Committee Member

Dhanesh Chandra, Ph.D.
Graduate School Representative

David W. Zeh, Ph.D., Dean
Graduate School

May, 2021

Abstract

In the world of structural metals, magnesium and its alloys are much lighter than other traditionally used metals having a density of ~1/5 that of iron and ~2/3 that of aluminum – two commonly used metals. Unlike these isotropic cubic metals, magnesium has a hexagonal closed-packed (hcp) crystal structure and is not commonly used. The hcp structure has less symmetry than the face centered and body centered cubic structures, resulting in an anisotropic mechanical response with fewer available slip systems. *C*-axis deformation is particularly difficult to achieve through dislocation slip at room temperature. To accommodate deformation, tension twinning is activated, which rotates the crystal by almost 90° to better allow the easily activated basal {0001} slip system. As the microstructure dynamically changes by twinning during plastic deformation, so too do the local deformation processes. The microstructural evolution directly affects the mechanical behavior of magnesium under both monotonic and cyclic loading. To better design, process, and utilize the magnesium alloys in engineering applications, a fundamental understanding of the process of twinning and twin-twin interactions is required. The current research aims to capture and explain the microstructural evolution due to twinning during tension, compression, torsion, and uniaxial strain path changes.

The nucleation, growth, and interaction of tension twins were directly observed utilizing a hybrid *in situ* optical microscopy, *ex situ* electron backscatter diffraction procedure. Cross-grain twin pair formation was captured in extruded pure polycrystalline magnesium where the twin in one grain assists in the nucleation of a similar twin in the adjacent grain. Two assisted formation processes were observed: the commonly observed

twin propagation-assisted and the newly recorded twin thickening-assisted mechanisms. A twin chain spanning seven grains was rapidly developed through the twin propagation-assisted mechanism of two smaller chains and eventual conjoining within a middle grain. The two smaller chains form across grains with small misorientations from grain to grain, allowing for easy-cross grain twin formation by a twin-propagation assisted process. In the middle grain where the chains connect, the same twin variant is formed from both chains on either side of the grain, where they both grow and coalesce forming the larger twin chain. The new twin thickening-assisted formation is observed for the first time where the paired twin is formed across a grain boundary by the other twin thickening.

Applying the hybrid testing procedure to nearly *c*-axis tension of single-crystalline pure magnesium reveals that basal slip is activated prior to the nucleation of tension twins. As twinning increases with increasing strain, the initial basal slip bands are deflected within the twinned region relative to the activated variant and the twinning shear. By the final plastic strain of 3.83%, all six tension twin variants are identified within the observed area along with all three types of twin-twin interactions: Type I co-zone, Type II(a) non-co-zone, and Type II(b) non-co-zone. A needle-like Type I interaction is captured by *in situ* observation for the first time. The initial interaction results in the normally occurring impinging and acute angle twin-twin boundary. On the obtuse angle side, twinning dislocations are deposited near the impinging twin-twin boundary, leading to incoherent curving twin boundaries. The combination of the acute angle twin-twin boundary and incoherent boundaries on the obtuse angle side result in the penetrating structure. Partial

penetrating structures are observed in the Type II interactions, along with secondary twinning. Detwinning is quantitatively measured during unloading.

Twinning behavior during strain path change and torsional loading was examined using extruded pure polycrystalline magnesium. Compression parallel to the extrusion direction of the bar results in severe twinning up to 95% of its volume by exhaustion. Using companion specimens, pre-compression was applied to -7.3% and -12.8% strains to induce varying twin severity prior to re-loading in tension. The subsequent tension reveals a combination of detwinning and secondary tension twinning of the initial twins formed during compression. Detwinning is more significant than secondary twinning in the -7.3% pre-strain case while the opposite is observed in the -12.8% pre-strain case. After detwinning is exhausted, non-Schmid factor twins are observed along with the retained secondary twins. Twinning during free-end torsion about the extrusion direction cannot reach the same global twin severity as compression as the texture is not entirely favorable for twinning. Grains favorably oriented for tension twinning are severely twinned. Less favorably oriented grains show high variability in terms of twin severity, while the unfavorably oriented grains show very little to some twinning. All six variants are observed in multiple grains, and more significantly, some twinned regions are highly favorable for further twinning, so secondary twinning is very common. By torsional failure, favorable secondary twins can be found fully encompassing their primary variant.

Dedication

To my loving and supportive mother Ms. Lisa Zambrano.

Acknowledgements

First, I would like to express my utmost respect and gratitude to my advisor, Dr. Yanyao Jiang. Over the past 6 years, Dr. Jiang has been an incredible mentor for me, providing the necessary guidance while also allowing me to gain the experience needed to develop my skills and knowledge. His scientific curiosity, insatiable thirst for knowledge, and enthusiastic work ethic have made an indelible impact on my life and professional values. The experience I have gained working under Dr. Jiang will benefit my future career, wherever that path may take me.

Second, I would like to acknowledge Dr. Qin Yu, who has not only been a great collaborator, but also a great friend. His insight and intuition during our discussions have been an invaluable asset in both my academic and personal development. I would not be where I am now without Dr. Jiang and Dr. Yu. My sincere thanks also go to Dr. Bin Li, who has assisted me throughout my program when it comes to magnesium. I greatly appreciate the collaboration and discussions we have had over the years, and for his service in my dissertation committee. I also want to sincerely thank Dr. Dhanesh Chandra, Dr. Matteo Aureli, and Dr. Pradeep Menezes for their advice and for serving as the dissertation committee members. I also want to thank Dr. Feifei Fan for allowing the use of the digital microscope in her lab.

Additionally, I would like to thank the machine shop technicians Mr. Ferrill “Tony” Berendsen (former), Mr. Seth Draper, and Mr. Brian Nagy for their help in machining almost everything for us – specimens, testing grips, stages, etc. I also thank Dr. Joel

Desormeau, the Geosciences lab manager in charge of the SEM, for his assistance in the operation of the SEM and EBSD.

Outside of the research, I would like to thank Dr. Angelina Padilla. As a teaching assistant working under Dr. Padilla, I had the opportunity to experience hands-on teaching with hundreds of students, which has been among my favorite experiences at UNR. It helped develop my public speaking skills immensely and has changed the way I approach presentations. I also want to thank the current and former members of our research group especially Luiz Carneiro, Yuqian Wang, Chris Yocom, Aidan Dolan, and Ryan Wang. I have thoroughly enjoyed our time spent together, and I hope you have as well. I consider you all friends.

Finally, I would like to thank my beloved family and friends. Most of all to my parents, I owe immeasurable gratitude for their unconditional love, support, and sacrifice that has allowed me the freedom to pursue this path in life.

Table of Contents

List of Tables

List of Figures

1 Introduction

Magnesium, a hexagonal closed-packed (hcp) crystal structured metal, and its alloys are very tempting structural materials in engineering, especially in automotive and aerospace industries [1–4]. These materials are lightweight compared to their commonly used cubic metal counterparts like iron-based steels and aluminum alloys [1,5]. Comparing densities, magnesium has the lowest density of the structural metals with a value of 1.74 g/cm^3 while iron and aluminum have densities of 7.87 g/cm^3 and 2.7 g/cm^3, respectively. Titanium, a popular hcp metal, has a density of 4.5 g/cm^3. However, despite this weight benefit, magnesium does not have many significant applications as a structural material in industry due to some material difficulties.

While the primary issues with magnesium are its flammability and low corrosion resistance, it has some difficulties related to its mechanics as well. Components are formed by two common methods: casting and deformation processes. Casting is a commonly used method [6], but it yields defects like voids that hamper the yield strength, micro-hardness, and fatigue resistance of the material [7]. Alternatively, deformation processes, or more commonly phrased as wrought, magnesium is subjected to processes like extrusion, rolling, and forging, which form a strong texture and eliminate issues relating the defects often found in their cast counterparts [1,5]. As a result, the wrought materials possess superior mechanical strength and fatigue resistance [8,9]. Despite these benefits, wrought magnesium comes with difficulties relating to its low ductility and poor formability at room temperature [1,5]. These challenges are a direct result of the hcp crystal structure. Cubic

metals, like iron and aluminum, are treated as isotropic materials due to the high symmetry of the cubic crystal structures. This symmetry allows for multiple deformation systems to accommodate strain in just about any direction. Alternatively, the hcp structure has less symmetry and fewer available slip systems as a result. Deformation along the *c*-axis of the hcp crystal is particularly challenging, with the only slip system capable of *c*-axis deformation having a large critical resolved shear stress at room temperature. Thus, twinning is one of the most important mechanisms in magnesium and its understanding vital in its ability to be used in structural components.

1.1 Significance and Motivation

To better use magnesium as an engineering material, its deformation mechanisms, especially twinning, must be better understood. Extensive studies have been conducted over the past three decades on twinning in magnesium ranging in scale from sub-microscale nucleation and propagation to macroscale mechanical response. More recently, a significant emphasis has been made on modeling twinning and its effects on the material's mechanical behavior. Atomistic and molecular dynamic simulations have predicted the nucleation, propagation, thickening, and interactions of twins in a controlled space. These findings are then compared to what has been observed in experimental works. However, many of these experimental works are done by *ex situ*, post-mortem methods, thus lacking real-time information. At the macroscale, modeling methods like the elastic viscoplastic self-consistent model are being used to predict and replicate the mechanical response of these materials. At both scales, there is a distinct lack of detailed microstructural analysis of twinning during the deformation process. At the micron-scale, *in situ* works attempting

to capture live evidence of the deformation process can follow a single area but operate on interrupted loading, thus will miss the details between loading steps. Well-designed experiments that can capture live deformation *in situ* while still allowing characterization is required to adequately capture key twinning phenomena. Physical evidence can support or further the findings of both simulation and *ex situ* observation. At the macroscale, localized *in situ* observation cannot be used to explain the global material response. There have been many studies that explain the twinning phenomenon at the global material scale under both tension and compression. However, there are very limited studies that explore the microstructural evolution during more advanced loadings. When it comes to reversed loading and free-end torsion, no studies have been conducted that examine the detailed microstructural evolution due to twinning.

1.2 Research Objectives and Outlines

The current research aims to investigate the development of the $\{10\bar{1}2\}$ tension twin system and its associated mechanisms under different twin-favorable loading conditions. A focus is placed on fundamentally understanding and expanding on key twinning mechanisms such as nucleation, propagation, thickening, detwinning, and the interaction between different variants. The following goals are expected to be achieved:

1. To clarify the development of both old and new types of twin structures using *in situ* observation in conjunction with *ex situ* analyses
2. To quantitatively study the three key single twin processes: nucleation, propagation, and thickening

3. To record the interactions between twins and the nucleation of paired twins at grain boundaries
4. To analyze the general twinning process during reversed and torsional loading paths

To achieve these goals, research efforts will be split into two interrelated parts: mechanical testing and microscopic characterization. A hybrid *in situ* optical microscopy (OM), *ex situ* electron backscatter diffraction (EBSD) method will be applied to both extruded pure polycrystalline and single-crystalline magnesium favorable for tension twinning by tension. This method allows direct visual observation of twin evolution while still allowing orientation characterization by EBSD. The polycrystalline material will provide insight into the interaction between twins and grain boundaries. The single-crystalline material allows for a fundamental study of twinning devoid of grain boundaries and their effects on local stresses. Compression-tension reversed loading and free-end torsion experiments are conducted on extruded pure polycrystalline magnesium. Companion specimens are utilized to characterize microstructures at intermediate strains using EBSD. Sequencing EBSD maps allow for general microstructural evolution investigation, but lack direct, real-time observation.

The main content of this dissertation is divided into five parts:

1. The first part, Chapter two, reviews the fundamental information about magnesium including crystallography, primary deformation mechanics, and their effects on the material's mechanical response. More advanced topics related to secondary twinning, tertiary twinning, and twin-twin interactions are included in the second half of this chapter.

2. In the second part, a hybrid *in situ* OM, *ex situ* EBSD testing procedure is developed to better capture and clarify twinning processes. Chapter three describes this method and applies it in the study of cross-grain twin pair formation in polycrystalline magnesium. Two paired twin nucleation methods are detailed using *in situ* observation and *ex situ* characterization. Favorability of cross-grain twin pair formation is explained using Schmid factor and a geometric compatibility factor. Most of this chapter is adapted from [10]. Chapter four applies this newly developed hybrid testing procedure to monotonic tension testing of single crystal magnesium almost parallel to its *c*-axis. Twin nucleation, growth, thickening, and interactions are both quantitatively and qualitatively examined. Twin-twin interaction processes, previously studied by *ex situ* methods, are clarified with *in situ* results. Some of this chapter is adapted from [11].
3. The third part, Chapter five, will explore the effect of reversed strain path change and monotonic torsion on the microstructural and texture evolution of polycrystalline pure magnesium. The effect of twins formed during pre-compression on the microstructural evolution in tension will be examined. This work was adapted from [12]. Torsion and its favorability for twinning will be clarified and compared with tension and compression. Grains highlighting the variability of twinning based on favorability will be presented and discussed.
4. The fifth part, Chapter six, summarizes the conclusions of the research. Recommendations for future research related to the current findings are outlined.

2 Literature Review

2.1 Crystallography of Magnesium

Magnesium and its hcp crystal structure are visualized in Figure 1 [13]. When working with hexagonal unit cells, four basis vectors a_1, a_2, a_3, and c and two lattice parameters **a** and **c** are used. For magnesium, these lattice parameters **a** and **c** are 3.2094 Å and 5.2108 Å, respectively. The **c**/**a** ratio, or the close-packing of the spherical atoms, for magnesium is 1.624, which is smaller than the ideal hcp ratio of $\sqrt{8/3}$ = 1.633 [14]. The **c**/**a** ratio, compared to the hcp metal of study, affects the twinning characteristics such as the possible twin systems, twin direction, and magnitude of shear.

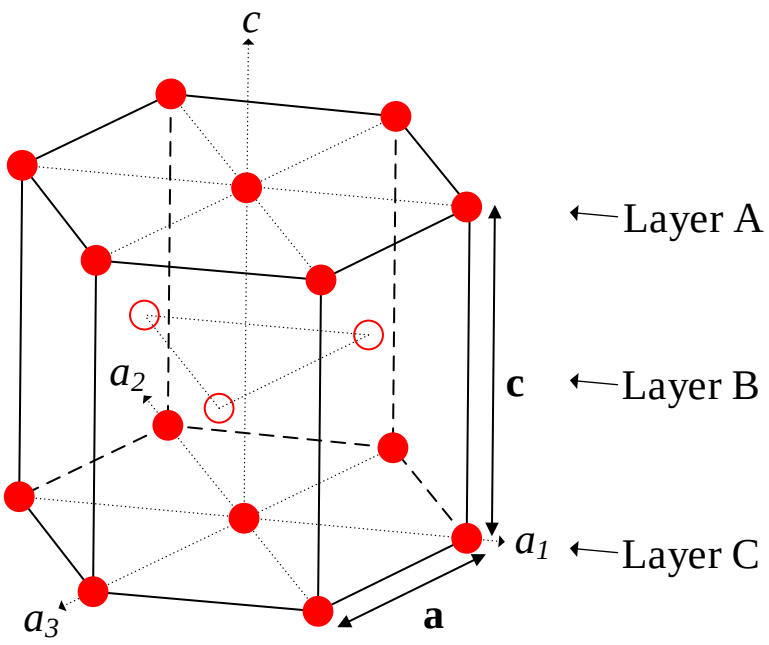

Figure 1**:** Three-dimensional hexagonal closed-packed crystal structure based on the a_1, a_2, a_3, and c basis vectors [13]. For magnesium, **a** is 3.2094 Å and **c** is 5.2108 Å.

Atoms are situated at the center and at each corner of the hexagonal base, as shown as the solid dots in Figure 1. There are three close-packed atoms per unit, with the first one located at $\frac{2}{3}, \frac{1}{3}, \frac{1}{2}$, and the other two at ±120° about the *c*-axis. These three atoms are shown has hollow dots in Figure 1. Assuming each atom, and thus dot, as a solid sphere, the stacking sequence of the hcp crystal is -ABA-.

There are three important zone axes in magnesium [13] that can be based on a three-axis rhombohedral system. These axes are the *a*-axis $\langle \bar{1}2\bar{1}0 \rangle$, prismatic *b*-axis $\langle 10\bar{1}0 \rangle$, and the basal *c*-axis $\langle 0001 \rangle$, respectively, and are shown in Figure 2a. The $\langle \bar{1}2\bar{1}0 \rangle$ zone axis is parallel to the *a*-axes in the hexagonal basis, and its zone encompasses the $\{10\bar{1}n\}$ planes (Figure 2b). The prismatic $\langle 10\bar{1}0 \rangle$ zone axis contains the $\{1\bar{2}1n\}$ planes (Figure 2c). The basal $\langle 0001 \rangle$ zone axis is parallel to the *c*-axis of the unit cell. Its zone encompasses all $\{hki0\}$ planes that are perpendicular to the basal plane. The family of planes related to these key zone axes is significant due to their relationship with the deformation mechanics of magnesium.

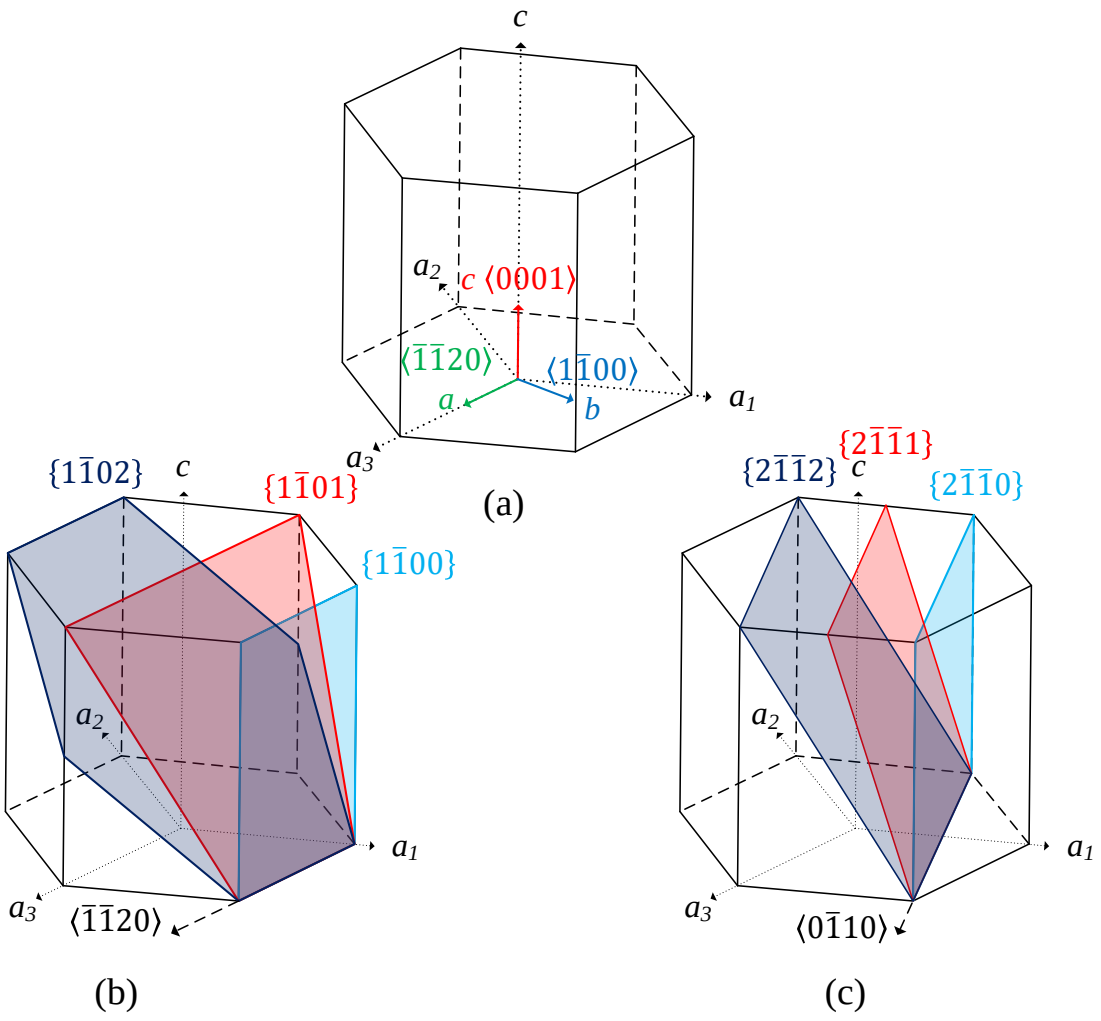

Figure 2: The three important zone axes and their zone planes in magnesium [13]: (a) the three important zone axes - basal ⟨0001⟩, prismatic ⟨1$\bar{1}$00⟩, and the *a*-axis ⟨$\bar{1}\bar{1}$20⟩ relative to the hexagonal unit cell; (b) the *a*-axis ⟨$\bar{1}$2$\bar{1}$0⟩ zone axis and some of its associated {10$\bar{1}n$} zone planes; (c) the prismatic ⟨10$\bar{1}$0⟩ zone axis and some of its associated {1$\bar{2}$1n} zone planes

2.2 Deformation Mechanisms in Magnesium

2.2.1 Dislocation Slip

It is commonly accepted that five independent slip systems are required for polycrystalline materials to undergo homogeneous deformation based on the von Mises criterion [15,16]. However, because of magnesium's hcp structure, it has a reduced number of available slip systems.

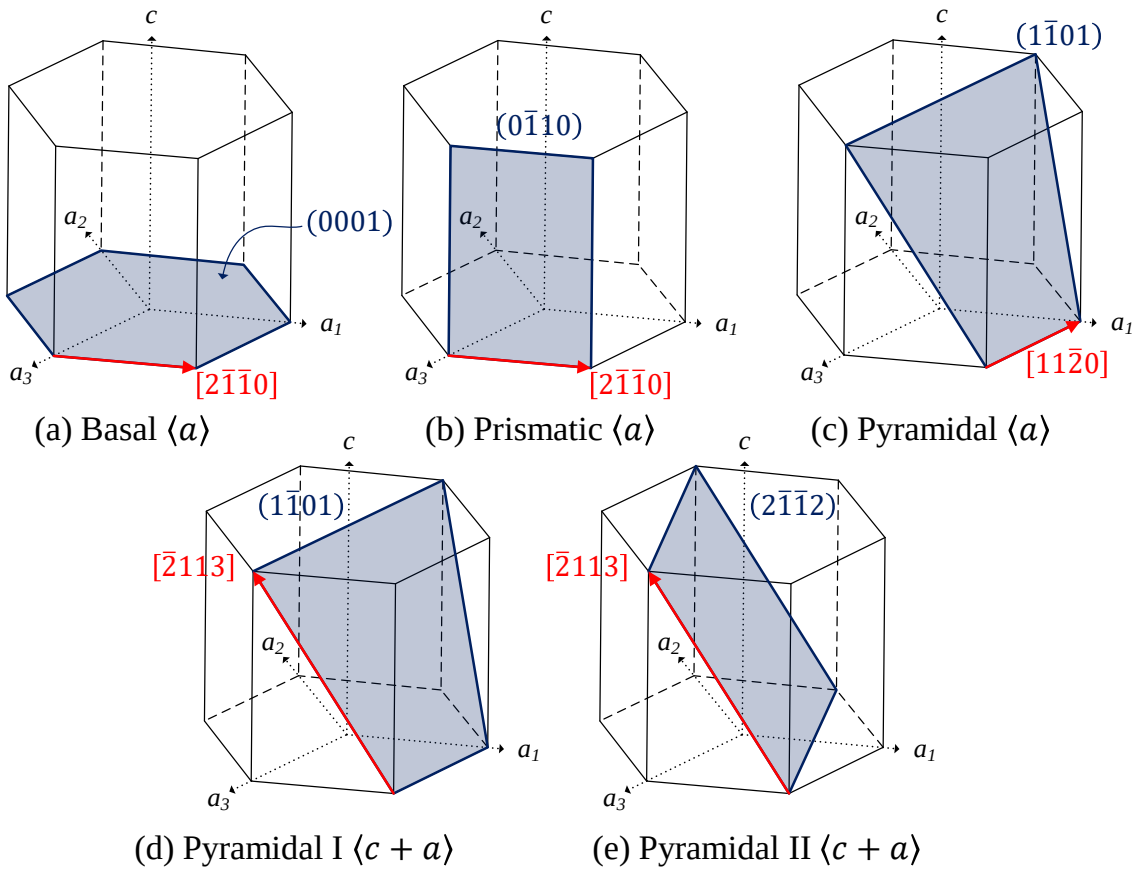

Figure 3: The five typical slip systems in magnesium [13,16,17]: (a) basal ⟨a⟩ - {0001} ⟨$\bar{2}$110⟩; (b) prismatic ⟨a⟩ - {10$\bar{1}$0} ⟨$\bar{2}$110⟩; (c) first-order pyramidal ⟨a⟩ - {01$\bar{1}$1} ⟨$\bar{2}$110⟩; (d) first-order pyramidal ⟨$c + a$⟩ - {1$\bar{1}$01} ⟨$\bar{2}$113⟩; and (e) second-order pyramidal ⟨$c + a$⟩ - {2$\bar{1}\bar{1}$2} ⟨2$\bar{1}\bar{1}$3⟩

Table 1: The four typical slip systems and their critical resolved shear stress in magnesium at room temperature [13,16,18]

Burgers vector type	Slip System	Slip plane	Slip direction	CRSS (MPa) at 300 °K
$\langle a \rangle$	Basal	$\{0001\}$	$\langle \bar{2}110 \rangle$	0.45-1.07 [18–22]
	Prismatic	$\{10\bar{1}0\}$	$\langle \bar{2}110 \rangle$	~8 [23] ~18 [24] 39.2 [25]
	First-order pyramidal	$\{10\bar{1}1\}$	$\langle \bar{2}110 \rangle$	0.51 [18] 3.92 [19]
$\langle c + a \rangle$	First-order pyramidal	$\{10\bar{1}1\}$	$\langle \bar{1}\bar{1}23 \rangle$	54 [17]
	Second-order pyramidal	$\{11\bar{2}2\}$	$\langle \bar{1}\bar{1}23 \rangle$	~40 [26]

Magnesium has a potential five slip systems as shown in Figure 3. These systems are associated with a lattice shear in which slip dislocations move on a slip plane in a slip direction. Examination of the five systems reveals that three systems can only accommodate deformation within the basal plane. Comparing the experimentally acquired critical resolved shear stress (CRSS) values for the slip systems in Table 1, basal slip (Figure 3a) is the easiest $\langle a \rangle$ system to activate at room temperature, requiring only 0.5-1 MPa resolved shear stress. This system slips on the basal $\{0001\}$ plane in the three principle $\langle a \rangle$ directions. Prismatic slip (Figure 3b) also occurs along $\langle a \rangle$, but on the prismatic $\{10\bar{1}0\}$ planes. However, prismatic slip is more difficult to activate than the basal system. Experimental studies on single-crystal magnesium have revealed that the CRSS for the prismatic slip is roughly 40-100 times more than the basal system [13,25]. The first-order pyramidal $\langle a \rangle$ slip (Figure 3c), occurring on the $\{10\bar{1}1\}$ plane, is the second non-

basal $\langle a \rangle$ slip system. Crystallographically this system is equivalent to the combined modes by cross slip between the basal and prismatic systems [16]. However, as previously stated, these three $\langle a \rangle$ systems only accommodate strain in the $\langle a \rangle$ directions and not along the *c*-axis.

There are two additional slip systems, both of which can accommodate *c*-axis deformation – the first-order pyramidal (Figure 3d) and second-order pyramidal (Figure 3e) $\langle c + a \rangle$ systems. At room temperature, both systems have large CRSS values greater than 40 MPa. Thus, instead of these non-basal $\langle c + a \rangle$ systems, tension twinning is often activated with a much lower CRSS of ~ 2.5 MPa [27], assisting in satisfying the von Mises criterion.

2.2.2 Twinning

With the reduced number of slip systems in the hcp structure, twinning is an important deformation system for hcp crystals. Like slip, deformation by twinning is achieved through a lattice shear. Though, unlike in slip where the shear deformation occurs locally on the discrete slip planes, twinning shear occurs over the uniformly deformed region [28]. Additionally, twinning is polar in nature and occurs only in one direction, unlike slip [29]. Details of the crystallographic elements associated to twinning has previously been reported [13,14,30]. The four twinning elements relative the shear plane, P, are shown schematically in Figure 4.

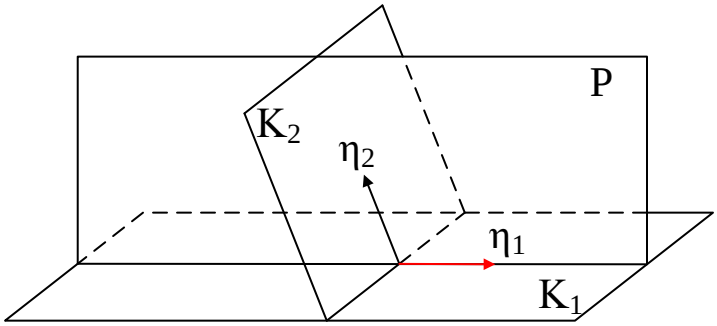

Figure 4: The four twinning elements related to the plane of shear, P [14].

The twin plane and its corresponding twin direction are labeled K_1 and η_1, respectively. The conjugate, or reciprocal, twin plane and direction are labeled K_2 and η_2, respectively. The shear plane contains both twin directions and the twin plane normals. With K_1 and η_1 as the twinning plane and direction, twinning shear is applied on the plane K_1 in the η_1 direction, which results in the twinning/rotation of the reciprocal twin plane and direction. This rotation due to shear does not distort either plane or direction. From this simple rotation, the magnitude of the twinning shear, s, can be calculated from the acute angle between K_1 and K_2 using the following equation:

$$s = 2\cot \measuredangle(K_1, K_2) \tag{1}$$

Table 2 provides the twin planes and directions for the commonly observed $\{10\bar{1}2\}$ (first row of Table 2) and $\{10\bar{1}1\}$ (second row of Table 2) twinning, along with their corresponding shear magnitudes and CRSS values. Both commonly observed twinning systems can accommodate strain along the *c*-axis of the magnesium crystal. Noting the small CRSS for the $\{10\bar{1}2\}$ twin system, *c*-axis deformation is far easier to occur by $\{10\bar{1}2\}$ twinning than by pyramidal $\langle c + a \rangle$ slip or by $\{10\bar{1}1\}$ twinning. As such, basal $\langle a \rangle$ slip and

"tension" $\{10\bar{1}2\}$ twinning, with their small CRSS values, play the largest roles in accommodating plastic deformation of magnesium and its alloys.

Table 2: The elements that define the commonly observed twinning mechanisms in magnesium [14]

K_1	η_1	K_2	η_2	Twin shear, s (γ =1.624 for Mg)	CRSS (MPa) at 300 °K
$\{10\bar{1}2\}$	$\langle\bar{1}011\rangle$	$\{10\bar{1}\bar{2}\}$	$\langle10\bar{1}1\rangle$	$\frac{\lvert\gamma^2-3\rvert}{\gamma\sqrt{3}} = 0.129$	2 [31] 2.4 [27] 2.7-2.8 [32] 5.5 [23]
$\{10\bar{1}1\}$	$\langle10\bar{1}\bar{2}\rangle$	$\{10\bar{1}\bar{3}\}$	$\langle30\bar{3}2\rangle$	$\frac{4\gamma^2-9}{4\gamma\sqrt{3}} = 0.138$	75-130 [24] 114 [33]

Figure 5 shows the two twin systems relative to the hcp crystal. Both twin systems have six crystallographically equivalent variants by symmetry about the crystal's *c*-axis. Because the **c**/**a** ratio for magnesium is less than $\sqrt{8/3}$, the $\{10\bar{1}2\}$ system favors extension along the *c*-axis, thus is considered a "tension," or extension, twin [13,14,16]. Crystal reorientation by tension twinning results in a rotation of 86.3° about the $\langle1\bar{2}10\rangle$ zone axis from the original, untwinned material. Alternatively, the $\{10\bar{1}1\}$ favors the contraction of the *c*-axis and is thus called a "compression" twin. This system results in a crystal rotation of 56.15° about the $\langle1\bar{2}10\rangle$ zone axis. With both systems, the crystal reorientation allows for additional strain accommodation by newly favorable secondary slipping or twinning [34]. For example, tension parallel to the *c*-axis of the magnesium hcp crystal favors

tension twinning but not basal slip. After twinning has occurred to a significant amount, the twinned crystal will be favorable for further deformation by basal slip.

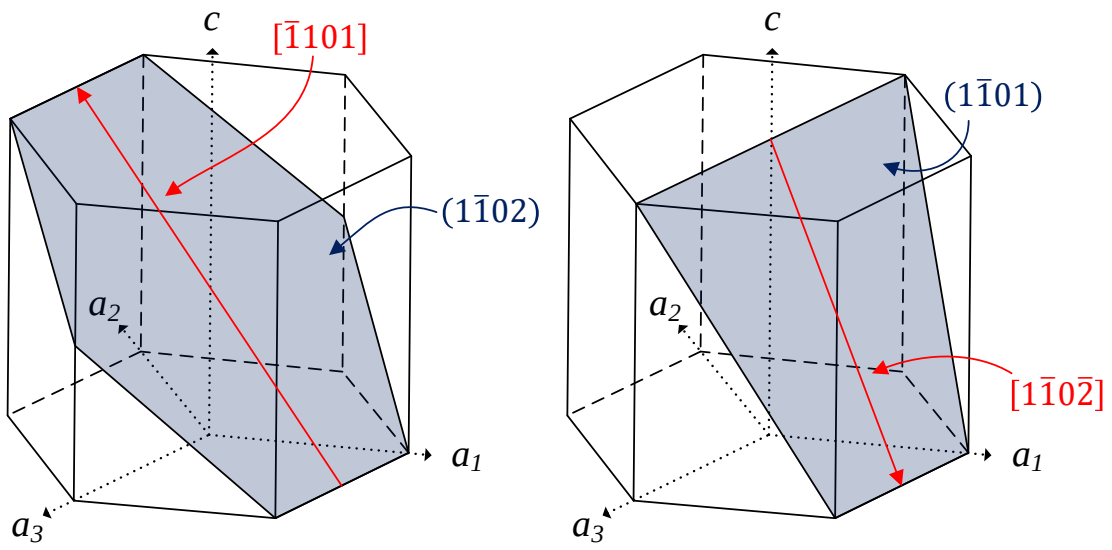

(a) Tension $\{10\bar{1}2\}$ (b) Compression $\{10\bar{1}1\}$

Figure 5: The two common twinning systems in magnesium: (a) tension (or extension) $\{10\bar{1}2\}\langle\bar{1}011\rangle$ twin and (b) compression (or contraction) $\{10\bar{1}1\}\langle10\bar{1}\bar{2}\rangle$ twin

Two less commonly observed twin systems in magnesium include the tension $\{11\bar{2}1\}\langle\bar{1}\bar{1}26\rangle$ [35–38] and compression $\{10\bar{1}3\}\langle30\bar{3}\bar{2}\rangle$ [33,39] systems. Normally, the $\{11\bar{2}1\}$ twin system is not observed in magnesium or its alloys [14,38]. However, Mokdad, Chen, and Li [35] identified embryonic $\{11\bar{2}1\}$ twins in extruded AZ31 alloy that have reoriented by greater than 70° from the matrix. These twins aid in the development of $\{10\bar{1}2\}$ twins which, with local basal slip dislocation nucleation, will eventually consume the embryonic $\{11\bar{2}1\}$ twins [40]. This explains the general absence of this twin type in the commonly studied magnesium materials. However, residual $\{11\bar{2}1\}$ twin bands have been reported in single phase binary alloys containing yttrium [36,37]. Misorientation

analysis of the twin bands revealed a 35° misorientation about the $\langle 10\bar{1}0 \rangle$ axis, matching the $\{11\bar{2}1\}$ system in titanium and zirconium [41]. It is suggested that, as the $\{11\bar{2}1\}$ twins compete with basal slip and $\{10\bar{1}2\}$ twinning, solute hardening from the yttrium is required for easier activation of the $\{11\bar{2}1\}$ system. The $\{10\bar{1}3\}$ system is the K_2 compression system listed in Table 2, which is an uncommon twin type that can change its habit plane from $\{10\bar{1}3\}$ to $\{30\bar{3}4\}$. This shifting habit plane led to early studies reporting that both $\{10\bar{1}3\}$ and $\{30\bar{3}4\}$ were possible twin systems [31], but was later clarified that both were the $\{10\bar{1}3\}$ system [39]. Misorientation analysis has this system misoriented 64° about the $\langle 1\bar{2}10 \rangle$ zone axis.

The process of twinning involves three steps: nucleation, propagation, and thickening. Twinning begins when a twin nucleus is formed with sufficient stress. Experimental studies revealed that twins form at grain boundaries, or other areas of high local stresses such as slip bands or twin boundaries [42–47]. Atomistic simulations suggest that nucleation is by pure-shuffle due to the previously noted high-stress concentrations and pre-existing dislocations at the grain boundary [48]. Thus, it is generally understood that twins are unlikely to nucleate inside a grain [46]. Grain size also affects twin nucleation, where increasing grain size usually results in more twin nucleation [49,50]. Alternatively, decreasing grain size causes the stress required to activate twinning to increase [43], more so than the stress for slip [51]. However, grain size has no effect on twin thickness or twin volume fraction, only on the nucleation [46]. Twin propagation occurs by twin boundary migration though the glide of twinning dislocations [14,52]. This process drives the twin front through the bulk of the grain until reaching an obstacle, such as a grain boundary

[53]. As the twin boundaries are already formed, propagation requires less stress than nucleation [28,54]. After reaching an obstacle, any further expansion of the twin is a result of thickening in the transverse direction and possible coalescence of parallel twins of the same variant. This occurs by similar mechanisms as propagation, as twinning dislocations migrate along the twin boundary [42]. It is noted that the twin boundary can deviate from its coherent plane. Morrow et al. [55,56] revealed that twin boundaries are a combination of the perfect, coherent plane and basal-prismatic facets. This can lead to both the commonly observed lenticular twin shape as well as highly irregular twin shapes.

2.3 Tension Twin Activation and Asymmetric Stress-Strain Response

It is important to note that the deformation of the hcp structure is highly dependent on the loading direction relative to the crystal orientation. Twin favorability is often described using Schmid factor (Schmid's law is elaborated in Appendix A), or the factor of applied stress that is resolved on a particular plane along a particular direction [57]. The activation of a deformation system is assumed when the resolved shear stress reaches a variant's CRSS. However, when discussing favorability of variants within the same system, direct Schmid factor comparisons are often made, where a maximum uniaxial Schmid factor of 0.5 can be achieved. For tension twinning, activation is by tension nearly parallel to or compression nearly perpendicular to the crystal's *c*-axis. Twin activation under torsion will be discussed in Chapter 5.

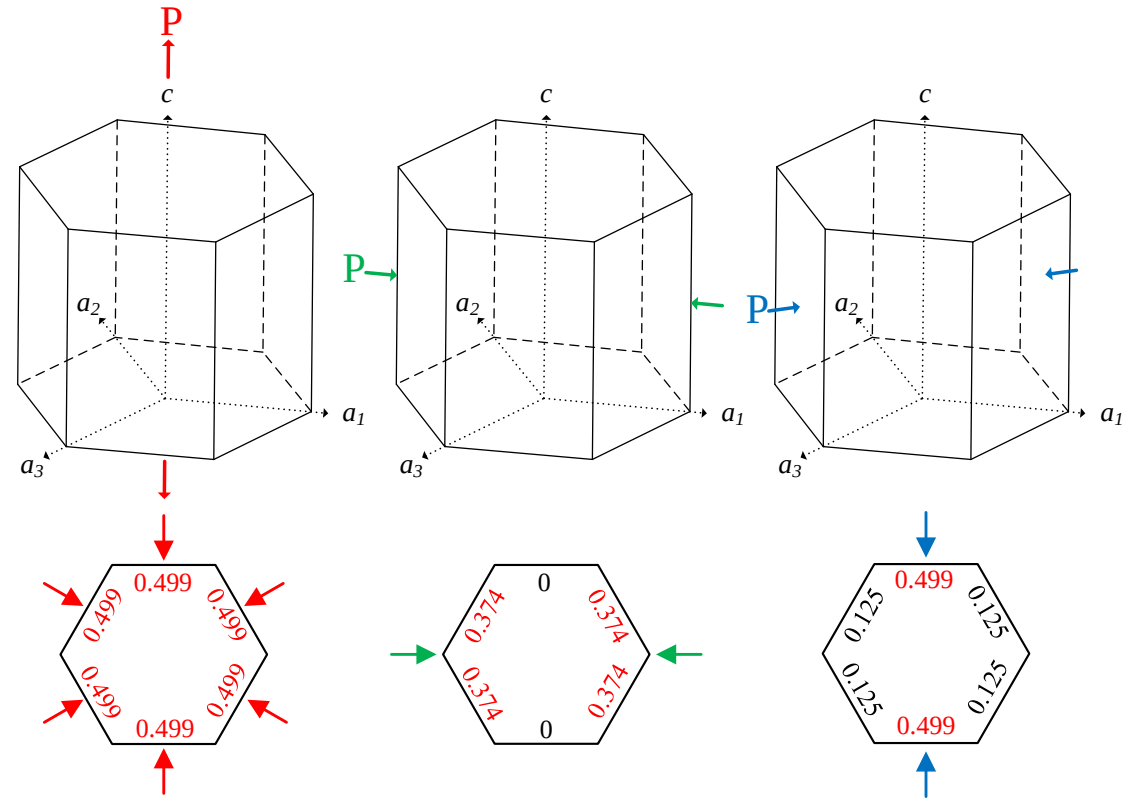

(a) Six variants favorable (b) Four variants favorable (c) Two variants favorable

Figure 6: Tension twin favorable loading relative to the crystal orientation for (a) tension parallel to the $\langle 0001 \rangle$, (b) compression parallel to $\langle \bar{2}110 \rangle$, and (c) compression parallel to $\langle 10\bar{1}0 \rangle$. Values in the second row of hexagonal cells represent Schmid factor values based on the loading.

Figure 6 visualizes the favorable loading orientation for tension twinning relative to the crystal orientation. Theoretically, twin variant selection will vary depending on the loading direction with respect to the *c*-axis [35,58,59]. For example, tension parallel to the *c*-axis is not affected by *c*-axis rotations (Figure 6a) and favors all six variants, as observed in single-crystal magnesium [60]. Alternatively, *c*-axis rotation has a significant effect on compression perpendicular to the *c*-axis. Compression parallel to *a*-axis (Figure 6b) results

in four equally favorable variants and two unfavorable variants. Compression parallel to the *b*-axis (Figure 6c) results in two highly favorable variants and four less favorable variants. In the intermediate orientations for compression ($0°<\theta<30°$), twin favorability will be paired with one favorable, one less favorable, and one unfavorable pair. Actual twin variant selection in nucleation is further complicated by localized fluctuating stress effects related to grain boundaries. Twin propagation, however, is dictated by local stresses across the grain [61]. Thus, unfavorable twin variants may still be nucleated, but the favorable variants will grow more. With these relationships, wrought magnesium and its alloys are often used to study twinning as their bulk texture are highly favorable for the activation and development of tension twinning.

The process of working by either extrusion or rolling produces strong basal textures where the *c*-axes of most grains are aligned in a specific way relative to the working process. Extrusion produces a strong basal texture where the *c*-axes of the grains are mostly perpendicular to the extrusion direction [12,62–67]. Thus, compression parallel to the extrusion direction results in tension twinning. Alternatively, rolling produces a strong texture in which the *c*-axes of most grains are roughly aligned with the material's normal direction [68–72]. For these materials, tension parallel to the rolled plate's normal direction or compression parallel to the rolled or transverse directions are favorable for tension twinning [73]. In these highly textured materials, the activation of twinning, or the lack thereof, greatly affects the mechanical behavior, which can be observed clearly by an asymmetric stress-strain curve. Figure 7 shows an example of the asymmetric monotonic

tension-compression stress-strain response in extruded pure polycrystalline magnesium with loading parallel to the extrusion direction of the bar.

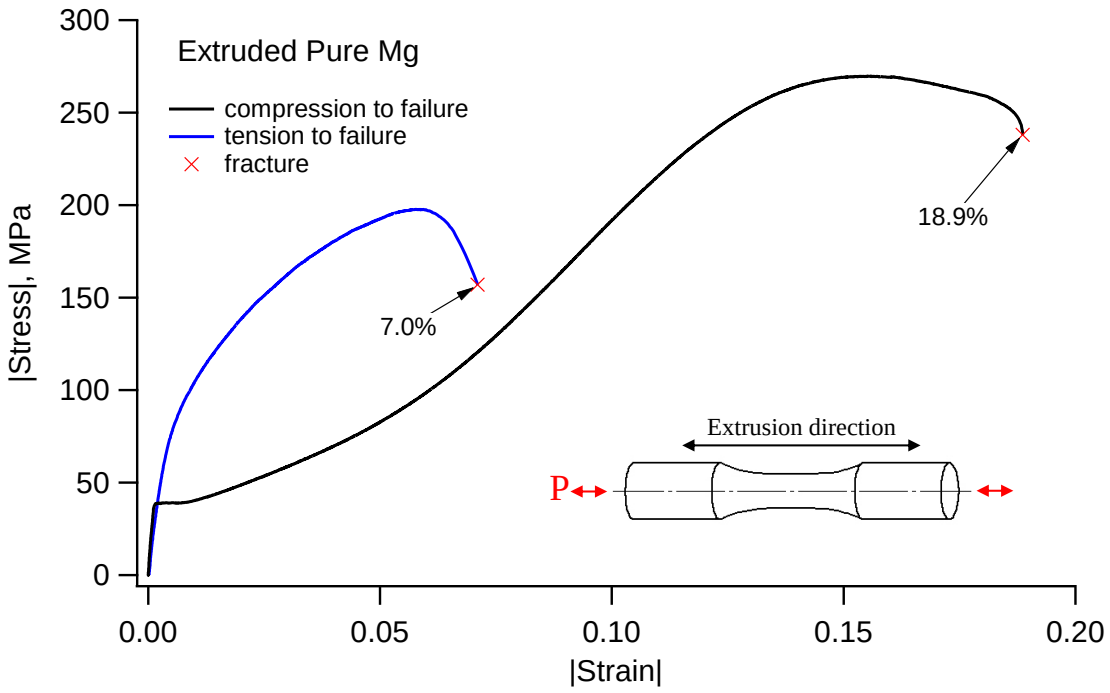

Figure 7: Asymmetrical tension-compression stress-strain response in extruded pure magnesium (adapted from [12])

Three immediately noticeable differences between the two loading conditions relate to the yield stress, stress-strain curvature, and elongation at failure of the material. All three features are directly related to the activation of tension twinning under one load condition and the lack of activation under the other. The stress-strain response under tension parallel to the extrusion direction, which is unfavorable for tension twinning, follows a typical slip dominated plastic deformation response where strain hardening is immediately observed following yielding. The strain at failure is also lower than the twin-favorable loading condition. Alternatively, yielding under compression begins with basal slip [74] followed

by tension twin nucleation, resulting in a lower yield stress than what is observed under tension [58]. The first hardening stage, one of low strain hardening, follows yielding as twinning dominates plastic deformation [58,75,76]. A second stage of increased hardening begins as twins continue to grow, thicken, and interact with other twins and slip systems, [12,50,77]. Twinning does not significantly contribute to strain hardening [76], but it has recently been reported that the significant hardening in this stage is attributed to the elastic deformation of the twinned grains [78]. As twinning nears exhaustion, a third stage of decreased hardening is observed, reflecting the typical late-stage, dislocation dominated stress-strain response leading to failure [75,77,79]. With these three stages, the stress-strain response under tension twin-favorable loading is the commonly observed S-shaped, sigmoidal curve [58,59,69,80,81]. The prevalence of twinning results in increased ductility, failing at a larger strain than the other loading condition [16].

When the loading condition changes, like during cyclic loading, detwinning is often observed [27,54,82–86]. As its name suggests, detwinning is the counter process to twinning that rotates the twinned crystal back to the original orientation. With the reversal of loading direction, a secondary tension twin of the same variant as the primary twin is activated, thus reversing the crystal rotation. Observation of detwinning in single crystal revealed that detwinning causes a gradual closing or narrowing of twin boundaries rather than the abrupt nucleation and growth of additional twinning [27]. It was previously suggested that detwinning is easier to activate when there are existing twin boundaries [87], although it may require more stress than twin growth [54]. Thus, detwinning is more energetically favorable when there are pre-existing twin boundaries from the initial loading

as opposed to nucleating new secondary twins. Additionally, back stresses developed during twinning may contribute to detwinning behavior when loading is reversed [88]. Detwinning can also occur during unloading, resulting in a Bauschinger-like effect [83,86].

For the remainder of this dissertation, discussions surrounding twin variants and twin-twin interactions will follow Sarker's method [89]. For tension twins, a label of "T_i" will be used to indicate a tension ("T") twin of "i" variant. Each primary twin type has six crystallographic equivalent variants due to crystal symmetry of the HCP crystal. T_1 corresponds to the $(10\bar{1}2)$ $[\bar{1}011]$ system as portrayed in with increasing subscripts corresponding to the other variants by a counter-clockwise rotation about the *c*-axis. Variants that share the same zone axis, such as T_1 and T_4, are called co-zone variant pairs. The same method of identification for compression twins can be used, using "C" to identify the twin as a $\{10\bar{1}1\}\langle 10\bar{1}\bar{2}\rangle$ compression twin.

2.4 Secondary and Tertiary Twinning in Magnesium

Secondary twinning, or double twinning, occurs when a second twin is formed within a primary twin. Reported secondary tension twinning involve a secondary $\{10\bar{1}2\}$ tension forming within a primary $\{10\bar{1}2\}$ tension twin [90–99], $\{10\bar{1}1\}$ compression twin [80,91,94,96,98,100–107], and $\{10\bar{1}3\}$ compression twin [39,108,109]. Under uniaxial monotonic loading favorable for tension twinning, tension-tension double twinning is unfavorable based on Schmid's law [98]. The activation of the unfavorable secondary twin is rationalized as a local stress effect, such as from a local stress concentration from a grain or twin boundary, that deviates from the macroscopically applied loading. Koike [110] reported anomalous, unfavored primary tension twins that formed to accommodate local

strain incompatibilities. The activation of secondary tension twins likely occurs for similar reasons. For example, Yu [60] observed secondary tension twins that were nucleated from a twin-twin interaction in single-crystal magnesium. However, this secondary twin type is much more favorable if the loading stress state changes, although it will be competing with detwinning.

The $\{10\bar{1}1\}$-$\{10\bar{1}2\}$ and $\{10\bar{1}3\}$-$\{10\bar{1}2\}$ compression-tension double twinning types are more commonly observed. In the cases where the compression twins are activated, the reorientation of either 56.2° or 64° is favorable for immediate secondary tension twinning, which is then ideally oriented for slip. These secondary twin systems are often diagnosed as a source of failure [100]. The $\{10\bar{1}1\}$-$\{10\bar{1}2\}$ system can result in micro-cracking or void formation parallel to the $\{10\bar{1}1\}$ twin boundary [80,103,111]. Reed-Hill [109] observed a crack and void following a supposed $\{30\bar{3}4\}$-$\{10\bar{1}2\}$ double twin, which is more likely $\{10\bar{1}3\}$-$\{10\bar{1}2\}$ as previously discussed. Yu [112] explained the local shear as a result of a $\{10\bar{1}1\}$-$\{10\bar{1}2\}$ double twin. The resulting strain of 0.044 is nearly perpendicular to the double twin boundary, thus causing a cleavage within the boundary that leads to rapid failure. These secondary twins may also form within a primary tension twin, forming a tension-compression-tension tertiary twin [94,96,113]. Observed examples of these secondary and tertiary twin structures are presented in Figure 8. Figure 8a highlights a beige-colored secondary tension twin, labeled as “ST,” within a green primary tension twin “PT.” A set of $\{10\bar{1}1\}$-$\{10\bar{1}2\}$ secondary twins are highlighted in Figure 8b where parallel tension twins can be identified in a compression twin band. Figure 8c shows a bright tension twins found within a $\{10\bar{1}3\}$ compression twin. Figure 8d highlights a

$\{10\bar{1}1\}$-$\{10\bar{1}2\}$ double twin within a heavily tension twinned grain, thus forming a $\{10\bar{1}2\}$-$\{10\bar{1}1\}$-$\{10\bar{1}2\}$ tertiary twin.

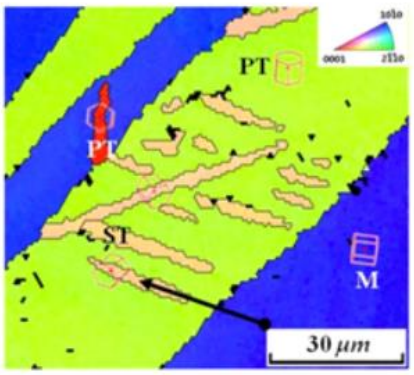

(a) $\{10\bar{1}2\} - \{10\bar{1}2\}$

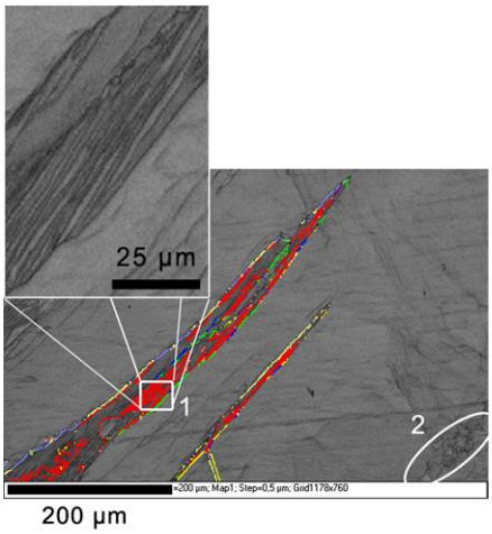

(b) $\{10\bar{1}1\} - \{10\bar{1}2\}$

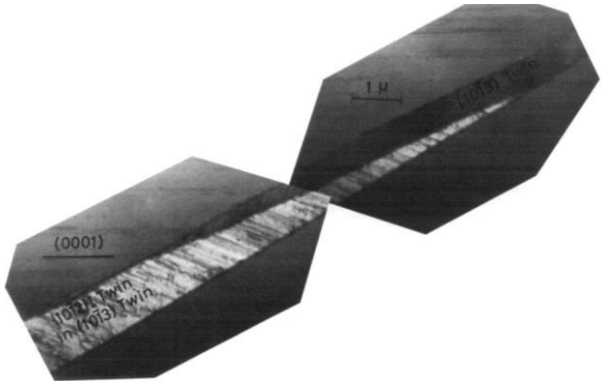

(c) $\{10\bar{1}3\} - \{10\bar{1}2\}$

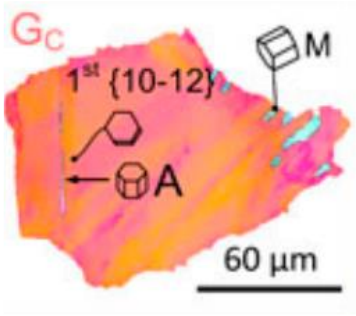

(d) $\{10\bar{1}2\} - \{10\bar{1}1\} - \{10\bar{1}2\}$

Figure 8: Observed secondary and tertiary twin types: (a) $\{10\bar{1}2\}$-$\{10\bar{1}2\}$ double twin [93]; (b) $\{10\bar{1}1\}$-$\{10\bar{1}2\}$ double twin [106]; (c) $\{10\bar{1}3\}$-$\{10\bar{1}2\}$ double twin [39]; and (d) $\{10\bar{1}2\}$-$\{10\bar{1}1\}$-$\{10\bar{1}2\}$ tertiary twin where "A" is a $\{10\bar{1}1\}$-$\{10\bar{1}2\}$ double twin formed in a primary $\{10\bar{1}2\}$ twin [113]

Expanding on the twinning nomenclature, secondary and tertiary twins will follow a similar descriptor as individual twins. For tension-tension double twins, "T_{ij}" will be used

where “i” describes the primary tension twin variant and “j” identifies the secondary tension twin variant. Compression-tension double twins, particularly the $\{10\bar{1}1\}$-$\{10\bar{1}2\}$ system, is described as “C_i-T_j,” where “C_i” is the primary compression twin variant and “T_j” is the secondary tension twin variant.

2.5 Twin-twin interactions

When two or more twin variants are activated within a grain, they eventually contact each other and form a twin-twin interaction. Requiring two of six tension twin variants, three types of tension twin-twin interactions can be defined. Type I (Figure 9b) corresponds to the interaction of co-zone pairs, or variants that share the same zone axis. The misorientation between co-zone pairs is 7.4° about $\langle 1\bar{2}10\rangle$ [60,114–116]. Type II interactions correspond to non-co-zone variant interaction and is split into two sub-types: Type II(a) and Type II(b). Type II(a) (Figure 9c) is the interaction of adjacent twin variants ($T_i \leftrightarrow T_{i\pm1}$) that has a misorientation of 60° about $\langle 10\bar{1}0\rangle$ [114]. Type II(b) (Figure 9d) is the interaction of non-co-zone, non-adjacent variants ($T_i \leftrightarrow T_{i\pm2}$), having a misorientation of 60.4° about $\langle 8\bar{1}\bar{7}0\rangle$ [114]. When discussing TTIs between tension twins, the classification proposed by Yu et al. [60] is used. $T_i \leftrightarrow T_j$ is used to describe the interaction: “T_i” identifies the encroaching twin that initiates the interaction and “T_j” denotes the barrier twin that is catching or receiving the interaction.

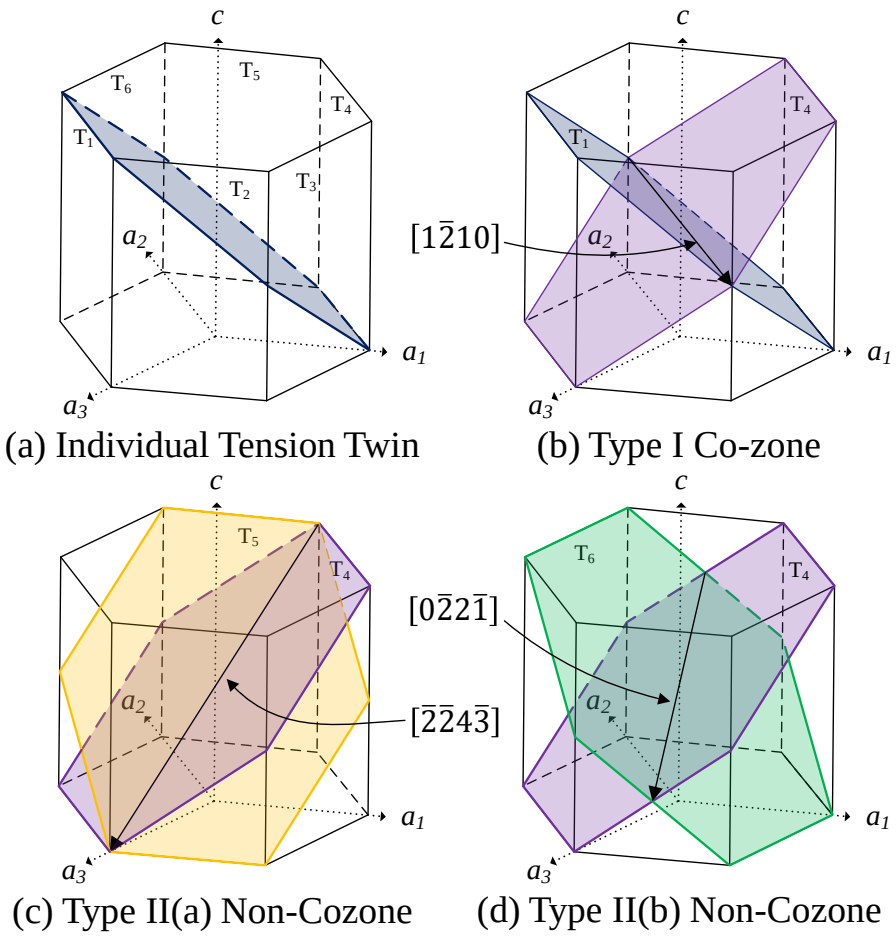

Figure 9: Twin-twin interactions in Mg [60]: (a) Tension twin variants. (b) Type I co-zone twin-twin interaction with $T_1 \leftrightarrow T_4$. (c) Type II(a) non-co-zone twin-twin interaction with $T_4 \leftrightarrow T_5$. (d) Type II(b) non-co-zone twin-twin interaction with $T_4 \leftrightarrow T_6$

Microstructurally, when two twins meet, three possible twin-twin boundaries (TTBs) can be formed [60]. The first boundary is the impinging twin-twin boundary, TTB_I, that is the result of T_i being blocked at the T_j boundary. Then there is the acute angle boundary, TTB_A, and the obtuse angle boundary, TTB_O. These two boundaries may form either by the zipping of the two twin dislocation types or by dissociation of twin dislocations from one twin into the other. The favorability for each boundary type varies in each interaction

type. Yu et al. [60,115] identified two tilt boundaries resulting from a Type I interaction – one having a habit plane of (0001), which matches TTB_O, and the other $(10\bar{1}0)$, which matches TTB_A. TTB_A was found to be energetically favorable but TTB_O was not, although it may still occur if the net elastic energy is reduced [60]. Alternatively, TTB_O is favorable in the Type II interactions while TTB_A is unfavorable [60]. Gong et al. [117] performed molecular dynamic simulations for the Type II interactions, yielding similar boundary formations for the type II(a) interaction where TTB_I and TTB_O are formed. For the type II(b) interaction, TTB_I was formed, a small TTB_A was formed, and the barrier twin was found to very slightly detwin on the obtuse side. While these structures are limited to individual interactions, larger structures containing additional twins are also observed.

At a larger scale, twin-twin interactions can result in three unique possible structures (Figure 10): a quilted-stitch pattern [27,30,60,75,85,116,118–120], apparent crossing [60,101], and double twin structure [60,93,121]. The quilted-stitch pattern was first reported by Cahn [30] in α-uranium, and later in magnesium by Roberts and Partridge [116]. The quilted-stitch pattern is defined by interlacing twins of two types, often co-zone pairs, forming multiple interactions. The apparent crossing pattern has the appearance of one twin variant crossing through a second variant, forming an X-like pattern. In this case, the larger, complete twin was formed first, and the second twin variant eventually forms an interaction on a side. As a result of the interaction, it was favorable for a second twin of the second variant to nucleate on the other side of the larger twin. The area of the larger twin that separates the two twins of the second variant undergoes a small crystal rotation. The double twin structure [60,91,93,99,121] is the development of a secondary twin at or

in the vicinity of a twin-twin interaction. Given how unfavorable the secondary twinning is during monotonic loading, the twin-twin interaction must affect the local stresses to yield the secondary twinning.

(a) Quilted-stitch (b) Apparent crossing (c) Double twin

Figure 10: Twin-twin structures: (a) quilted-stitch pattern [30]; (b) apparent crossing [101]; and (c) double twin [60]

Mechanically, twin-twin interactions affect other possible twinning phenomena at a granular level. El Kadiri et al. [119] compared the twin nucleation and growth of two grains with different number of activated twins. In a grain with only one twin, the twin propagation and thickening rate was higher. Alternatively, in a grain with interacting twins, twin thickening was lessened, but twin nucleation rate increased resulting in more twins. The overall volume of twins in both grains were found to be similar despite the difference in twin behavior. Theoretically, the grain with the twin-twin interactions should have a higher hardening rate [14]. This expands to the larger scale as well, where microstructures containing twin-twin interactions were found to undergo more hardening [75,118,122,123].

2.6 Summary

Plastic deformation in magnesium and its alloys is dominated by basal $\langle a \rangle$ slip and tension $\{10\bar{1}2\}$ twinning. Macroscopically, twinning plays a significant role in the anisotropic and asymmetric mechanical response of these materials. Microscopically, key twin developments can be reduced to three major processes: individual twin development, secondary twin formation, and twin-twin interaction. While there are many experimental works that explore these topics, there are gaps in the current understanding. Due to the difficulty of capturing a single twin, there is only limited work available focusing on the development of a single tension twin. This work can be very difficult, requiring *in situ* observation to adequately capture the twinning process. Similarly there are also limited *in situ* studies of twin-twin interactions outside of the fundamental work by Yu et al. [60]. This is especially important as there is some diversity in the twin-twin boundary formations, especially of the type I interaction type. Ideally, these studies should be performed on single-crystal magnesium, which allow for larger and simpler interactions devoid of significant local stress effects. As for *ex situ* analyses of polycrystalline magnesium, limited studies on the effect of pre-twinning has been studied in uniaxial experiments. Additionally, the microstructural evolution during free-end torsion has been inadequately reported.

3 Cross-Grain Twin Pair Nucleation and Growth in Polycrystalline Pure Magnesium

To better capture microscopic twin development, an experimental procedure utilizing sequential *in situ* loading under optical microscopy (OM) and *ex situ* electron backscatter diffraction (EBSD) analysis was developed. *In situ* OM captures the microstructural evolution during deformation, while *ex situ* EBSD characterizes the microstructural evolution and assists in twin identification. This new experimental procedure was applied to extruded polycrystalline magnesium. Monotonic tension was applied in a direction perpendicular to the extrusion direction (ED) and parallel to the radial direction (RD) of the extruded bar. *In situ* observation captured twin nucleation and propagation within grains. In some cases, two twins appear to meet at a shared grain boundary. These cross-grain twin pairs, or adjoining twin pairs (ATPs) as called by Beyerlein et al. [61], are observed forming rapidly and span multiple grains.

ATPs are commonly observed in deformed hcp metals [12,35,43–46,58,59,62,72,79,83,124,125]. However, long chains of ATPs are rarely highlighted [126]. Only recently have studies focused on the formation process and variant selection of the associated twins [61,127–131]. There have been two ATP formation processes suggested: “sequential twinning” [42] (also called “associated nucleation” [44,132]) and “isolated nucleation” [44,132]. Sequential twinning involves a twin in one grain propagating to a grain boundary, assisting in the nucleation of a twin in the adjacent grain from the shared boundary. This process requires a small grain boundary misorientation to

occur, as it is a twin-to-twin accommodation mode. Isolated nucleation occurs when the twins in adjacent grains form independently but converge at the shared grain boundary. This process is a twin-to-slip accommodation mode and is associated to non-favorable grain misorientations.

There is a distinct lack of true *in situ* study of these twin structures. A few of the reported studies utilize *in situ* EBSD [127,128,132], allowing for the observation of the same area. However, *in situ* EBSD lacks sufficient capture rate to capture the small details associated with the formation of these twin structures. *In situ* OM offers significantly improved capture rate, while *ex situ* EBSD provides the same characterization ability as *in situ* EBSD. Utilizing a sequential *in situ* OM, *ex situ* EBSD testing procedure, a connected chain of ATPs spanning seven grains was captured and characterized. Additionally, a new ATP formation process assisted by twin thickening is also captured through *ex situ* EBSD.

3.1 Development of a Combined *In Situ* OM, *Ex Situ* EBSD Procedure

A combined method of *in situ* observation and *ex situ* analysis was developed to capture the deformation of magnesium. The procedure, as shown in Figure 11, can be separated into the *in situ* loading experiment and *ex situ* analysis. The *in situ* testing procedure can also be reduced to two elements: the mechanical testing system and the light optical microscope. An MTI Instruments/Fullam SEMTester *in situ* loading device with a load cell capacity of ±1000 lb (±4.5 kN) was used for uniaxial loading experiments. The system comes with a proprietary computer control and material testing software package. Special grips were designed and machined to fit small dog-bone shaped plate testing specimens.

The grips were designed for tensile loading, so additional modifications to the specimen design or the use of extra parts are required for compressive or cyclic loading.

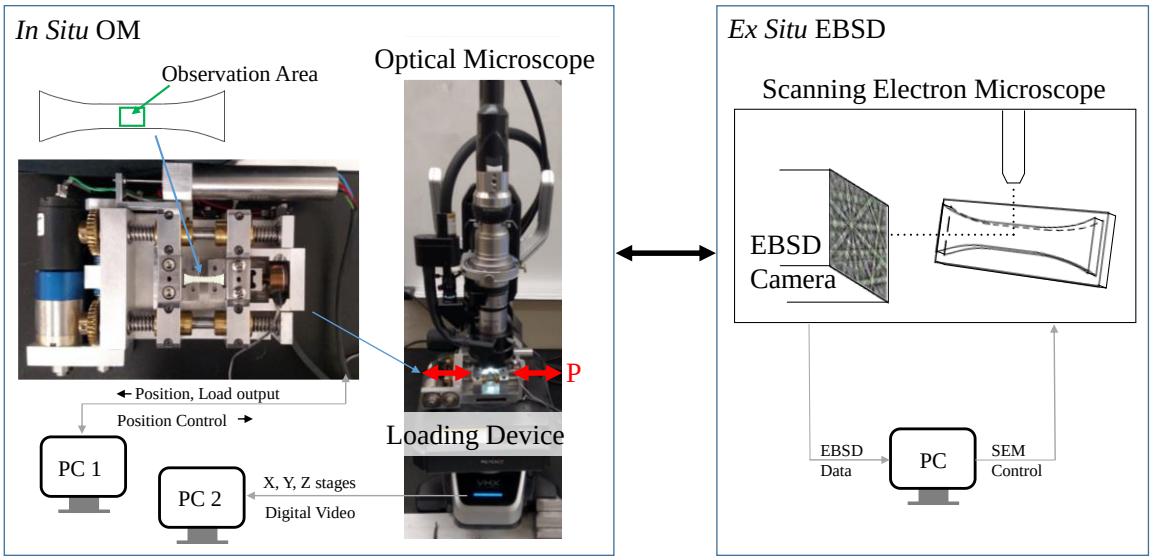

Figure 11: Schematic of the combined *in situ* optical microscopy experiment, *ex situ* electron backscatter diffraction procedure

In situ observation was conducted using a Keyence VHX-5000 model digital light optical microscope offering magnification from 100x to 1000x. The VHX system comes with its own computer system, separate from the loading device. Its proprietary system comes with the ability to record video at 15 frames per second (0.066 second/frame) and resolution that varies with magnification. Manual time syncing of the loading experiment and video recording had to be used so that real time frames could be correctly correlated to its load-displacement data. Deformation was recorded at the center of the testing specimen, which has general dimensions provided in Figure 12.

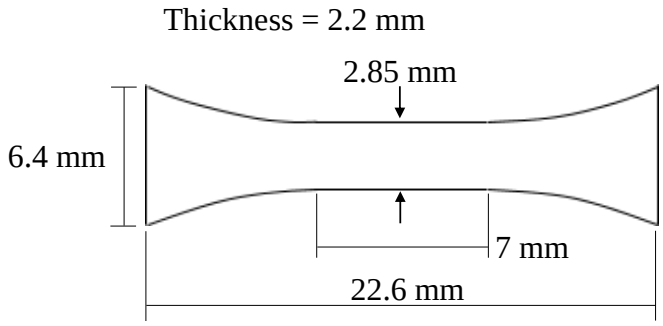

Figure 12: Specimen design for the combined *in situ* - *ex situ* testing procedure

Testing specimens were axially loaded horizontally under the microscope using displacement control to a pre-defined displacement or load to induce the desired amount of deformation and then unloaded. *Ex situ* EBSD analysis was then conducted on a JEOL 7100F field emission scanning electron microscope (SEM) with an Oxford HKL Channel 5 EBSD package. An accelerating voltage of 25 kV, probe current of 12, and working distance of about 25 mm were used. Inverse pole figure (IPF) maps were scanned to replicate the observation area recorded by *in situ* OM. Additional scans away from the observation area may also be recorded for *ex situ* analysis to maximize results. The specimen is then loaded further by *in situ* OM and the process is repeated until the specimen fails or satisfactory results are achieved. Unable to apply an extensometer to measure strain, changes in displacement measurements between clearly identifiable points in the observation area are used to measure the strain of individual frames.

With the clarity and resolution of the digital microscope, this combined method most closely replicates the capability of *in situ* EBSD without the drawbacks. As previously mentioned, *in situ* EBSD is severely limited by the data capture rate, or its framerate, and loading procedure. High resolution (large area, small step size) EBSD maps can take hours

to scan, so the testing procedure is also affected. To take a scan at any strain, either the load must be held for an extended time allowing creep to occur, or the specimen must be unloaded prior to scanning. Both options lose data. Other *in situ* and *ex situ* procedures also have their own limitations. Alone, i*n situ* OM has the benefit of good frame rate and resolution but cannot characterize twins or crystallography of polycrystalline materials. *In situ* neutron diffraction allows for bulk material twin study but cannot capture individual details. Alone, *ex situ* EBSD can only partially replicate *in situ* results. Thus, the combined method provided here allow for the best compromise of resolution, frame rate, and characterization. *In situ* OM captures the deformation behavior in real time, allowing the full development of twinning to be seen under loading and unloading. *Ex situ* EBSD then characterizes the twinning observed by *in situ* OM. Additional *ex-situ* OM and *ex situ* EBSD maps outside of the observation area can also allow for traditional *ex situ* analyses to be performed.

3.2 Material and Specimen Preparation

To apply the *in situ* OM, *ex situ* EBSD procedure to extruded pure polycrystalline magnesium, small dog-bone shaped plate specimens were fabricated to the dimensions shown in Figure 12 by electrical discharge machining (EDM). Next to single-crystal magnesium, polycrystalline pure magnesium is ideal for study due to having a larger grain size than wrought alloys. As shown in Figure 13, the specimens were fabricated with an observation area perpendicular to the extrusion direction and loading direction parallel to the radial direction of the extruded bar. Thus, the c-axes of some grains will align with the loading axis allowing for tension twinning under tension. Prior to experimental testing, one

side of the plate specimens was prepared to EBSD quality using traditional metallographic procedures. Grinding was done sequentially using silicon carbide grit paper from 320/P400 grit to 1200/P4000 grit, followed 6 μm and 1 μm polishing using oil-based diamond suspensions. Final polish was achieved using 50 nm alumina-based suspension. Specimens were then etched for EBSD characterization with 3% nital (30 mL ethanol, 1 mL nitric acid). EBSD was then performed using a JEOL 7100F field emission scanning electron microscope (SEM) with an Oxford HKL Channel 5 EBSD package.

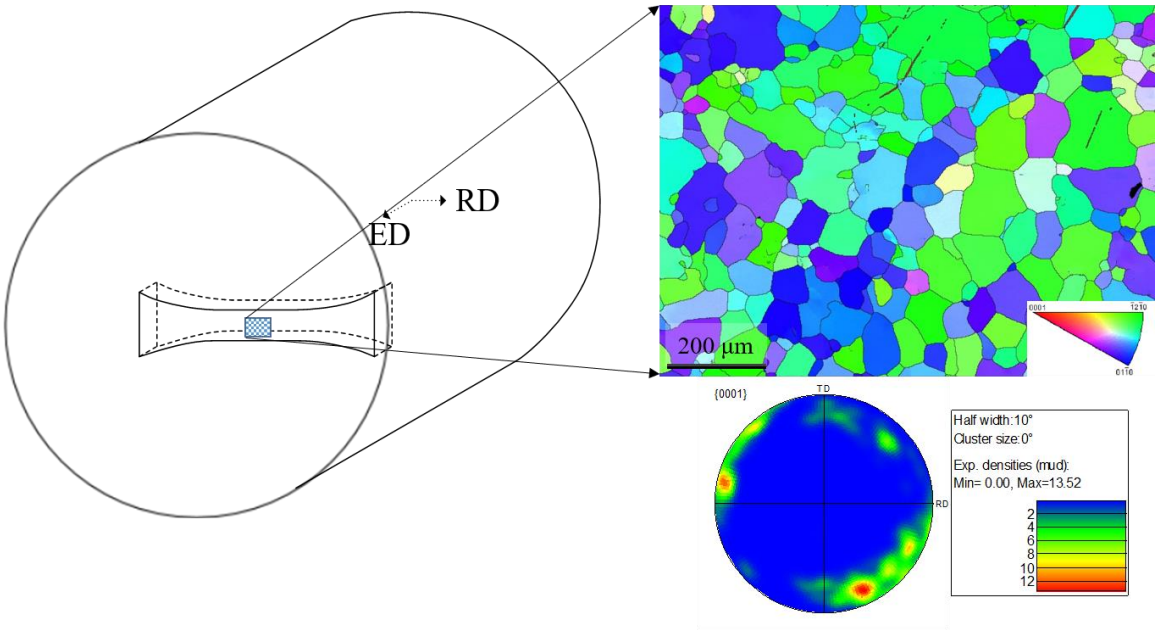

Figure 13: Polycrystalline magnesium dog-bone shaped specimen as machined from an extruded bar and the inverse pole figure EBSD map of the observation area with its corresponding basal texture pole figure

3.3 *In situ* Tension and Tension Twin Observation

In situ tensile loading was applied to the polycrystalline magnesium specimen at a displacement rate of 1 mm/min to an arbitrary displacement and then unloaded 0.5 mm/min. The observation area of 1026 x 770 μm^2 containing 240 grains was selected in the middle of the specimen. *Ex situ* EBSD inverse pole figure maps covering an area of 1000 x 750 μm^2 best replicating the OM observation area were captured. This process was repeated several times, with the sample being removed for EBSD characterization at certain deformation steps. The process and results are summarized in Figure 14, where each row corresponds to major segments of twinning development. Note that the stress is proportional to the values used here.

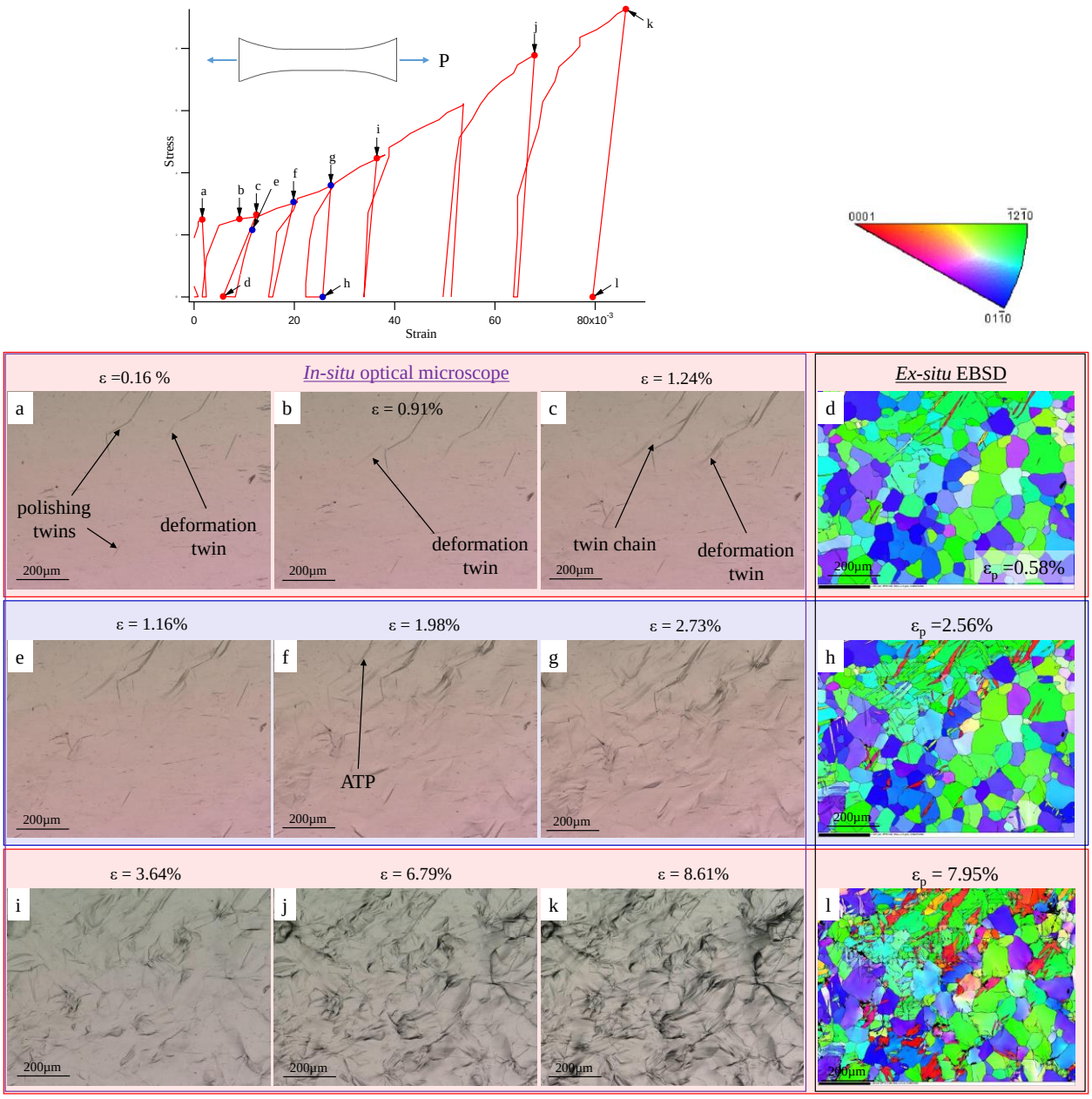

Figure 14: Summary of results from applying the combined *in situ* OM, *ex situ* EBSD method to extruded polycrystalline pure magnesium.

The first row, Figure 14a - 14d, corresponds to the first two loading sets. Pre-existing polishing twins are observed prior to loading. The first loading set (Figure 14a) did not yield significant deformation, although some very small twins can be observed. The

specimen was loaded again (Figure 14b – 14c) yielding some visual deformation. A possible singular tension twin band is optically observed and highlighted in Figure 14b. This twin is clearly thickened by Figure 14c and a second nearby twin can also be seen diagonally up and right from the first. A third twin can also be clearly seen to the right of the first two. EBSD characterization after unloading (Figure 14d) reveals that the first two "twins" are part of a twin chain spanning seven-grains and the third "twin" is an abnormal ATP. It is also clear from comparing the OM frames with the EBSD scans that some twins are not easily observed by OM, such as the middle twin forming the seven-grain twin chain. Further strain (Figure 14e – 14g) reveals more twinning and ATP formation in favorably oriented grains. Checking the grain boundary misorientations between ATPs, the findings here are consistent with statistical reports in literature [44,61,132–135]. Additionally, the surface morphology becomes rougher with increasing strain, but EBSD quality is not severely hampered, even at strains near 8% (Figure 14l). From the observations made in Figure 14, three significant ATP formations are highlighted. The first is the twin chain of ATPs that form across seven grains observed optically from Figure 14b – 14c and supported by EBSD characterized in Figure 14d. The second highlighted ATP formation is observed optically in Figure 14c, but the exact mechanism cannot be directly captured without visible grain boundaries. However, the process is deducted using a series of EBSD maps taken of the observation area. The third ATP formation occurs around Figure 14f but is not seen optically as the twin variants activated rotate in-plane. However, a similar process to the second highlighted ATP formation is deduced by EBSD analysis.

3.4 Propagation-Assisted Formation of Adjoining Twin Pairs

The first highlighted ATP formation process involves a twin chain of ATPs spanning seven grains forming over 0.87 seconds and 0.09% strain. Direct *in situ* OM observation (Figure 15b - 15f) captures the development during tension from 0.82% total strain to 0.91% total strain.

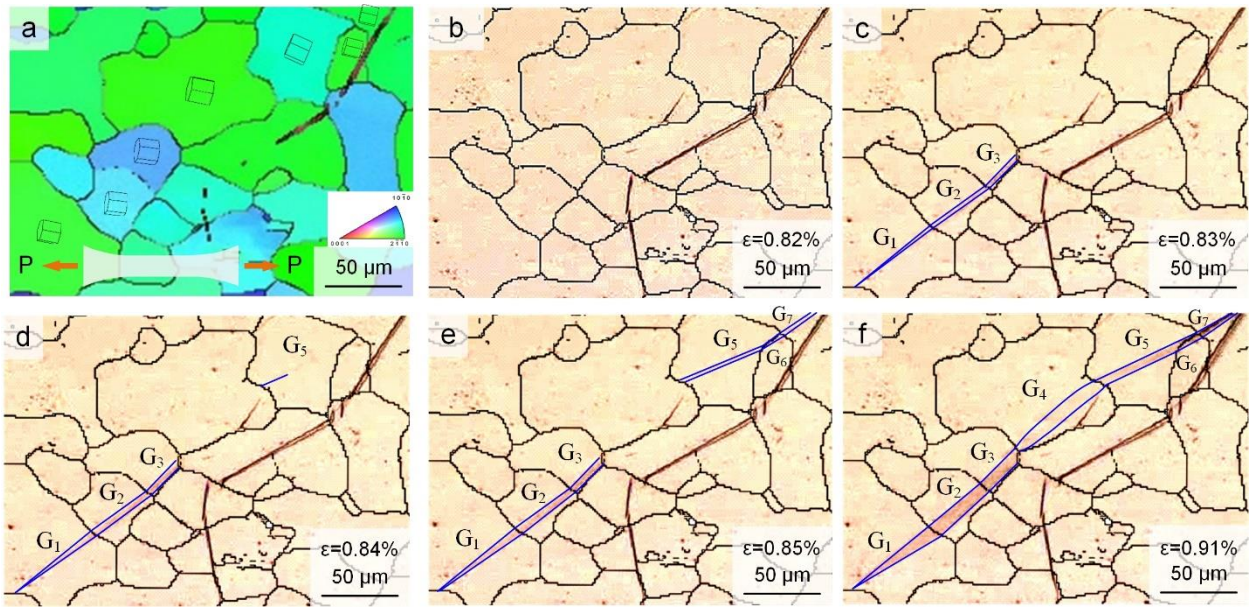

Figure 15: Development of a twin chain spanning seven grains: (a) crystal orientation map scanned from the undeformed sample; (b-f) *in situ* optical frames with imposed grain boundary maps [10]

The unstrained EBSD inverse pole map (Figure 15a) was used to overlay the grain boundaries onto the OM images using the pre-existing polishing twins as references. Optical identification of twin boundaries was made by detecting contrast differences between the matrix and twin domains in the OM images. Initial Schmid factor (*SF*), *m*, analysis of the seven grains reveal values greater than 0.45 in all but one grain, G_5. While these values are high and very favorable, the rank of the activated twin may not be the

highest, where the rank 1 variant has the largest *SF* and the rank 6 variant has the smallest *SF*. Figure 15b, at 0.82% total strain, corresponds to the frame immediately preceding twinning. One frame later at Figure 15c, an initial twin chain spanning three grains was observed. Because this chain forms after one frame, the sequence cannot be confirmed. However, the location of the chain and very small misorientation between the grains, the chain most likely formed through a twin propagation assisted mechanism. This mechanism matches the previously reported sequential twinning and associated twinning mechanisms [42,44,132]. The process follows such that a twin propagates to the grain boundary, where the paired twin nucleates in the adjacent grain. EBSD observations revealed that the formed pairs grow synergistically, where both twin's boundaries are aligned across the grain boundary. Early work studying the formation of ATPs focus on grain boundary misorientation [44,61,132–135], suggesting that grain boundary misorientations of 5° - 35° are favorable for ATP formation. More recent studies have applied a geometric compatibility factor, *m'*, which was originally used for slip transfer study in Ti-Al alloys [136], to ATP formation in titanium [125]. Instead of basing favorability on grain boundary misorientation, this factor instead checks the compatibility or the ability for the twin pair to accommodate the local stress based on the alignment of the two twins. For twinning, this geometric compatibility factor is defined as:

$$m' = \cos\Psi \cdot \cos\kappa \tag{3.1}$$

where Ψ (or κ) is the angle between the twin plane normal (or twin shear direction) of the adjoining twin systems. This value cannot be greater than one, which would equivalent to two grains of the same orientation having the same twin variant. From their study of

titanium, Wang et. al. [125] suggest that the alignment of twinning systems should satisfy *m'* greater than 0.8 and that at least one of the activated twins should have a Schmid factor greater than 0.4.

Confirming both the grain boundary misorientations and *m'* for the ATPs formed in Figure 15c revealed a highly favorable alignment. Each activated twin is independently favored to twin with *SF* values of 0.456 (rank 2), 0.475 (rank 1), and 0.470 (rank 1) for grains 1, 2, and 3, respectively. Additionally, the grain boundary misorientations were found to be less than 11° and *m'* was greater than 0.978 between each grain. This further supports the propagation-assisted mechanism, allowing the chain to rapidly form across three grains with strong favorability. However, further expansion of this chain is improbable at this point due to unfavorable grain orientations to the left of grain G_1 and right of G_3. Further strain to 0.84% (Figure 15d) reveals a new twin nucleation in G_5 from the grain boundary to G_4. This grain had the lowest of the seven *SF* values within the chain with 0.372 (rank 4) but is still considered favorable for twinning. This twin rapidly forms a chain spanning G_6 and G_7 (Figure 15e). Performing a similar analysis as the previous chain reveals grain boundary misorientations less than 14° and *m'* values greater than 0.95. Although each grain in this second chain is of lower rank than the twins activated in the first, they are still deemed favorable to form with *SF* values of 0.454 (rank 3) and 0.461, respectively. While the upper chain was forming through assisted nucleation by twin propagation, the bottom twin chain thickened closer to the grain boundary to G_4. OM twin identification in G_4 is difficult due to the crystal rotation from twinning being in plane, resulting in minimal dimensional change in the observation direction. Eventually the two

chains nucleate separate ATPs in G_4, which meet in the middle to conjoin and coalesce (Figure 15f) as observed by EBSD. While difficult to see in Figure 15f, there is a visible enough contrast between the G_4 and the twins within that the twin chain could confidently be outlined. Both nucleated ATPs in G_4 are favorable. The lower ATP formed between G_3 and G_4 has a misorientation of 21° and *m'* of 0.927 while the ATP formed between G_4 and G_5 had similar values of 23° and *m'* of 0.911, respectively. A summary of these results and the EBSD inverse pole figure map following unloading from 1.24% total strain are given in Figure 16. Although G_5 has as Schmid factor less than 0.4, the high favorability of *m'* greater than 0.9 through the entire chain yields consistent results with other reports on magnesium alloys subjected to compression [130,131].

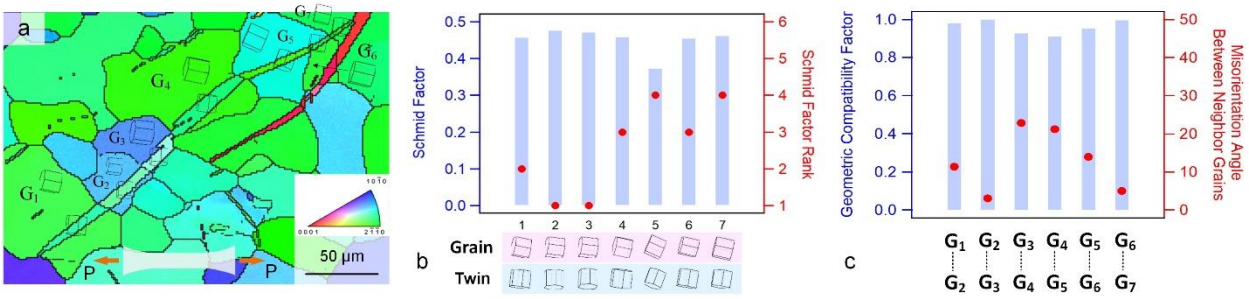

Figure 16: (a) EBSD observation of the area containing the seven-grain spanning twin chain at ε_p = 0.58%. (b) Schmid factor and its rank for the activated twins. (c) Geometric compatibility factor (*m'*) for the ATP and the misorientation angle between the neighboring grains [10]

3.5 New Thickening-Assisted Formation of Adjoining Twin Pairs

While ATP formation by twin transmission across grain boundaries is common, the second and third highlighted ATP formations at the end of Chapter 3.3 reveal a new ATP formation assisted by twin thickening. The process involves a twin thickening within one

grain until reaching the boundary to an adjacent grain and, as with the propagation-assisted mechanism, “transmits” into the adjacent grain. Figure 17 highlights the two cases identified by *ex situ* EBSD.

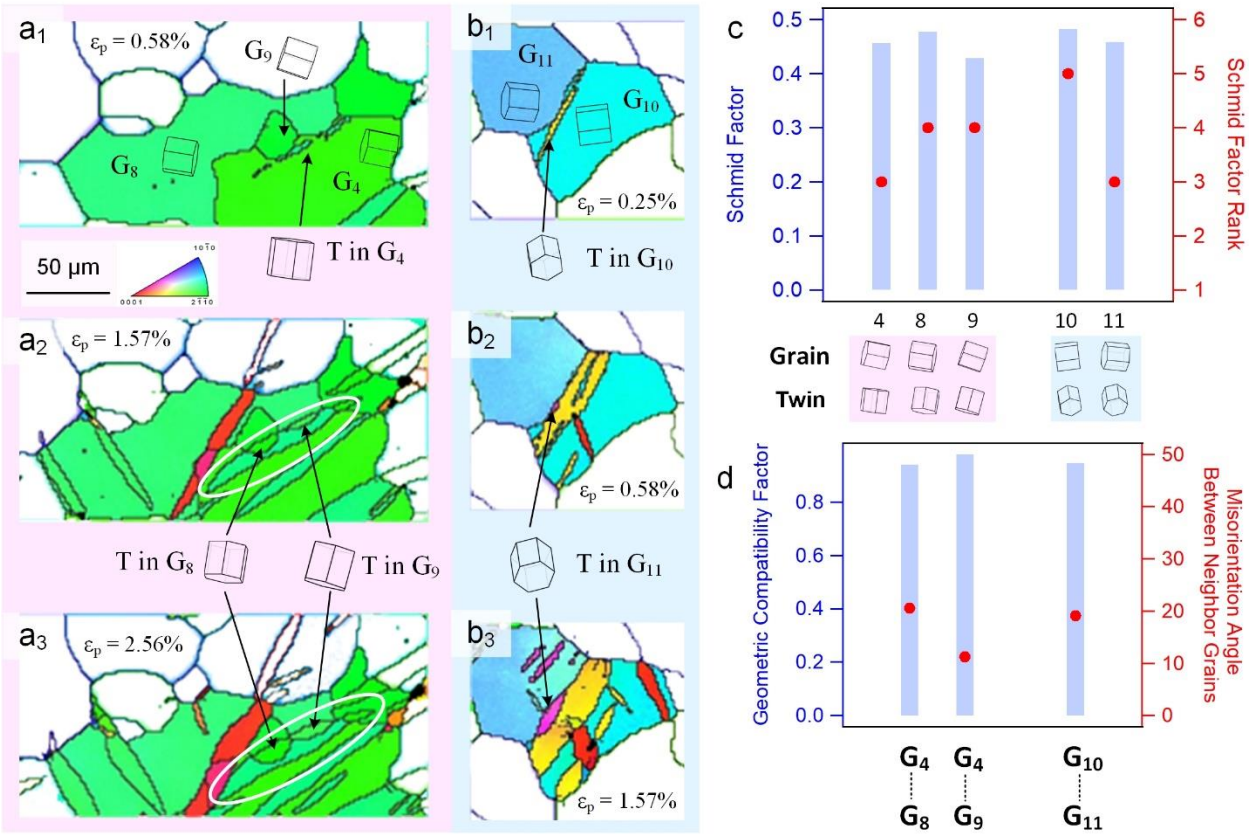

Figure 17: (a_1-a_3) and (b_1-b_3) *Ex situ* EBSD observations of cross-grain twin pair formation across grain boundaries by twin thickening. (c) Schmid factor and its rank for the activated twins. (d) Geometric compatibility factor (*m'*) for the ATP and the misorientation angle between the neighboring grains [10]

In the first case (Figure 17a), an initial twin, as highlighted by an arrow in Figure 17a_1, with a *SF* of 0.457 (rank 3) can be found by EBSD at 0.58% plastic strain within G_4. For the second case (Figure 17b), an initial twin with a *SF* of 0.483 (rank 5) is observed within G_{10} at 0.25% plastic strain. Some geometric similarities between the two cases are

immediately evident. In both cases, the initial twin is roughly parallel to an adjacent grain boundary. Additionally, the grain boundaries are slightly embedded within the initial grains, which will allow the twin to thicken slightly past the tip of the grain boundary. At 1.57% plastic strain (Figure 17a_2), the twin in G_4 has already thickened to the G_8 and G_9 grain boundaries, forming ATPs across both boundaries. The *SF* values for these paired twins are large but with lower ranks, having values of 0.478 (rank 4) and 0.428 (rank 4), respectively. Their *m'* values from G_4 are also very favorable, having values of 0.941 and 0.978, respectively. Further straining to 2.56% plastic strain (Figure 17a_3) shows further thickening of the ATPs into G_8 and G_9, maintaining their connected twin boundaries at the shared grain boundaries. Increasing the plastic strain in the second case to 0.58% (Figure 17b_2), a small twin having a *SF* of 0.458 (rank 3) can be observed in G_{11} at the shared grain boundary. This induced twin also has a large *m'* value of 0.946, suggesting favorability for ATP formation.

In the three ATP cases presented, initial twinning is dominated by large *SF* values greater than 0.38, a value slightly lower than the 0.4 value reported in [125], although the activated twins do not always have a high rank. As described in Chapter 2.3, tension loading favorable for twinning will often have large Schmid factor for all six variants, and thus rank is less significant in variant selection. In polycrystalline magnesium, additional effects of grain size and varying levels of *c*-axis misalignment with respect to the loading direction further complicate variant selection of the initial twin. For the paired variant, selection is dominated by grain misorientation accounting for both *c*-axis and *a*-axis misorientation. The geometric compatibility factor, *m',* accounts for both of these

alignments such that large *m'* values correspond to better alignment of the paired twins. Additionally, it is observed that the twin boundaries of both twins forming an ATP meet at the shared grain boundary giving the appearance of one singular twin entity. With further strain, the twins in each ATP continue thickening while maintaining the twin boundary alignment at the grain boundary.

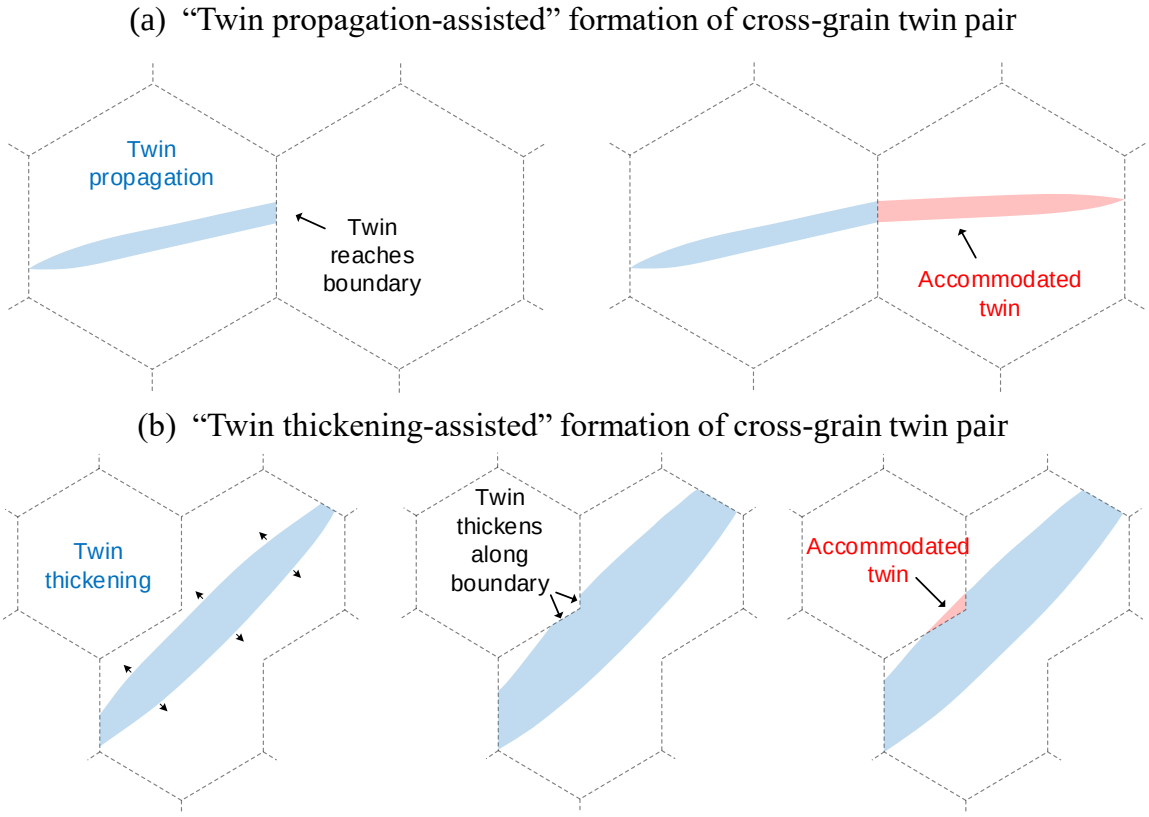

Figure 18: Schematic illustration of proposed formation of cross-grain twin pair: (a) "twin propagation-assisted" formation, and (b) "twin thickening-assisted" formation. [10]

Through *in situ* observation and *ex situ* analysis, two cross-grain twin pair formation processes were identified for magnesium subjected to twin favorable tensile loading. A schematic showing the two formation processes are presented in Figure 18. The "twin

propagation-assisted" formation (Figure 18a) is synonymous with the previously reported "sequential twinning" [42] and "associated nucleation" [44,132] mechanisms. In this process, a twin propagates until it is impinged at a grain boundary, forming a large inclination angle between the twin plane and the grain boundary. Mobile twinning dislocations at the twin front become pinned, causing a local back stress. The paired twin is nucleated near the pinned twinning dislocations, relaxing the local stress concentration at the grain boundary. The ease of the paired twin formation increases with a smaller misorientation between the neighboring the grains, as it is more favorably aligned for the shear to transmit across the grain boundary. With increasing strain, the paired twin will continue to propagate toward a distant grain boundary. If the same conditions are met at that boundary, another ATP may form.

In the newly identified "twin thickening-assisted" process (Figure 18b), the initial twin is already shown impinged at a grain boundary. In the simplest case, ATP formation by twin propagation-assistance is ignored despite the possibility. Careful examination of the ATPs generated in Figure 17a, the twin from G_4 can be seen with a twin propagation-assisted ATP in a neighboring grain. Being impinged along the twin shear direction, twin growth will be sustained through twin thickening by twin boundary migration. Eventually, the continuity of the twin boundary will be interrupted when part of the twin boundary reaches the grain boundary along the thickness, splitting the twin boundary into segments. These segments will continue to thicken "around" the grain boundary, increasing the amount of contact between the now partially impinged twin boundary and the grain boundary. While the mobile segments away from the contact area continue to thicken,

twinning dislocations become impinged at the grain boundary. Then, as with the propagation-assisted formation, the local stress concentration due to the buildup of twinning dislocations can be accommodated by the formation of an ATP assuming it is energetically favorable to do so.

3.6 Summary

A robust, combined *in situ* OM, *ex situ* EBSD experimental procedure was developed for the study of twinning in magnesium. This specialized procedure provides the benefits of both *in situ* observation, allowing for real time imaging of deformation with higher resolution and framerate compared to *in situ* EBSD, and the characterization of EBSD. This procedure was used on extruded polycrystalline magnesium subjected to tension loading favorable for tension twinning. The following conclusions have been drawn from this work:

1) Twin propagation-assisted, otherwise known as “sequential twinning” or “associated nucleation,” formation of cross-grain twin pairs, or ATPs, was captured by *in situ* observation. From *ex situ* EBSD analysis, a new “twin thickening-assisted” formation was identified by which a paired twin is nucleated in a neighboring grain through the thickening of the initial twin. Mechanically, both formation methods are similar where the energetically favorable paired twin relaxes the local stress concentrations at the shared grain boundary.
2) A twin chain comprised of multiple ATPs spanning seven grains of similar orientations was formed rapidly by twin propagation-assisted formation. *In situ* OM revealed that the chain was formed from two smaller chains coalescing in a middle grain. Variant

selection of the cross-grain twin pair is strongly affected by the geometric compatibility between the paired twins, more so than by Schmid factor or Schmid factor rank. All twins activated had a Schmid factor greater than 0.37 and geometric compatibility across each grain was highly favorable with *m'* values greater than 0.9.

3) Two cases of adjoining twin pair formation was captured from the twin thickening-assisted formation process by *ex situ* EBSD. Favorability was similar as the twin propagation-assisted process where individual twins were individually favorable and favorable for ATP formation. Schmid factor values for each twin were greater than 0.4 and the geometric compatibility between the formed pairs were greater than 0.9.

4 [0 0 0 1] Tension of Single-Crystal Magnesium

Single-crystal material is ideal for the study of fundamental deformation mechanisms due to the lack of grain boundaries and its singular orientation. With these features, specimens can be manipulated to favor specific deformation systems while suppressing others. Thus, many early studies utilized single-crystalline magnesium to isolate fundamental deformation systems [18–20,31,33,109,116,137–140]. The majority of these early studies were primarily focused on non-basal slip and non-tension twinning modes - a topic much less researched now [22,141–146]. More recent studies have focused on tension twinning in monotonic loading [23,93,147–150] and twinning-detwinning in cyclic loading [27,60,85,90,151,152]. However, only few studies have utilized *in situ* methods to capture physical process of twinning [27,60,150,153].

4.1 Materials and Specimen Design, Manufacturing, and Preparation

Single-crystal magnesium was acquired in the form of a cylindrical rod with the *c*-axis of the crystal aligned along the length of the rod. The other two key axes with respect to the rod were identified by cutting a small piece and characterizing it by EBSD. Knowing the specific orientation of the bulk material, specimens of desired orientation can be manufactured.

4.1.1 Specimen Design

To utilize the testing procedure described in Chapter 3.1, small dog-bone shaped plate specimens that fit in the custom grips must be manufactured from the single-crystal rod. To activate twinning, specimens were designed such that the *c*-axis of the specimen is

nearly aligned with the loading direction. The $(\bar{1}2\bar{1}0)$ observation plane was used for the tension specimens. Similar specimen dimensions to what was used in the study of ATP formation in polycrystalline pure magnesium is used here. Figure 19 clarifies the relationship between the tensile testing specimen geometry and the hcp crystal.

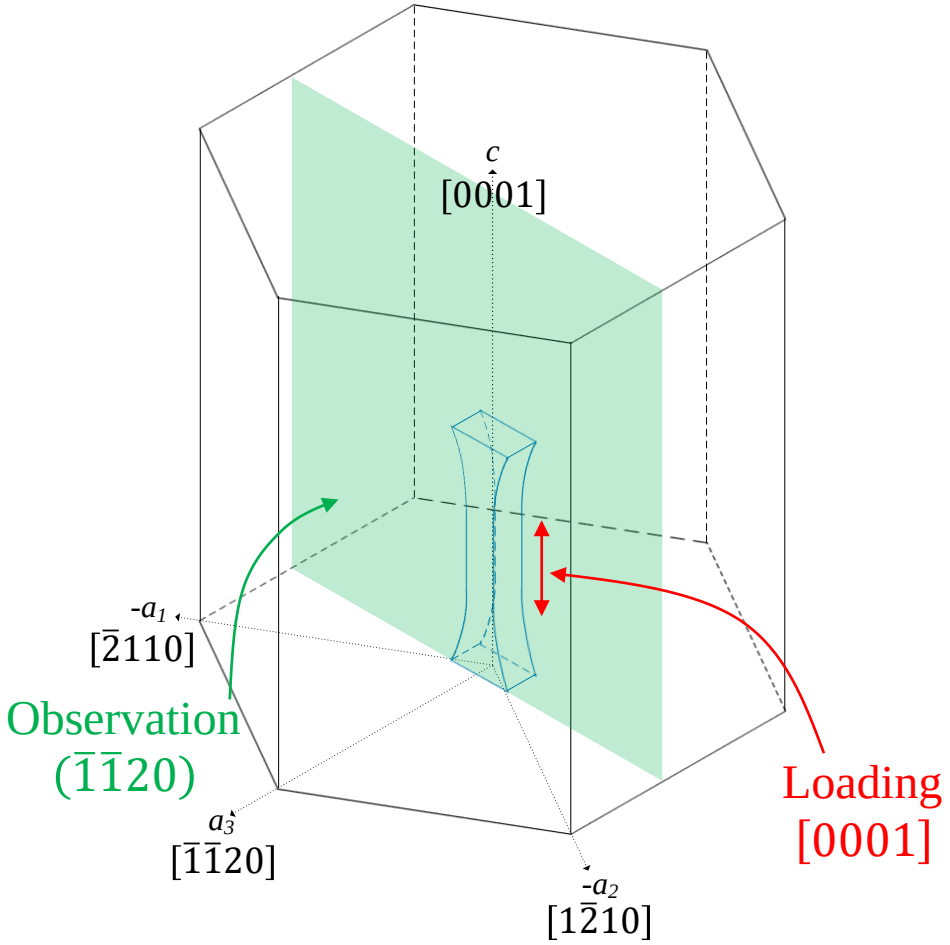

Figure 19: Single-crystal magnesium specimen design for *in situ* study

4.1.2 Material Cutting by Acid Saw

With the CRSS for twinning, especially in single-crystal magnesium, traditional manufacturing methods by material removal can induce twinning. At the scale of this specimen size, electromagnetic discharge machining, also called EDM, is a commonly

used technique to cut single crystal [60,150,154]. However, even with careful application, special heat treatments may still be required to anneal any deformation twins in the manufacturing procedure. To avoid any deformation in the material removal process, an acid saw utilizing a corrosive material removal process may be used. Acid saw machines "cut" material by reciprocating a very thin stainless-steel wire between two pairs of capillary plates containing acid, or in this case 35% nitric acid in water. The wire transfers droplets of acid from the plates to the material being cut, where material is removed by corrosion as opposed to mechanical action. This is done by fixing the wire on one end, passing it through a pulley system, and hanging a 22.3 g weight on the other end to maintain tension in the wire. The capillary plates and material are located in the center of the system while a motorized arm near the fixed end produces the reciprocating motion for the wire. Figure 20a visualizes the general construction and application of the acid saw.

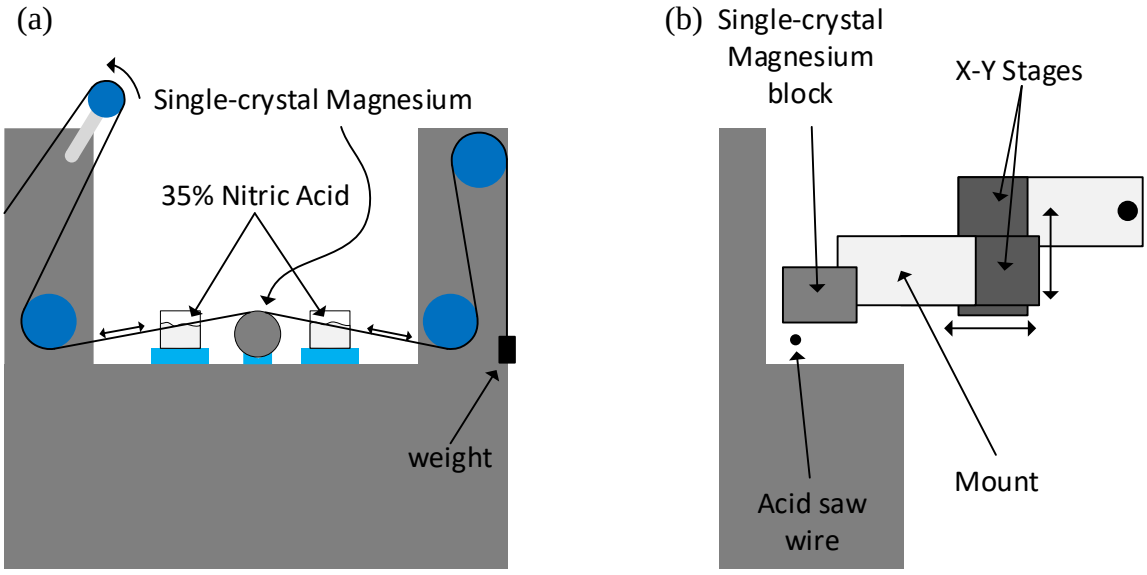

Figure 20: Acid saw configurations for cutting (a) blocks from mounted material, and (b) testing specimens.

The cutting is driven by the tension in the wire over the surface of the material. As the wire makes its way through the material approaching its neutral alignment, the tension in the wire is reduced. As the wire nears its neutral alignment, which is related to the height of the acid basins, the stage containing the two basins can be manually lowered to increase the tension in the wire. To make a testing specimen, several cutting steps by acid saw must be performed.

4.1.3 Specimen Manufacturing and Preparation

Specimens are manufactured in two steps. The first step is to section out rectangular plates from the cylindrical bar of material. The bar is reduced into smaller sections of 25 mm – 30 mm length. The larger bar is mounted using mounting putty such that the wire should cut along the basal plane of the crystal. Mounting reduces the chance of the material moving during the cut, as the wire can become stuck or break within thicker materials. In cases where the wire breaks, mounting also allows for easy realignment of the wire to cut nearly along the same path. These smaller cylindrical blocks are then remounted to cut parallel to the desired observation plane. A mounting rail modification allows for easy parallel cutting. These cuts yield rectangular plates of ~5 mm thickness. While specimen thickness is designed around 2.2 mm – 3 mm, extra material is necessary from this step. The cut quality in these larger blocks is very inconsistent, so additional manual removal of material is necessary to get the plates flat prior to cutting specimens. In particular, the rectangular block cuts can be wavy. To flatten the surfaces, manual grinding is performed using 400/P800 silicon carbide paper lubricated with ethylene glycol. Specimens will be cut from the flat rectangular plates.

Modifications were made to the acid saw to cut the specimens to the desired dimensions. First, a hole was cut from a hollow section of the acid saw between the two acid basins to provide additional space for the cutting process. Additionally, only one acid basin is used as using both bins provide too much acid to the thin plate, severely corroding the final specimen. Second, two one-dimensional stages of 50 mm range and 0.05 μm resolution were set up in series to allow for x- and y- directional control. An aluminum mounting attachment used to hold the rectangular plate was connected to the x-y stages. To prevent twinning by compression perpendicular to the crystal *c*-axis, double sided tape was used to carefully mount the plate. This acid saw configuration is visualized in Figure 20b. Each stage is controlled independently using a proprietary computer program. The programs run a series of "move and hold" steps that can be imported from a .csv file. For a plate thickness of ~ 3 mm, each step provided movement of 0.1 mm and holding of 3 minutes averaged over the vector of the combined movement. To best replicate the desired specimen dimensions, individual steps moved no further than 0.05 mm, and an additional 0.1 mm was added to the length and width of the specimen. These small steps add tension to the wire to drive the cut.

As-cut specimens require additional manual grinding to remove corrosion effects and flatten the specimen's side dimensions for proper fit and alignment in the testing apparatus. Both flat surfaces are also then lightly ground to remove any corrosion before one side is prepared for both *in situ* observation and *ex situ* EBSD analysis. Standard metallographic procedures are followed starting with manual P1000 to 1200/P4000 silicon carbide grit papers with ethylene glycol lubrication. Polishing was done using 6 μm and 1 μm oil-based

diamond suspensions. Final polish was achieved using 50 nm alumina-based suspension followed by etching with 3% nital (30 mL ethanol, 1 mL nitric acid). Nital was found to reveal most surface defects, such as polishing twins, so several cycles of final polish and etching was required for a clean surface.

4.2 *In situ* Observation of Twinning in the Observation Area

After the testing specimen was machined and prepared for study, initial EBSD revealed a matrix Euler angles (90,86,59). Figure 21a summarizes the crystal orientation of the specimen, where the *c*-axis of the crystal is roughly aligned with the x-axis. This orientation is highly favorable for twinning, having a 4° misorientation between the *c*-axis and a loading axis. All six twin variants have a Schmid factor greater than 0.49 (Figure 21b), suggesting that all six variants may be observed over the course of multiple loading and unloading cycles. For reference, the largest Schmid factor for the basal slip system is 0.0696.

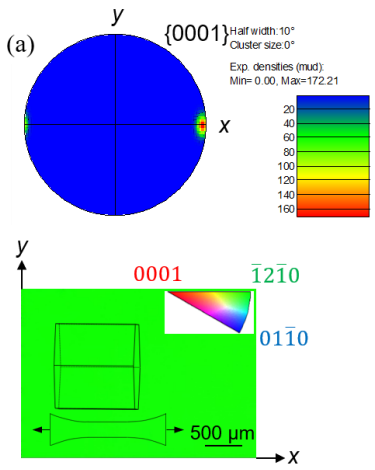

(b)

Variant	Twin Plane	Schmid Factor
T_1	$(10\bar{1}2)$	0.4986
T_2	$(01\bar{1}2)$	0.4986
T_3	$(\bar{1}102)$	0.4966
T_4	$(\bar{1}012)$	0.4909
T_5	$(0\bar{1}12)$	0.4908
T_6	$(1\bar{1}02)$	0.4965

Figure 21: Single-crystal magnesium specimen's (a) actual orientation and (b) Schmid factor values for the six possible tension twin variants

4.2.1 Microstructural Development during [0 0 0 1] Tension

To maximize the optical data for loading cycle, an OM area of 3120 x 2340 μm^2 with a resolution of 2 μm was chosen for the *in situ* observation. To also track the areas outside of the observation area, stitched images of the gage section are taken between cycles, while higher magnification micrographs are taken in areas of interest. *Ex situ* EBSD scans replicating the observation area of 3.1 mm x 2.3 mm with a step size of 4 μm and other areas of interest are also taken between loading cycles. A slower loading and unloading rate of 0.1 mm/min was used for single-crystal study to lengthen deformation processes. *Ex situ* EBSD was performed at interrupted plastic strains of 0.57%, 1.21%, 1.89%, 2.23%, 3.28%, and 3.83%. It is also noted that the load cell is properly calibrated for this experiment.

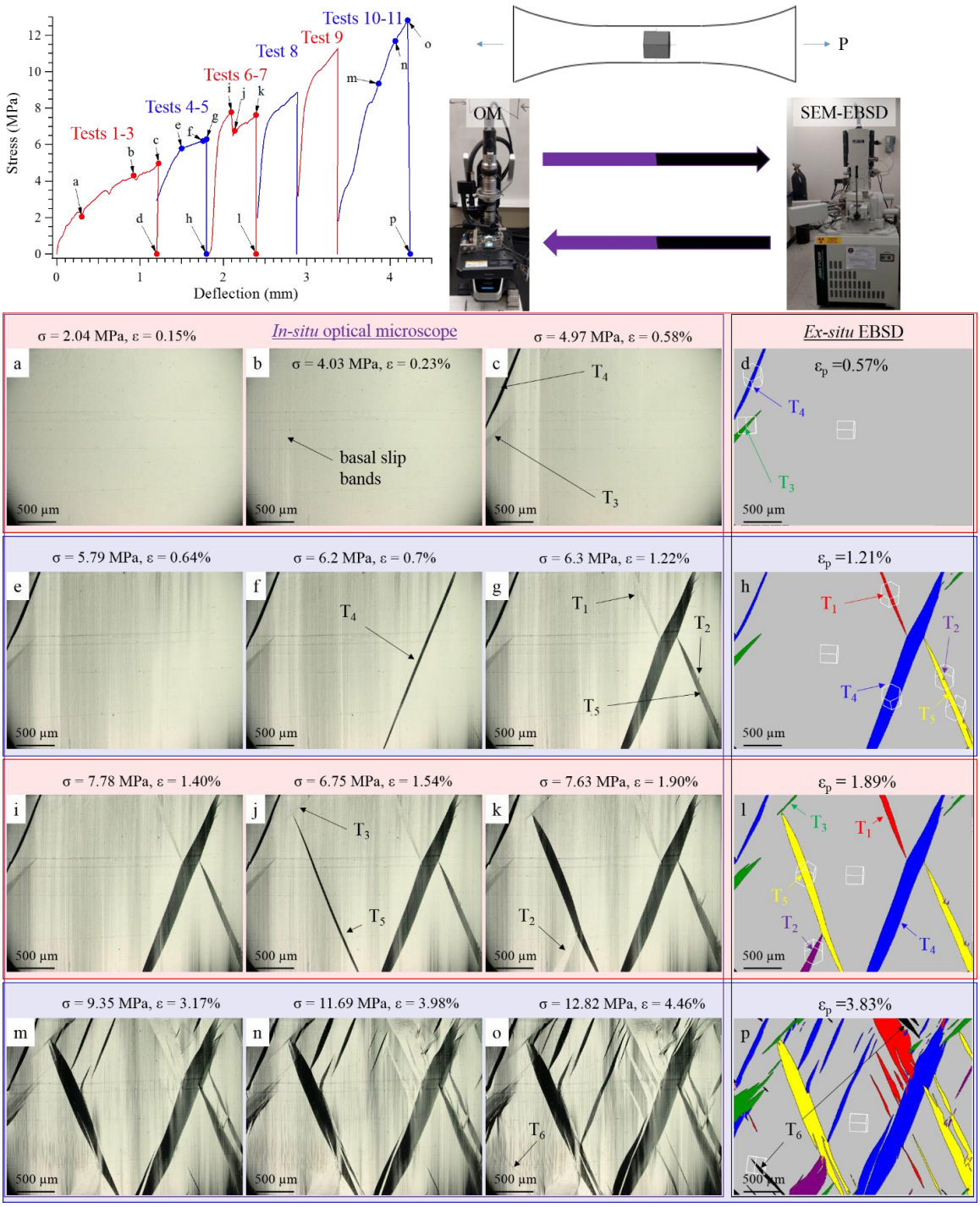

Figure 22: Combined *in situ* OM, *ex situ* EBSD observation of deformation in single-crystal magnesium subjected to nearly [0001] tension. Each test is a single loading-unloading cycle. Tests are combined into loading sets between which EBSD is performed.

Yielding and some plastic deformation shortly thereafter are captured by the first three loading steps (Figure 22a – 22d). First signs of plastic deformation are vertical basal slip bands at around 4 MPa of applied stress (Figure 22b). This corresponds to a resolved shear stress of 0.28 MPa, which is roughly half of the smallest reported CRSS 0.5 MPa from Table 1. Two twin variants are observed shortly after at around 5 MPa of applied stress (Figure 22c), where both twins propagate from the left edge of the frame. Additionally, the basal slip bands can be seen propagating from left to right within the observation area. After unloading and observing the full gage section, both observed twins appear to have nucleated from the edge of the specimen. *Ex situ* EBSD identified these twins as T_3 and T_4 (Figure 22d). Because some variants can result in similar colors in the IPF map, a custom color scheme is applied to the EBSD maps where the matrix is made gray, T_3 green, and T_4 blue. The measured CRSS here of ~2.4 – 2.5 MPa is consistent with the CRSS reported in literature (2 – 5.5 MPa from Table 2).

The first major twinning event in the observation area is observed during the second loading set (Figure 22e - 22h), where a large twin spanning the height of the occurs at 6.2 MPa of applied stress (Figure 22f). Two additional twins are then seen propagating to the initial long twin from out of frame, forming two possible twin-twin interactions (Figure 22g). The T_4 boundaries deviate from their coherent twin plane, likely resulting from the interactions formed. EBSD identifies the large initial twin as T_4, while the two smaller twins are identified as T_1 and T_5, thus a type I and type II(a) interactions are occurring. T_3 twin bands can also be seen in the upper right corner of the frame, while two sets of small T_2 clusters can also be seen nucleating from the T_5 twin band. After unloading, the larger

T_1, T_4, and T_5 twins can be seen originating from the edge of the specimen just slightly outside of the observation area. Additionally, persistent basal slip bands are evident, even within the twinned regions.

A third loading set (Figure 22i - 22l) captures another two twin-twin interactions between T_5 and T_2, and T_5 and T_3. The type II(b) interaction between T_3 and T_5 occurs first (Figure 22j). T_5, nucleating from the edge of the specimen, propagates rapidly to T_3, which acts as a barrier to the propagation of T_5. It is noted that T_3 also nucleated from the top edge of the specimen. As T_5 thickens, its tip does not grow or extend, causing a large deviation of its coherent plane near the interaction site. The type I interaction occurs slightly after the type II(b) interaction. T_2 propagates from the bottom edge of the specimen towards T_5, where they initiate contact and form the type I interaction. After additional strain, T_5 appears to encompass the tip of T_2, giving the appearance of a partial penetration of T_2 in T_5 (Figure 22k). The T_5 boundaries appear to deviate from their coherent plane near the type I interaction as well, where T_5 appears to thicken more near the interaction on the same side.

By the end of the final loading set (Figure 22m - 22p), all six tension twin variants are observed in the observation area. The twin shear can be seen by the deflection of the basal slip bands within the twinned regions, where the deflection angle varies by twin variant. Despite the similar Schmid factors, some twins are more prevalent than others are. T_1 has a twin volume fraction (TVF) of 4.5%, while its co-zone pair T_4 accounts for 12.6%. T_2 and T_5 account for 2.5% and 7.9%, respectively. T_3 and T_6 account for 2.3% and 0.7%, respectively. In total, all six variants cover 29.1% of the scan area.

Additionally, several trends associated to the nucleation, propagation, and growth of new twins can be deduced. One such trend is the commonality of parallel twins of the same variant, though not to the degree observed from twin-favorable compression. Some cases are very clear where there is significant spacing between the parallel twins, such as the T_5 variants in the bottom quadrant of the frame. Other cases are more subtle as the space between the twins gets smaller or where a large portion of the boundaries have coalesced. Evidence of these cases can be reduced to the fork-like twin-tips at the barrier twins. Additionally, many of the newer parallel twins are developed from twin boundaries as opposed to the edge of the specimen, and do not reach a barrier twin or surface. While the prevalence of twin-twin interactions and increased stress state can explain the increased nucleation of new twins, it is also noticed that many of the new parallel twins contribute to the development of twin-twin structures. An example of this is the interaction between T_4 and T_5 that was initially observed in Figure 22g, where the formation process is consistent with literature [60,116,117]. However, by the final loading frame (Figure 22o), T_5 appears to penetrate into T_4, in part due to the nucleation, propagation, and growth of parallel twins near the interaction site. Using the *in situ* recordings and *ex situ* analyses, detailed analysis of key deformation processes, such the nucleation, propagation, thickening, and interaction of twins, can expand on the current understanding of the field.

4.2.2 Detailed Analysis of Deformation

In situ observation confirmed that yielding occurs by basal slip followed by the activation of tension twinning. Figure 23 details the inhomogeneous deformation as a result of the basal slip propagation during yielding. *In situ* observation revealed basal slip bands

at around 4 MPa applied stress towards the left side of the observation area. This corresponds to a CRSS of 0.25 MPa, which is roughly half of the reported value in literature (0.5 – 1 MPa in Table 1). Before significant propagation of the basal slip bands, the first two tension twins are seen growing into frame from the left edge of the observation area. Before any other twinning phenomena are observed in the observation area, the basal slip bands are seen spanning the entire frame. It is noticed that the initial basal slip bands remain persistent within the twinned regions, although they are deflected by some small angle.

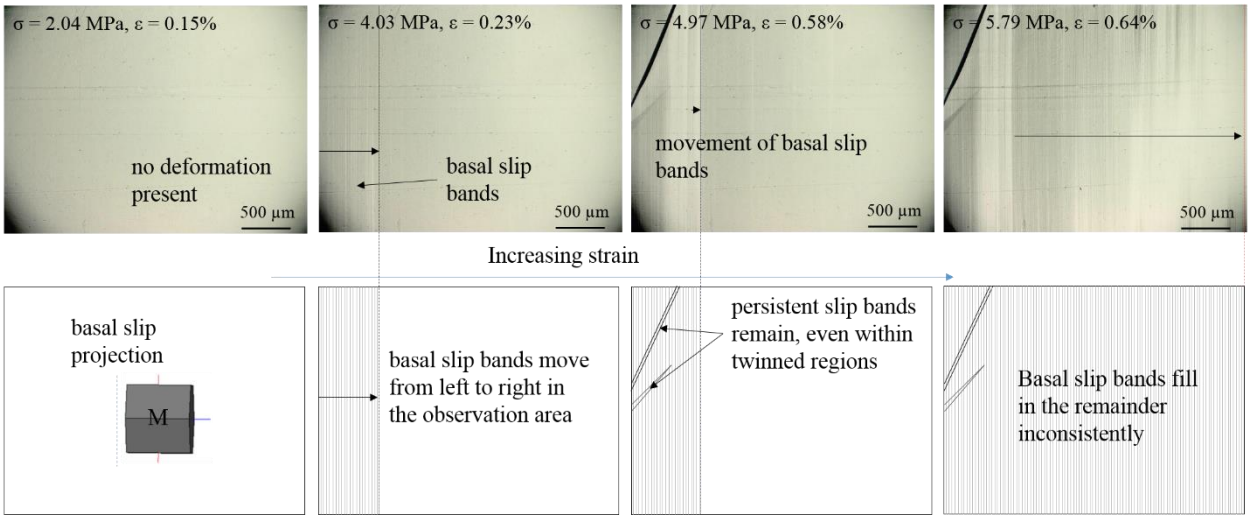

Figure 23: *In situ* observation of slip band propagation from left to right during yielding

Figure 24a shows the basal slip bands deflected within a T_3 band. In general, the deflection due to tension twin shear is determined by the activated variant, where in-plane rotations result in the largest measured angle up to 3.7° in a perfectly aligned crystal (Figure 24b). Thus, since T_3 results in almost a perfect in-plane rotation, it results in the largest deflection angle of ~3.7°. Using Molodov et al.'s [155] method and the measured deflection in T_3, θ_m, the shear due to twinning is estimated to be 0.1295. This matches very well with the theoretical value 0.1294 using the equation from Table 1.

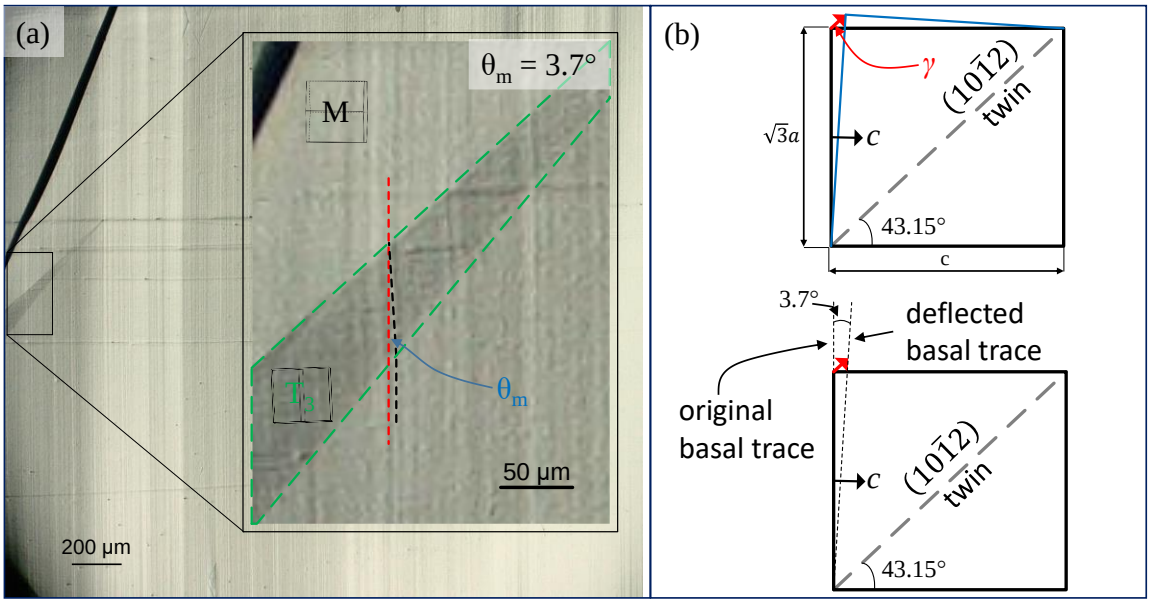

Figure 24: (a) Deflection of basal slip bands within T_3 due to twinning shear. (b) A schematic showing the deflection angle resulting from twin shear.

The next significant twinning effect occurs when T_1, T_4, and T_5 develop in the second set of loading cycles. Figure 25 details the how these three twins accommodate strain. Prior to *in situ* observation, T_4 is nucleated from outside the observed area, likely from the edge of the specimen. After one frame, it is found with an initial length of 270 μm (Figure 25a) before propagating by 200 μm and thickening by 6μm after an additional frame (0.067 second). At a slight increase in strain, T_4 propagates past the observation area with significant growth and thickening, while a new twin, T_5, enters frame (Figure 25b). This rapid growth of T_4 corresponds to a twin tip velocity of greater than 30 mm/second. Limited studies have examined the twin growth rate. Twin boundary growth rate in magnesium has been reported at 35 x 10^{-9} m/second [156], while twin tip velocity has been reported at a much higher rate of 1 km/second [150,157]. However, there is little consistency between testing procedures to make an adequate comparison to the results made here. Both twin tip

velocity studies apply high strain rate loading in the order of 10^3 – 10^5 s^{-1}, and twin tip profiles are measured by post mortem methods [157] or by *in situ*, high speed camera with a frame rate of 5 million frames/second [150]. Alternatively, the strain rate applied here is much lower in the range of 10^{-6} – 10^{-5} s^{-1} and limited to a much lower frame rate of 15 frames/second.

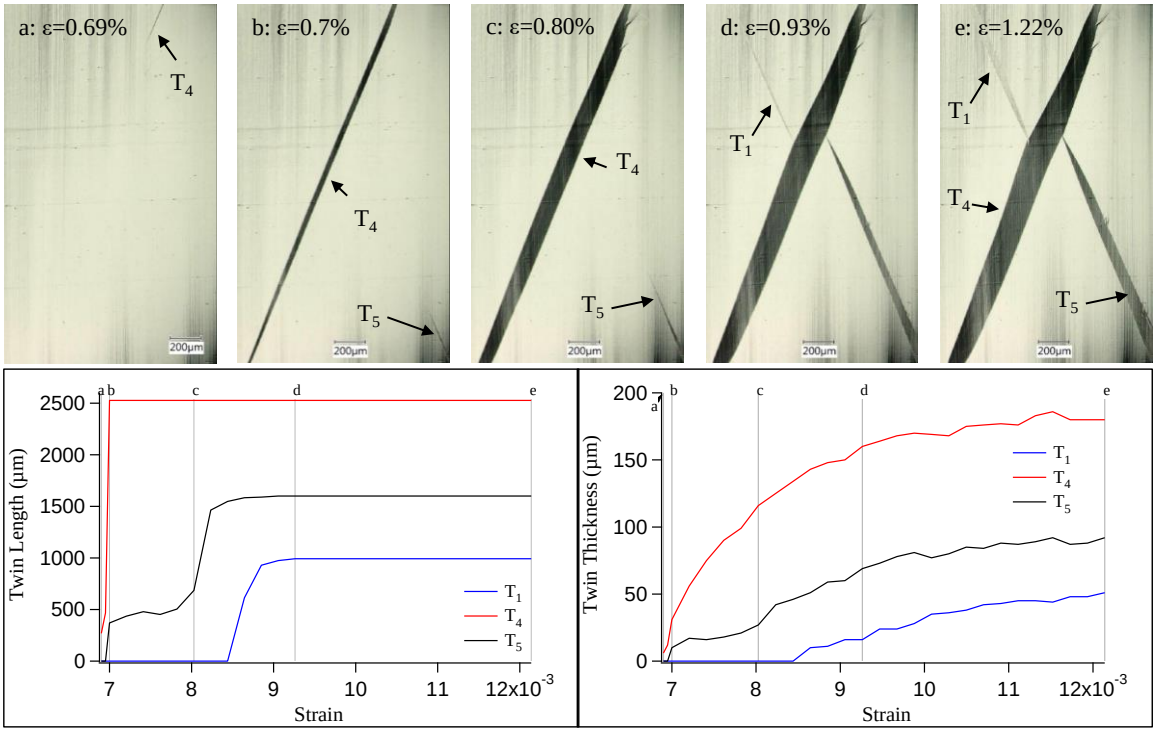

Figure 25: Twin growth and thickening development of T_1, T_4, and T_5 twin variants.

Over an additional 4.0 seconds (Figure 25c), or 0.08% strain increase, T_4 steadily thickens to 100 μm while T_5 experiences a minimal growth (136 μm). The twin length and thickness graphs show that the thickening of T_4 accommodates most of the strain during this process. With further straining, the development of T_5 accelerates, which results in the increased length and thickness of T_5 while the thickening rate of T_4 is reduced. Subsequently, a T_1 twin rapidly propagates to the T_4 boundary (Figure 25d). After the two

possible twin-twin interactions are formed, strain is accommodated by the gradual thickening of all three variants. However, because of the interactions formed, most of the thickening occurs away from the interaction sites resulting in incoherent twin boundaries. After a certain point, the nucleation, propagation, and thickening of new twins is required to accommodate additional strain as seen in the microstructural development in Figure 22.

Evidence of cyclic loading effects were present with the later tests where the stress unloading increased. Evidence of partial detwinning during unloading was found, especially when unloading from larger peak stresses. This detwinning is related to the Bauschinger effect. In highly textured magnesium alloys, the Bauschinger effect is described as the reduced flow stress during a reversed loading than the forward loading [158]. The result is a reduced yield stress in the reversed loading compared to the forward loading. Studies of Bauschinger effect in cubic materials have explained the phenomenon using dislocation structures, dislocation interactions, and back stresses [159–163]. In steels, it was found that when twinning was the primary deformation mechanism, a large Bauschinger effect was observed when the loading was reversed. Extending the observations to magnesium, Bauschinger effect was attributed to the twinning-detwinning process [88], and has been observed during unloading [164]. Additionally, it has been reported that the accumulation of dislocations from slip can reduce the Bauschinger effect, especially with large pre-strain [83]. This can be exasperated by the twin favorable loading where the reorientation by twinning favors the easy activation of basal slip within the twinned region. Dislocations will then converge and accumulate at or near the twin

boundary, which may further reduce the Bauschinger effect. Figure 26 highlights three measurable partial detwinning cases.

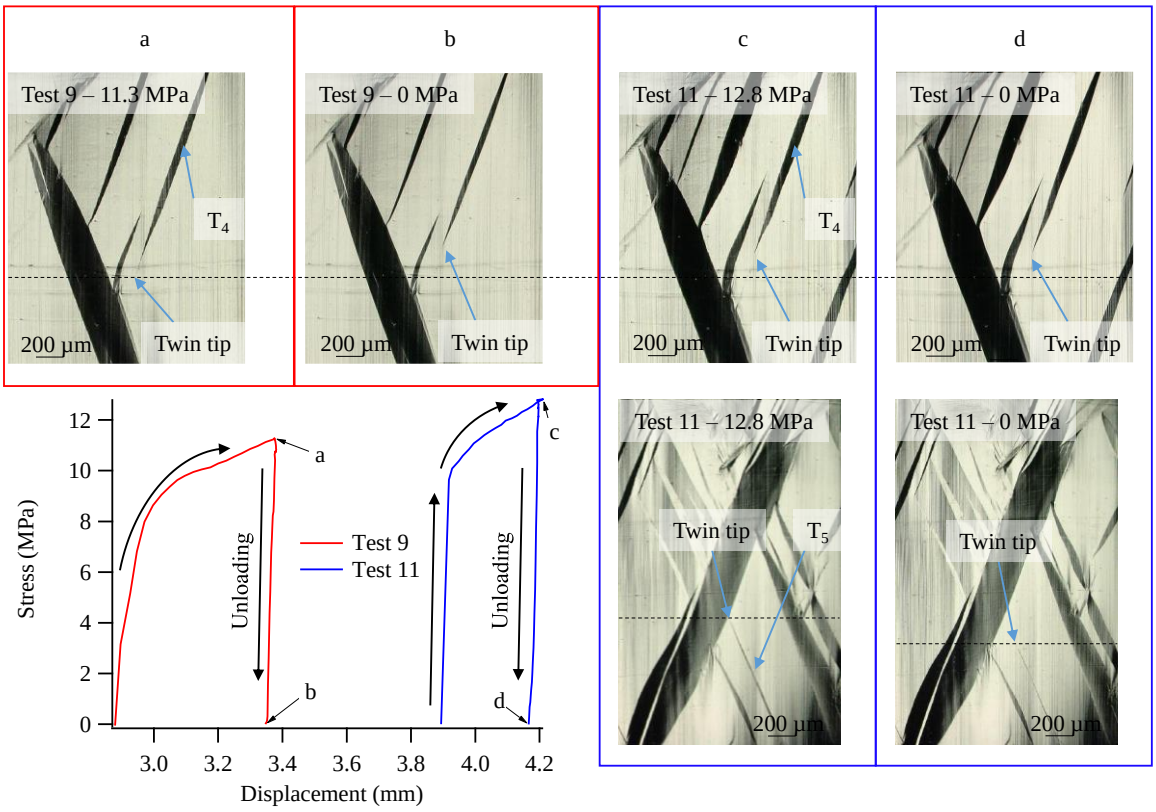

Figure 26: Three cases of partial detwinning resulting from unloading. (a-b) Unloading from 11.3 MPa results in the shortening of one T_4 twin. (c-d) Unloading from 12.8 MPa resulting in the shortening of two twin bands – T_4 and T_5.

Further focusing on the detwinning of a T_4 twin in Test 9 (Figure 26a – 26b), some additional details can be revealed (Figure 28). To measure the dimensional changes, a horizontal line through a clearly identifiable point in the observation area was used for reference. The micrographs in Figure 27 were cropped at this line. Length measurements were taken from the twin tip to the center point of the twin base along the reference line. Twin thickness was measured between the coherent parts of the twin bands. Unloading

from 11.3 MPa, initial detwinning from the narrow twin tip begins after the elastic portion of unloading when stress drops to 5.22 MPa. The remaining unloading corresponds to the plastic deformation by Bauschinger effect, and thus activates detwinning. With increasing strain, the amount of stress unloaded is increased. Thus, the lack of detwinning in previous loading sets can be attributed to not reaching the plastic deformation range in unloading. Additionally, that explains the increased detwinning observed from the larger stress in Figure 26c – 26d.

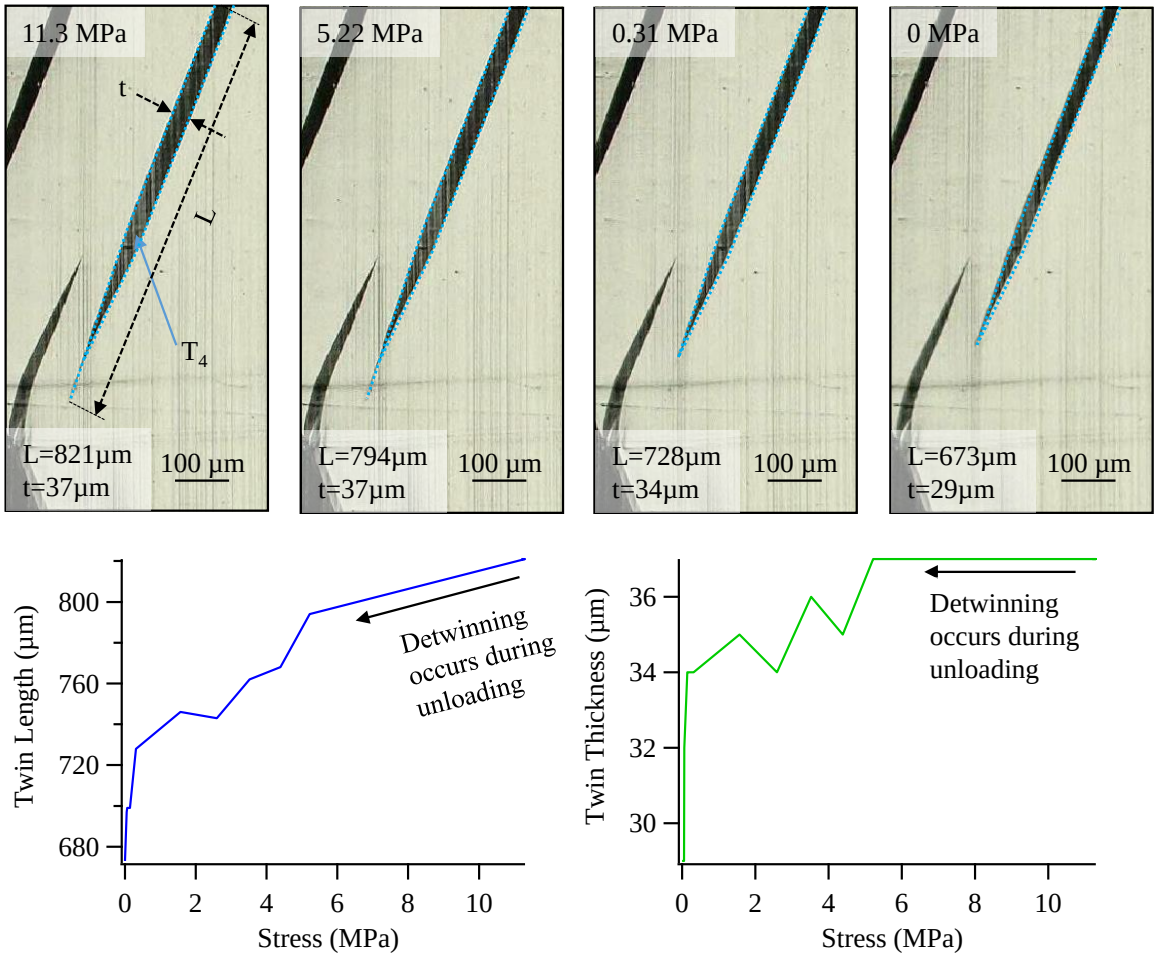

Figure 27: Detailed observation of T_4 twin detwinning during unloading from 11.3 MPa.

4.3 Twin-Twin Interactions

To re-summarize from Chapter 2, three types of twin-twin interactions can occur. There is the Type I co-zone interaction and the Type II(a) and Type II(b) non-co-zone interactions. There are also three types of twin-twin boundaries (TTB) resulting from a twin-twin interaction. The first is the acute angle boundary, TTB_A, the second is the impinging twin-twin boundary, TTB_I, and the third is the obtuse angle boundary, TTB_O. The favorability and formation processes of these TTBs vary by the type of twin-twin interaction.

4.3.1 Type I Co-Zone Twin-Twin Interaction

A Type I interaction occurs when co-zone variants interact in the form of $T_i \leftrightarrow T_{i\pm3}$. In the Type I interaction, TTB_A is energetically favorable to form by the zipping of the two twins' twinning dislocations [60,115]. The result is a boundary that bisects the two coherent twin traces. TTB_I is rarely reported, although it can form by the deposition of twinning dislocations from the impinging twin on the barrier twin boundary. This boundary's difficulty lies in its visibility, as it may be seen optically but is difficult to observe clearly by EBSD due to the low misorientation angle of 7.4° between the co-zone pair. TTB_O was suggested to occur by the dissociation of twinning dislocations from one twin onto the other, but is considered energetically unfavorable [60]. This leads to a diversity of Type I interaction structures, as one or more twin-twin boundaries may occur. When both TTB_O and TTB_A are formed (Figure 28a, highlighted with by a red arrow), the resulting structure is a wedge-shaped partial penetrating structure [60,115,165]. In one unique case where only one TTB is formed (Figure 28b), a needle, or knife-like, deep penetrating structure

was observed by transmission electron microscopy [166]. It is noted that this structure was observed at the nanoscale, and the proposed formation process was unclear. Roberts and Partridge [116] have optically captured a possible penetration structure, but due to the accommodation kinking and lattice re-orientation, they could not separate the two twin variants. Almost all the experimentally observed penetrating structures were identified by post-mortem analyses.

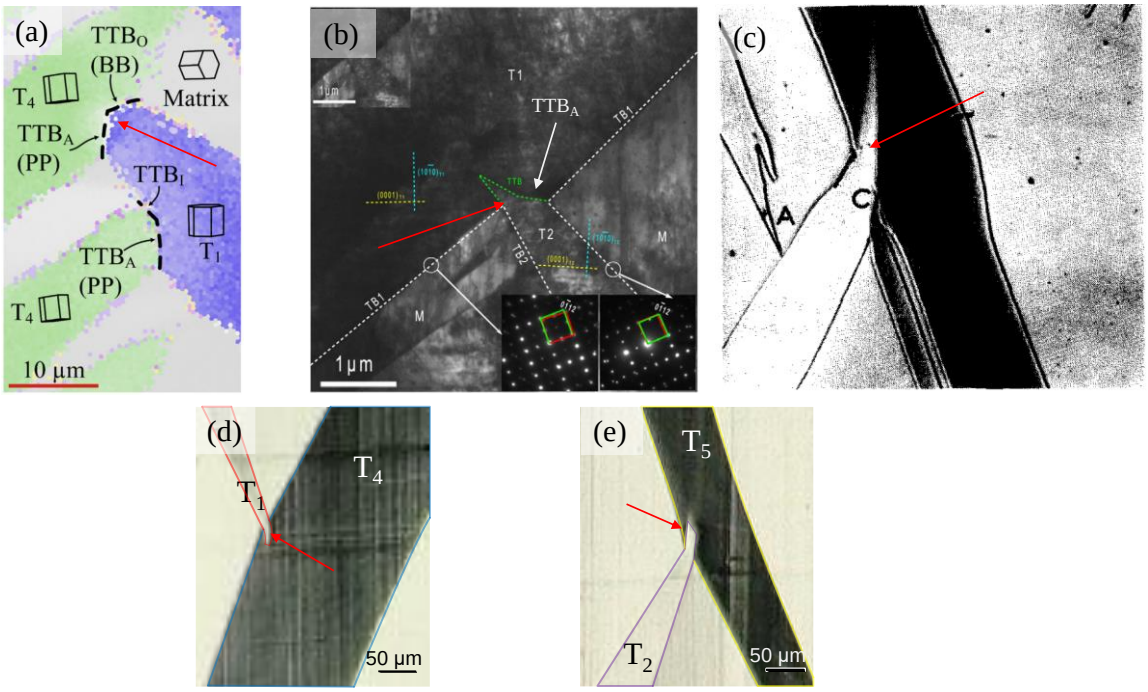

Figure 28: Intrusion-like structures resulting from Type I co-zone interactions; (a) wedge-shaped partial penetrating structure resulting from formation of TTB_A and TTB_O [60,115]; (b) nanoscale deep needle, or knife-shaped penetration where only TTB_A is developed [166]; (c) Possible penetration structure [116]; (d, e) two deep blade-like penetration structures captured by *in situ* observation

Two intrusion-like structures were observed *in situ* during the nearly *c*-axis tension in single-crystal magnesium (Figure 28d and 28e). The first observed case occurred during

the second loading set (Figure 22e – 22h) during the interaction between T_1 and T_4. The second intrusion-like structure occurred during the third loading set (Figure 22i – 22l) from the interaction between T_2 and T_5. The interaction between T_2 and T_5 has no other twinning nearby and was thus more closely to explain the formation process. The *in situ* development is presented in Figure 29, where the impinging T_2 propagates towards the barrier T_5 ($T_2 \rightarrow T_5$). Additionally, a schematic delineating the formation process is provided in Figure 30. Time stamps taken from the Test 7 recording are used to reference when these events occur. Development of the interaction occurs 23 seconds after the test starts, where T_2 is seen propagating toward T_5 (Figure 29a and Figure 30a).

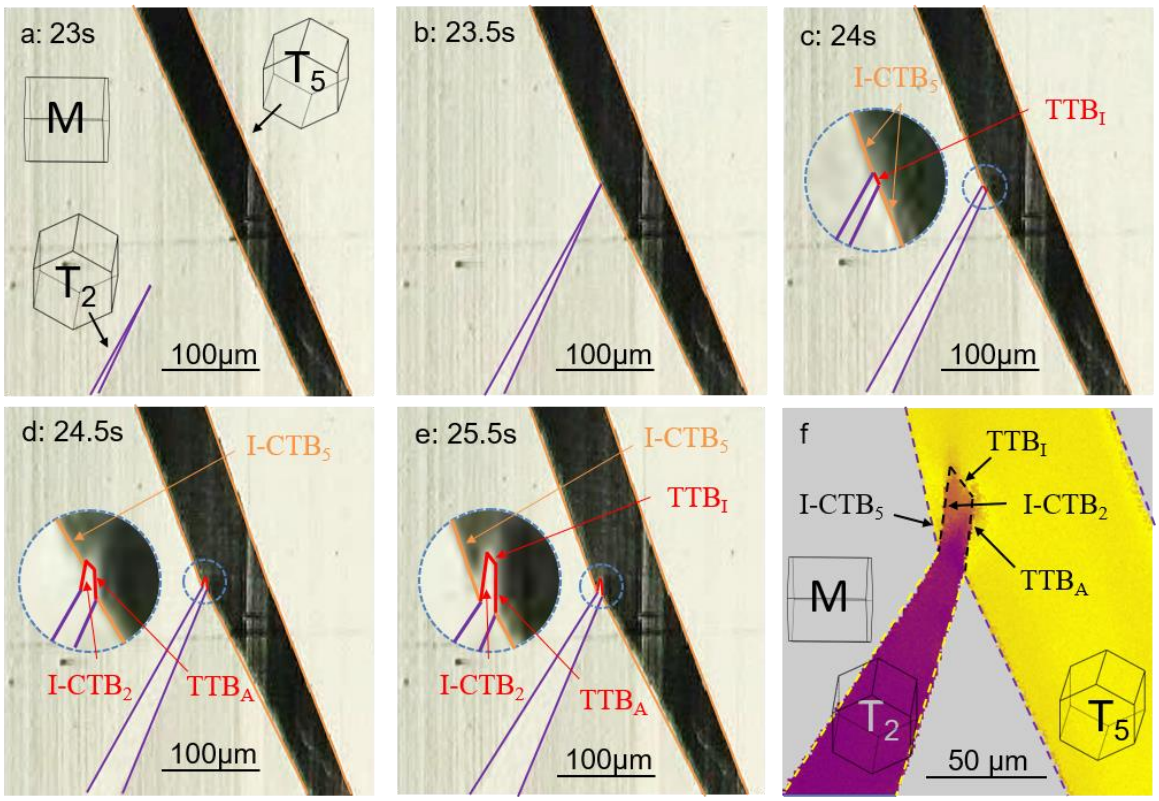

Figure 29: *In situ* formation of an intrusion-like twin-twin structure resulting from a $T_2 \leftrightarrow T_5$ Type I interaction [11]

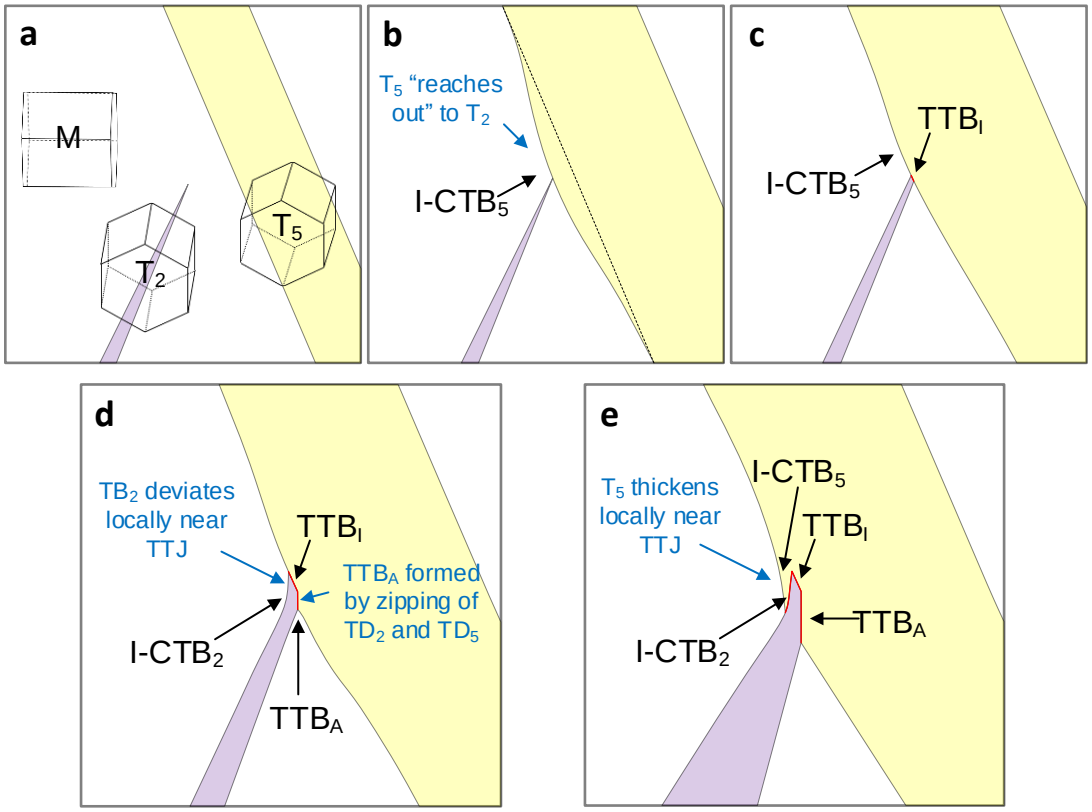

Figure 30: Schematic delineating the formation process for the intrusion-like co-zone twin-twin structure [11]

Initial contact is observed around 23.5 seconds (Figure 29b and Figure 30b), where the needle-like tip of T_2 meets the T_5 boundary. It is noted that the T_5 boundary deviates from the coherent twin boundary (CTB) as it reaches out to contact T_2. This "reach out" effect, which was first reported by Morrow et al [56], can be succinctly summarized using Arul Kumar's twin resolved shear stress (TRSS) obtained by molecular dynamic simulations [167]. At a critical distance between the two twins, the TRSS in T_2 is negative, and will thus stop propagating. Alternatively, the TRSS in T_5 will be positive and sufficiently large near the tip of T_2, thus driving the local thickening of T_5 by boundary migration. Therefore, instead of T_2 growing toward T_5, it is more accurate to say that T_5 locally thickens towards

T_2, as emphasized in Figure 30b. Additionally, because of the local deviation from the coherent twin boundary (CTB), TTB_I is affected as seen in Figure 29c where TTB_I does not align with CTB_5. TTB_I itself is formed by T_2 thickening along the T_5 incoherent twin boundary (I-CTB) on the obtuse angle side. With further growth of T_2 and T_5, TTB_A is formed by the energetically favorable zipping reaction of the twinning dislocations from T_2 and T_5 (Figure 29d). The trace of TTB_A approximately bisects the coherent twin traces of T_2 and T_5, which is consistent with previous works [60,115], where the TTB_A plane bonds the two twins' prismatic planes (termed as PP boundary). Thus, the formation of TTB_I and TTB_A are consistent with reported literature.

On the obtuse angle side of the interaction, TTB_O does not form by dissociation. Yu et al. [60] identified that TTB_O is energetically unfavorable in Type I interactions, despite observing the boundary by *ex situ* EBSD. They rationalized that TTB_O is unfavorable when only considering the elastic energy associated with the reaction on the obtuse angle side. However, reducing the net elastic energy, for example by the formation of dislocation walls, can increase the favorability for TTB_O formation. Lacking this reduced net elastic energy; T_2 instead thickens locally and transitions into $I\text{-}CTB_2$ adjacent to the TTB_I on the obtuse angle side. This is supported by large-scale molecular dynamics simulation (Figure 31 [167]), where the local distribution of TRSS for T_2 on the obtuse angle side is positive near the interaction point (highlighted by the white arrow). This means local nucleation and glide of T_2 twin dislocations is favorable, leading to the deviation of the T_2 twin boundary on the obtuse side as evidenced in Figure 29d.

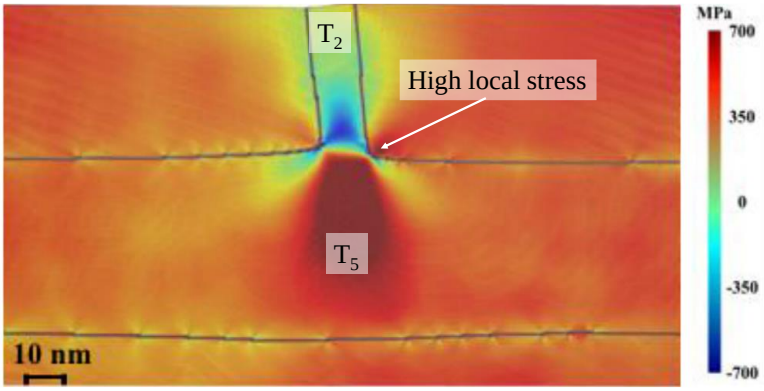

Figure 31: T_2 twinning resolved shear stress profile during a $T_2 \leftrightarrow T_5$ Type I interaction obtained by molecular dynamic simulations (modified for the present interaction from [167])

Shortly after, as indicated in Figure 29e and Figure 30e, the T_5 boundary locally migrates on the obtuse angle side along I-CTB_2, shaping the intrusion-like twin-twin structure. With further loading, TTB_A continues to grow while on the obtuse side, I-CTB_5 continues its migration along I-CTB_2 enlarging the intrusion structure. EBSD after unloading confirms the penetrating T_2 variant being surrounded by the barrier T_5 variant (Figure 29f). The color gradient seen in the IPF map indicates local variation of crystal orientation due to the high local stress concentration. As shown in Figure 29f, TTB_A has grown significantly, while I-CTB_2 and I-CTB_5 are more clearly observed on the obtuse angle side, forming a deep intrusion-like twin-twin structure. The summarized formation process, schematically presented in Figure 30, explains the boundary formation process that results in a penetrating co-zone twin-twin structure. Additionally, it may also explain the penetrating structures observed in literature by *ex situ* methods, such as those shown in Figure 28b and Figure 28c.

4.3.2 Type II Non-Co-zone Twin-Twin Interactions

As with the Type I co-zone interactions, the development of non-co-zone interactions has primarily been studied by *ex situ* study. There are two types of Type II interactions: Type II(a), forming from a $T_i \leftrightarrow T_{i\pm1}$ interaction, and Type II(b), forming from a $T_i \leftrightarrow T_{i\pm2}$ interaction. For both Type II interactions, previous studies noted that TTB_A formation is energetically unfavorable while TTB_O formation is favorable [60,117]. Beginning with the Type II(a) interaction, experimental observations of this formation are presented in Figure 32a [116] and 32b, while an atomistic simulation suggesting the formation process [117] is provided in Figure 32c.

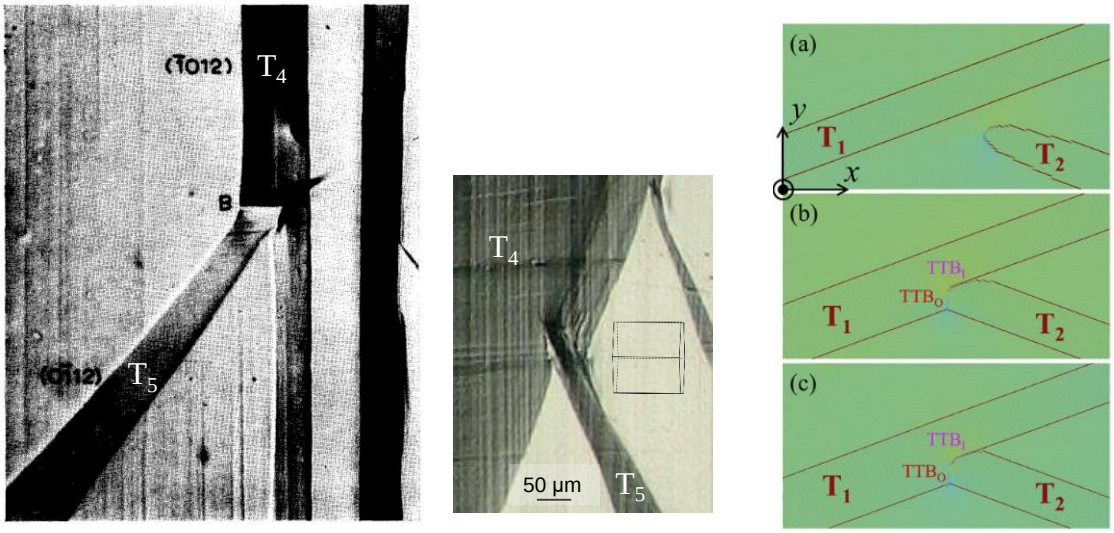

(a) Reported type II(a) interaction

(b) Observed type II(a) interaction

(c) Atomistic simulation of type II(a) interaction

Figure 32: Type II(a) twin-twin structure; (a) previously reported between a T_4 and T_5 variant [116]; (b) experimentally observed *in situ* $T_4 \leftrightarrow T_5$ Type II(a) interaction; (c) atomistic simulation of the formation process [117]

The similarities between the experimentally observed cases and the simulations are apparent. TTB_O is observed in both cases, while TTB_I is less noticeable and TTB_A is unobserved. In the *in situ* observed case (Figure 32b) was reported previously in the discussion of strain accommodation, though additional development is observed following the initial formation of the twin-twin interaction. As with the Type I interaction presented in Figure 29, the final result of this interaction appears as a penetration-like structure. To explain how the structure is formed, the *in situ* breakdown of this development is presented in Figure 33.

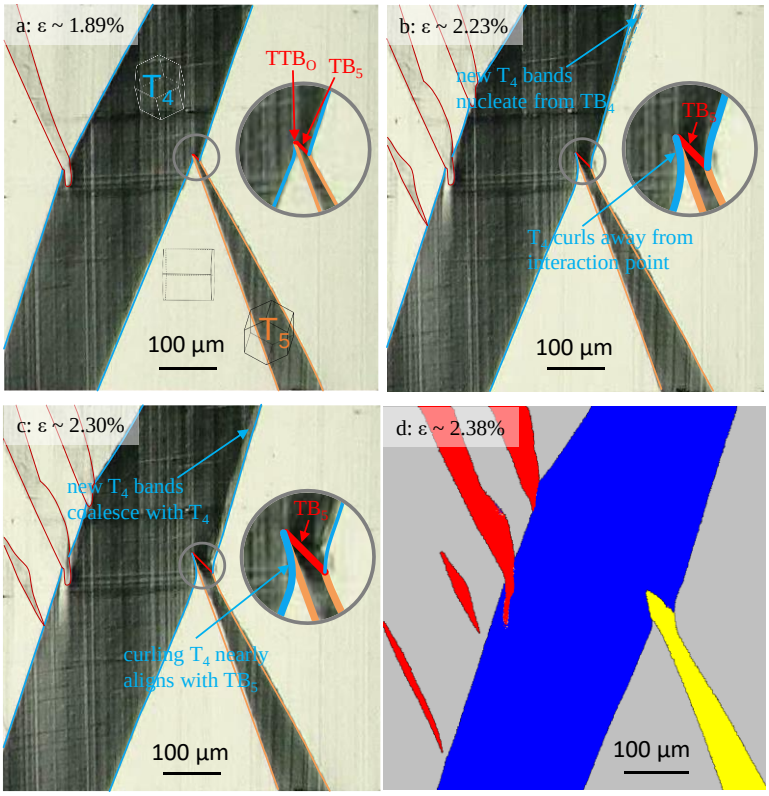

Figure 33: *In situ* development of the $T_4 \leftrightarrow T_5$ Type II(a) interaction.

The initial formation closely follows the atomistic simulations, where a slight TTB_I is formed upon contact. It is noted that "T_1" and "T_2" in the simulation are equivalent to T_4

and T_5 in the experiment. Shortly after, TTB_O is formed parallel to a prismatic plane of the matrix, which is consistent with the crystallographic analysis by Yu et al. [60]. As TTB_O bisects the coherent twin planes of the intersecting twins, TTB_O is formed by the zipping of the two twins' twinning dislocations. With increasing strain, TTB_O reaches a critical point and stops expanding. The T_4 boundary curves sharply some distance away from the interaction site. New T_4 twins are nucleated from the curved twin boundary, which then propagate and thicken, coalescing with the initial T_4 boundary allowing it to migrate along the T_5 boundary. On the acute angle side, T_4 thickens away from the intersection point, causing severe incoherency and curling nearly along T_5 such that the space between the two twin bands is invisible optically. With I-CTB_4 being almost parallel to and along the T_5 boundary, the appearance of a TTB_A-like boundary could be misconstrued. In the EBSD IPF map, this immeasurable spacing between T_4 and T_5 appear as a thick "boundary." This reaction is inverted from the simulation, where the equivalent T_5 is suggested to curve along the T_4 boundary. This minor difference is likely attributed to slight alterations in the real local stress compared to the simulation. But despite this, the experimentally observed formation of the Type II(a) interaction confirms the modeled formation by atomistic simulations.

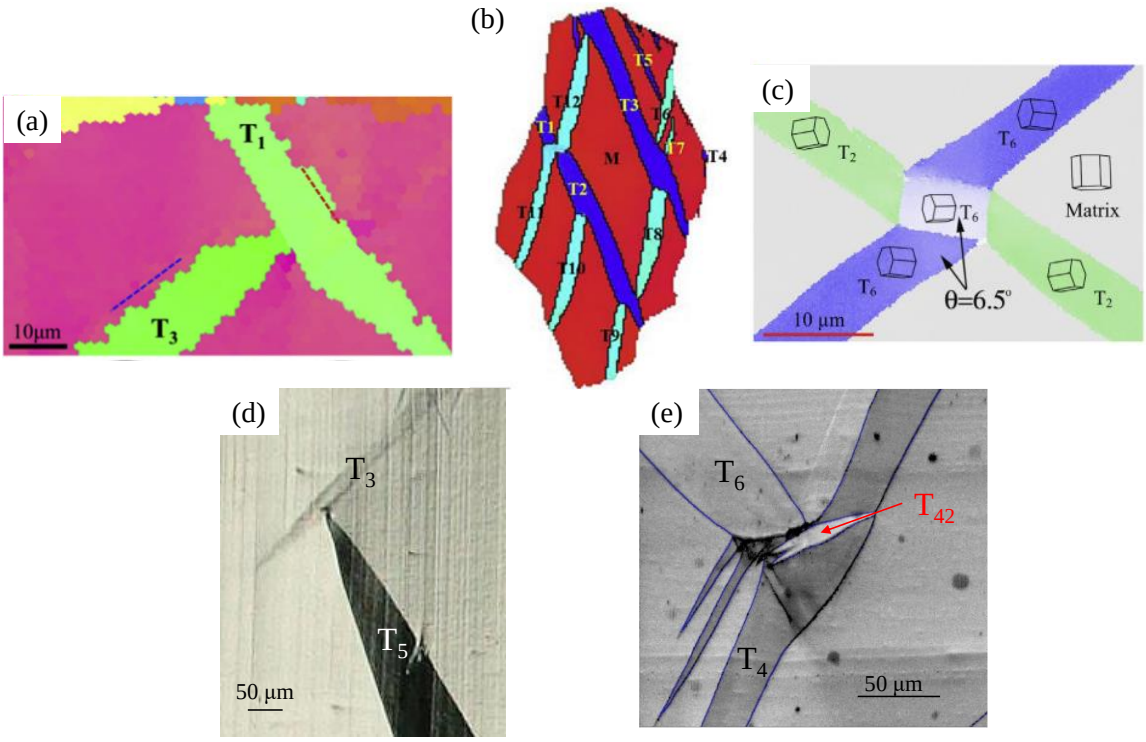

Figure 34: Experimentally observed Type II(b) interactions; (a) an impinging Type II(b) interaction within a grain [117]; (b) series of branching Type II(b) interactions within a grain [168]; (c) an apparent-crossing structure Type II(b) interaction with secondary tension twins [60]; (d) an impinging Type II(b) interaction observed by *in situ* OM; and (e) a partial apparent-crossing structure Type II(b) interaction with a secondary twin as observed by *ex situ* EBSD

There is diversity in the twin-twin structures resulting from a Type II(b) interaction. Figure 34a – 34c provides three cases reported in literature, while Figure 34d and 34e provide cases captured in this study. From the five presented cases, two have the approaching twin being impinged at the barrier twin boundary, while the other three show a partial or complete apparent-crossing structures. The difference between the two structures is the formation of the obtuse angle boundary. No TTBs are formed in the impinging structure (Figure 34a and 34d) and the approaching twin is impinged where its

tip meets the barrier twin boundary. This impinging twin can still grow away from its tip, causing most of its boundary to be incoherent. These impinging interactions are consistent with the molecular dynamic simulations at the nano-scale [117,169]. In the apparent-crossing Type II(b) structure, TTB_O is formed parallel to a matrix prismatic $\{2\bar{1}\bar{1}0\}$ plane corresponding to its associated reaction. This causes the "crossing" twin to "step" or cross along TTB_O before it continues growing. In a complete apparent-crossing structure, a second twin of the non-crossing variant is either nucleated or impinged on the other side on the interaction, forming an X-like crossing pattern (Figure 34b and 34c). How this second twin is introduced has not been reported.

In a partial apparent-crossing (Figure 34e) structure with T_4 and T_6, the second non-crossing twin that forms the "X" pattern is not formed. The initial formation involves T_6 contacting T_4 and forming TTB_O by zipping, which causes both twin boundaries to grow locally on the obtuse side. At some critical distance, the T_6 boundary begins to curl away from the tip of TTB_O. This curvature becomes the site for new T_4 twin nucleation. These T_4 twins assist in the further thickening of T_6 on the obtuse side of the initial interaction. On the acute angle side, no development occurs at the point of contact. Instead, T_4 is slightly detwinned away from the contact while T_6 thickens. This is evidenced by the concavity of T_6 and the convexity of T_4 with increasing strain. On the other side of the interaction, the T_4 boundary curves in the vicinity of the interaction, contributing to the appearance of the large step caused by TTB_O. Within T_4, a secondary twin, T_{42}, is formed near the interaction site and is ascribed to the high local stresses that are the reason behind the color gradients in the IPF maps of Figure 35.

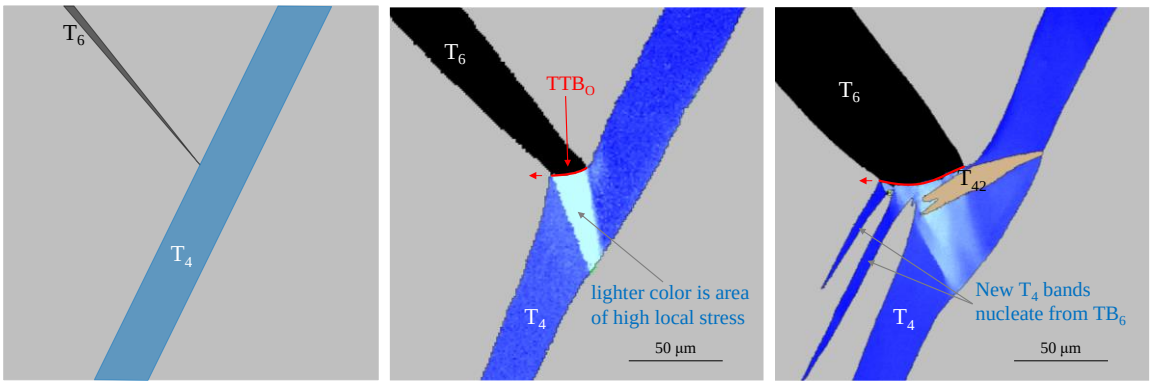

Figure 35: *Ex situ* observation of a partial apparent-crossing Type II(b) interaction. (a) Proposed initial interaction where a T_6 reaches the barrier T_4 twin boundary. (b) The obtuse twin-twin boundary is formed by the zipping of the two twin dislocation types. (c) Further expansion of the obtuse angle boundary is achieved through the nucleation of parallel T_4 bands from the twin-twin boundary, while a secondary twin is observed within T_4 in the high local stress area.

4.3.3 Tension-Tension Secondary Twinning

In single-crystal experiments subjected to monotonic loading, secondary tension twinning does not follow Schmid's law, as assuming the local stress follows the global stress will result in a negative resolved shear stress. As such, there are two possible explanations for secondary tension twin formation. The first possible explanation is that local stress effects due to twin-twin interactions or a build-up of dislocations assist in forming these secondary twins. The second possible explanation is that the Bauschinger effect during unloading provides a sufficient relative compressive stress to activate the secondary twins. As with detwinning, unloading from larger stresses may provide sufficient compressive stress to nucleate secondary twins, especially as the detwinning of interacting twins is difficult.

In addition to the secondary twin formed from the Type II(b) interaction shown in Figure 35, there is another interesting case resulting from a Type II(a) interaction. To the right of the observation area, a $T_4 \leftrightarrow T_5$ interaction results in parallel T_{52} secondary tension twins with no other twins in the vicinity (Figure 36a). In Figure 36b, T_4 approaches T_5 before multiple developments are observed in Figure 36c. First, two interactions of $T_4 \rightarrow T_5$ are observed on the right side of T_5. The top interaction is between the initial two twins, while the bottom is between a second formed T_4. Within T_5, T_{52} secondary twins connect to T_4 twins on the either side of T_5.

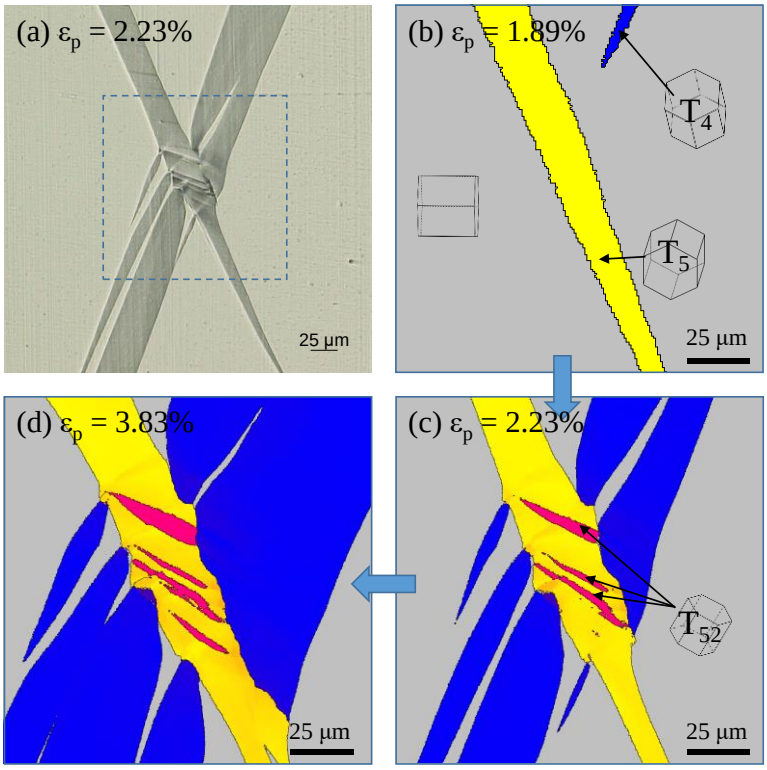

Figure 36: The formation of secondary tension twins from a Type II(a) interaction; (a) optical micrograph highlighting the area of secondary twinning and (b-d) the EBSD inverse pole figure maps showing the development at three plastic strain levels ranging from 1.89% to 3.83%. Note that the strain levels increase in counter-clockwise rotation.

4.4 Summary

Nearly *c*-axis tension to ~3.83% plastic strain was applied to single-crystal magnesium to study deformation twinning. A slow loading rate of 0.1 mm/min, or strain rate in the range of 10^{-6} – 10^{-5} s^{-1}, was used in an attempt to clearly capture twinning phenomena at 15 frames/second. Twin development, such as the nucleation, growth, and interactions of multiple twins, was tracked by *in situ* OM and intermittently characterized by EBSD. The summary of the significant observations and mechanisms are as follows:

1) All six tension twin variants were captured within the observation area by 3.83% plastic strain. While all six variants are highly favorable to form, the order of activation did not follow Schmid's law nor do their respective volumes with respect to their appearance in the observation area.
2) Prior to the activation of tension twins, inhomogeneous deformation by basal slip was observed, confirming previous reports in literature. Basal slip bands were captured propagating directionally within the observation area prior to the first evidence of twinning. The CRSS for basal slip was calculated to be 0.25 MPa based on the applied stress and Schmid factor, while the CRSS of tension twinning was estimated to be 2.5 MPa.
3) The initial basal slip bands remain persistent within twinned regions, but are deflected due to the twin shear. T_3 and T_6 rotate in plane, providing an almost perfect 3.7° deflection, which was used to confirm the twin shear, *s*, to be 0.1295.
4) Twinning during loading and detwinning during unloading were quantitatively analyzed. Twin propagation velocity was inconsistent as multiple twins unequally

accommodated local strain, but a maximum velocity of 30 mm/s was recorded. Detwinning resulted in a visible Bauschinger-like effect when unloading from more than 11 MPa. A twin was found to have shortened by 18.0% and thinned by 21.6% when unloading from 11.3 MPa. Most of the detwinning occurred after 6 MPa of unloading. In addition to the lack of visible detwinning in earlier loading steps, this suggests that more detwinning will occur when unloading from larger stresses. This may also contribute to the formation of secondary tension twins.

5) Intrusion-like structures resulting from Type I co-zone twin-twin interactions was expanded on. The formation process of a deep, penetrating structure was enlightened by *in situ* observation. Commonly observed TTB_I and TTB_A are formed, while TTB_O does not form. Instead, a series of energetically favorable deposition of twinning dislocations occurs, resulting in the appearance of the barrier twin growing along the impinging twin boundary. When combined with TTB_A's growth by zipping, the appearance of a deep penetration twin-twin structure is observed.
6) A penetration-like structure resulting from a Type II(a) interaction is also observed. This structure is a result of secondary development as opposed to the formation process, unlike the Type I structure. The initial formation of the Type II(a) interaction was consistent with reports in literature, where TTB_I and TTB_O are formed. Further development on the acute angle side revealed the barrier twin growing just away from the interaction point, resulting in the barrier twin curling along the impinging twin boundary. Not to be misconstrued, TTB_A does not form, but instead there is an immeasurably small space between the two twin boundaries. On the obtuse angle side,

the curvature of the barrier twin boundary some distance from TTB_O nucleates additional twins of the same variant, which coalesce and thicken further along the I-CTB_5.

7) The Type II(b) interaction can have two forms. The impinging form locks the tip of the impinging twin at the barrier twin boundary. No TTBs are formed, and the impinging twin is forced to grow away from the interaction. This causes the impinging twin to have highly incoherent boundaries near the interaction. The second form is the apparent-crossing structure, which can be partial or complete. When the approaching twin initiates contact with the impacted twin, TTB_O is formed. TTB_O can continue to expand by the nucleation of new twin bands of the impacted twin variant.

5 Compression-Tension Loading Sequence and Free-End Torsion of Polycrystalline Pure Magnesium

Under axial loading, twinning can significantly change the texture of wrought magnesium alloys and will consequently affect the deformation and fracture of the material. Twinning from monotonic loading [58,97,122,170–177], cyclic loading [27,68,73,88,164,178–181], and loading path changes [59,81,87,182,183] allows for the activation secondary deformation systems, such as basal $\langle a \rangle$ slip or secondary twinning. Therefore, altering the initial texture through pre-deformation could optimize the mechanical properties of magnesium alloys. For example, tension-compression asymmetry of as-wrought magnesium alloys may be reduced through the mitigation of initial basal texture by pre-twinning [89,184].

Pre-deformation experiments can be classified into two categories, the first being two-step monotonic compression experiments along different directions [89,184–190]. Twins are introduced through an initial pre-compression loading along the extrusion direction or rolled direction. A second compression loading is applied, either along the same direction for tension-compression asymmetry study or in an orthotropic direction [89,186,188]. Both result in an increase in the compressive yield strength, where same direction re-compression strengthens due to the texture change and decreased twinning capacity [89] while orthotropic re-compression strengthens due to the increased resistance to detwinning [186]. Microstructurally, orthotropic re-compression results in detwinning and tension-tension double twins [89,185,186,190], which were attributed to the observed enhancement

of ultimate strength during re-compression. The second type of pre-deformation experiments involve alternation of the loading direction [62,87,191–193]. Initial loading by tension or compression will induce a desired pre-deformation state. The loading is then switched, such that the opposite loading state is applied. The loading axis is not always the same. This method of pre-deformation provides a practical means of manipulating the twin structure to improve material strengthening and toughening. Song et al. [191] reported that pre-tension parallel to the rolling direction of a rolled magnesium alloy can modify the initial basal texture such that $\langle 10\bar{1}0 \rangle$ poles are concentrated towards to the rolling direction. Follow-up compression along the transverse direction is then aligned along most grains $\langle \bar{1}2\bar{1}0 \rangle$ axes, allowing the nucleation of more tension twin variants. This increase in activated variants promotes nucleation, rather than growth, and twin-twin interactions, enhancing the grain-refinement hardening. Despite the numerous studies on strain path change, only few apply reversed loading along the same loading axis [87,192,193]. No studies have been carried out from large pre-compressive strains (> 8%) nor have there been any studies to comprehensively examine the microstructural evolution in these types of experiments.

Deformation from shear loading in magnesium has been less extensively studied than tension and compression. Monotonic experimental work has been limited to simple shear tests [81,194–197] and free-end torsion [71,198–211] with a heavy emphasis on visco-plastic self consistent (VPSC) modeling [194,197,198,202,204,209,210,212]. As such, the majority of shear-based experimental studies focus almost exclusively on the mechanical shear stress-strain response and texture evolution. From these studies, though, the

significant deformation systems are suggested. In extruded magnesium materials, basal slip, prismatic slip, and tension twinning play significant roles in deformation [204,210], while only basal slip and tension twinning are significant in rolled materials [210]. Second order deformation along the axial direction, known as Swift effect [213], has also been replicated by VPSC. In extruded materials, Swift effect is reflected by axial contraction [198,204,205], while axial extension is observed in rolled materials [71,210]. In magnesium materials, tension twinning has been credited for the Swift effect [71,210]. While the mechanical response and texture evolution have been extensively reported, minimal experimental work has examined the microstructural evolution from pure shear loading [194,195,197,205,211]. Only recently as there been a detailed microstructural analysis done on a rolled magnesium alloy subjected to free-end torsion [71].

5.1 Materials, Mechanical Experiments, and Specimen Preparation

For pre-compression experiments, solid cylindrical dog-bone shaped specimens were machined from an extruded pure polycrystalline magnesium rod. The specimen's gage section had a length of 12.7 mm and a diameter of 10.0 mm. Thick-walled tubular specimens with a 30 mm gage length, 16 mm inner diameter, and 24 mm outer gage diameter (thickness is 4 mm) were machined from the extruded pure polycrystalline magnesium rod for torsion. Both specimen types are visualized in Figure 37a. Initial microstructure revealed by EBSD inverse pole figure (IPF) map (Figure 37b) revealed untwinned and equiaxed grains with an average size of 100 μm. The basal (0001) pole figure (Figure 37c) reveals that most of the scanned grains' c-axes aligned perpendicular to the extruded direction (ED). Prior to mechanical testing, the specimen gage sections

were sequentially polished with silicon carbide grit papers from 320/P400 to 600/P1200. For the thick-walled specimens for torsion, axial and tangential lines were engraved in the gage section for measuring strain.

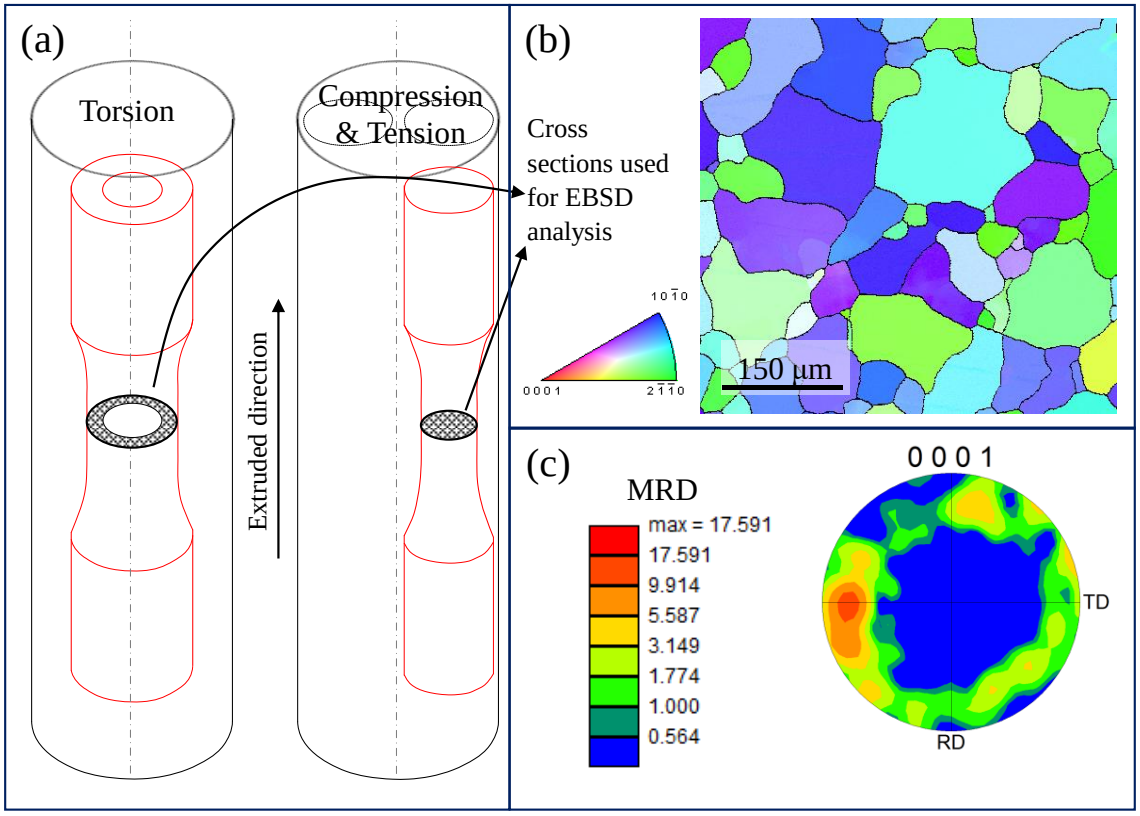

Figure 37: (a) Cylindrical dog-bone shaped pure magnesium specimens as cut from the extruded rod, as well as the (b) initial microstructure and (c) texture of the cross-section [12].

Mechanical experiments were conducted using a servo-hydraulic axial-torsion Instron 8500 load frame in ambient air. The machine has an axial load capacity of ±222 kN and a torsional load capacity of ±2800 Nm. For the axial tension and compression, strain was measured by a clip-on extensometer with a gage length of ½ in. (12.7 mm) and a strain range of ± 40%, and a strain rate of 4.5×10^{-3} s^{-1} was used for both tension and compression

loading. Companion specimens were used capture intermittent strain levels to examine the effect of pre-compression on microstructure evolution. Under pure compression, five companion specimens are taken at true strains of -0.7%, -3.0%, -7.3%, -10.5%, and -12.8% for the study of twin nucleation and growth during monotonic compression. Three companion specimens were used for -7.3% pre-compression, and were taken from true strains of -4.1%, 2.0%, and tensile failure (4.8%) following the reversed tension loading. The three companion specimens for -12.8% pre-compression were unloaded at -9.4%, -2.0%, and tensile failure (4.3%). For the remainder of this chapter, true stress and true strain will be used for the discussion of the pre-compression experiments, results, and analyses.

For free-end torsion, a modified biaxial MTS extensometer with a gage length of 25.4 mm and a shear range of ±3% was used. To avoid damaging the extensometer, it was removed after reaching a strain of ~5%. Following the experiment, residual plastic strains were measured by the dimensional changes in the engraved lines. Residual plastic surface shear strain, γ_p, was measured by the angular change between the axial and tangential engraved lines with respect to the undeformed measurements. The total shear strain, γ, is calculated by equation 1, where the surface shear stress, τ_s, is calculated using equation 2.

$$\gamma = \gamma_p + \frac{\tau_s}{G} \tag{1}$$

$$\tau_s = \frac{3T}{2\pi(r_o^3 - r_i^3)} \tag{2}$$

where G is the shear modulus, T is the measured torque, r_o is the initial outer diameter of the specimen, and r_i is the initial inner diameter of the specimen. Shear strain after the removal of the extensometer is assumed to be a linear relationship between shear strain and

the rotation angle reported by the testing system. Loading was applied by rotation angle control such that the surface shear rate was ~ 3 x 10^{-3} s^{-1}. Companion specimens were taken 5.8%, 11.5%, and 22.1% (failure) plastic surface shear strain.

Following the mechanical experiments, cross-sectional EBSD samples are sectioned from roughly the middle of the gage sections. For fractured specimens, samples were taken some distance from the fracture surface but still within the gage section. For EBSD analysis, the surfaces of the samples were sequentially ground, polished, and then etched using standard metallographic procedures. Grinding and polishing were done using the same procedure reported in Chapter 3.2. Pre-compression samples were etched in a picral-acetic solution for EBSD acquisition (10 mL glacial acetic acid, 4.2 g picric acid, 10 mL water, and 70 mL 200 proof ethanol) by a TSL OIM SEM-EBSD system. Two EBSD scans were conducted on the prepared sectioned samples with areas of 1.2 mm x 1.0 mm using step sizes ranging from 0.35 to 0.6 μm. Torsion samples were etched with ~ 3% (1 mL nitric acid, 30 mL 200 proof ethanol) for EBSD analysis using a JEOL 7100F field emission SEM with an Oxford HKL Channel 5 EBSD package. Scan areas of 1.2 mm x 1.2 mm using a step size of 1.5 μm were used. EBSD scans for the torsion specimens were taken at the midsection of the cross-sectional ring.

5.2 Microstructure and Texture Evolution during Compression-Tension Loading Sequence

To capture the effect of pre-compression, and thus twinning, on the reversed tension response, two pre-strain levels are used. The lower pre-strain level, -7.3%, was chosen to introduce a significant number of twins prior to exhaustion. The larger pre-strain, -12.8%,

was chosen for twin exhaustion before reversing the load direction. The true stress-strain responses for the examined loading paths are shown in Figure 38, where points "A," "B," "C," and "D" correspond to the companion specimen strain levels taken from the tension reversals.

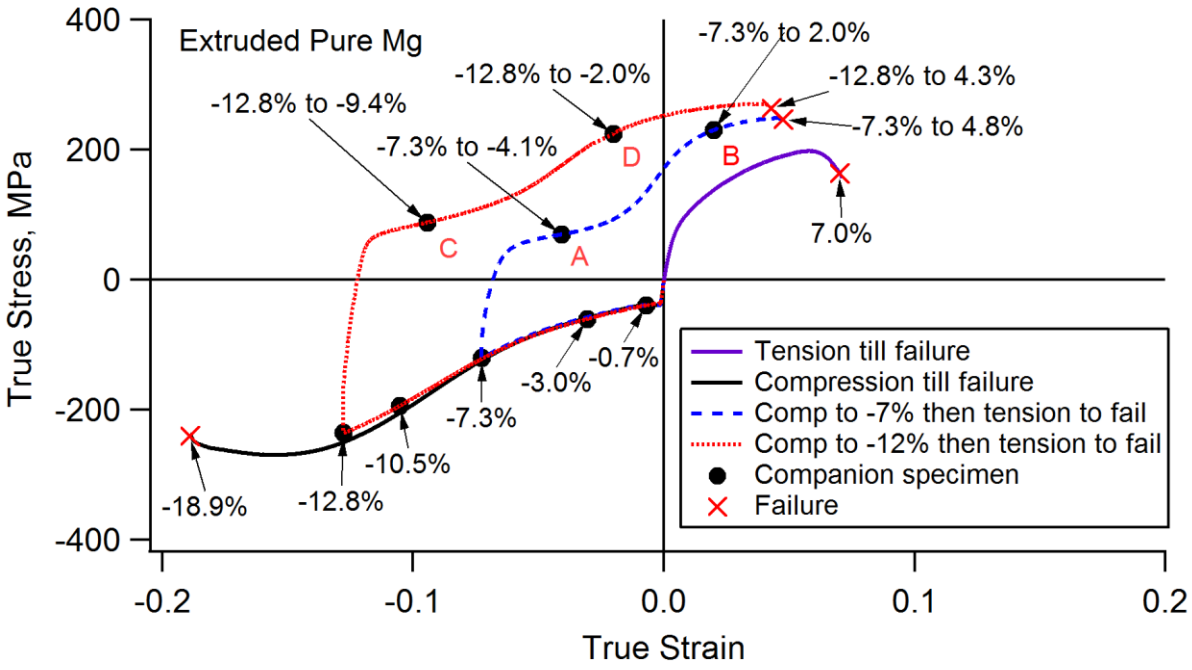

Figure 38: True stress-strain response for the loading cases and corresponding companion specimens, as indicated by markers along the loading curves [12]

5.2.1 Compression Parallel to Extrusion Direction

Compression parallel to the ED of the rod is known to induce twinning. Figure 39 summarizes the microstructural evolution due to twinning up to -12.8% compressive strain where twinning is exhausted at 94.1% twin volume fraction.

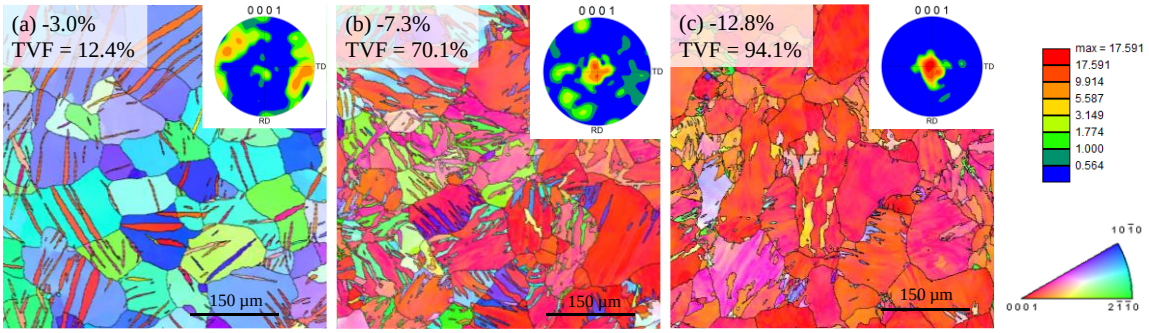

Figure 39: EBSD results for three compression companion specimens taken at (a) -3.0%, (b) -7.3%, and (c) -12.8% true strain.

At -3% compressive strain (Figure 39a), a statistical analysis of 209 grains reveals a twin volume fraction of 12.4%, with 76.6% of grains containing at least one twin variant and 40.7% containing two or more twin variants. Additionally, the twins present are consistent both in shape and activation. As described in Chapter 2.3, the number of variants nucleated depends on the crystal orientation of the grains. Twinning under compression ideally rotates the crystal so that the *c*-axis can be aligned closely with the loading axis. Assuming ideal crystal orientations, compression along the $\langle 10\bar{1}0 \rangle$ direction ("blue" grains in IPF maps) results in one co-zone variant pair with a shared *SF* value of 0.499 and two pairs with a much lower value of 0.1247. Alternatively, compression along the $\langle 1\bar{2}10 \rangle$ direction ("green" grains in IPF maps) results in two pairs with shared *SF* values of 0.374 and the remaining pair with a shared *SF* value of 0. Any orientation between will have three pairs of *SF* values where one pair will have the largest *SF*, another pair will have the smallest *SF*, and the final pair will have a *SF* value between the two extremes. Two grains, one of $\{1\bar{2}10\}$ and another of $\{10\bar{1}0\}$ orientations, are presented in Figure 40.

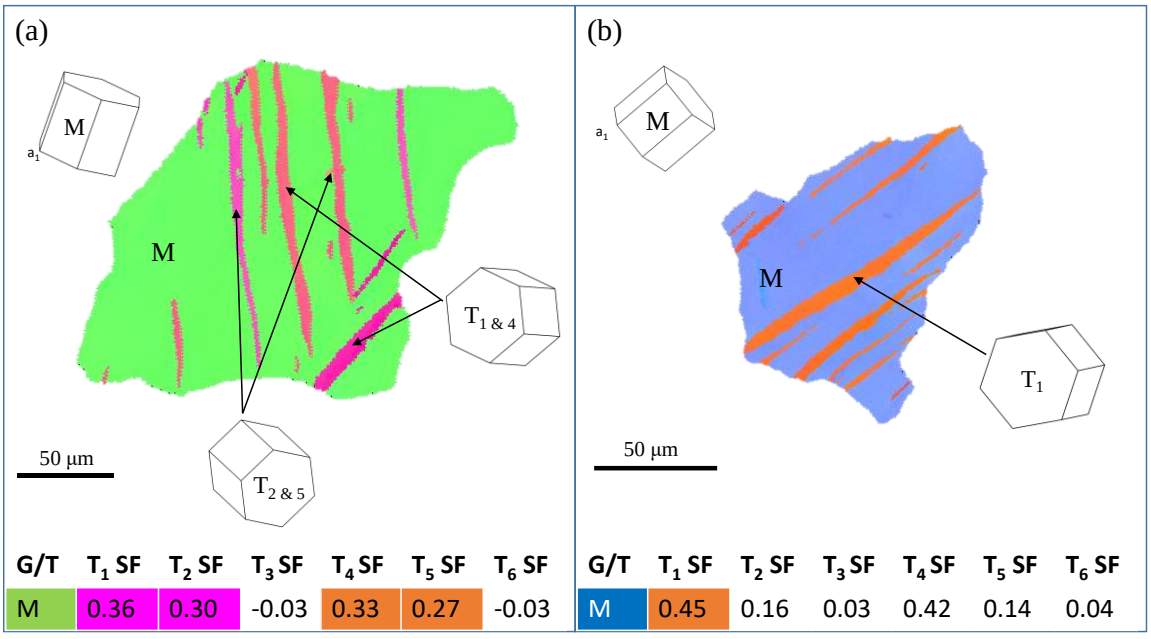

G/T	T_1 SF	T_2 SF	T_3 SF	T_4 SF	T_5 SF	T_6 SF
M	0.36	0.30	-0.03	0.33	0.27	-0.03

G/T	T_1 SF	T_2 SF	T_3 SF	T_4 SF	T_5 SF	T_6 SF
M	0.45	0.16	0.03	0.42	0.14	0.04

Figure 40: Representative grains at -3% compressive strain where (a) four twin variants are favorable and activated and (b) where two variants are favorable but only one variant is activated.

An example "green" $\{1\bar{2}10\}$ grain is highlighted in Figure 40a, where the four almost equally favorable twin variants are identified. At this stage, only a few interactions can be seen, but more are expected as the twins continue to grow with increasing strain. These interactions will limit further growth of some twins and increase the nucleation of additional twins. Alternatively, in the second grain, an example "blue" $\{10\bar{1}0\}$ grain in Figure 40b, two variants are favorably oriented but only one is identified. In similarly oriented grains, only one co-zone pair is expected to form so only Type I interactions may be observed. With increasing strain, these grains are expected to twin more rapidly given the fewer expected interactions.

With increasing strain, the nucleation and growth of new twins result in an increased TVF. Twin boundaries of the same variant meet and coalesce, forming a larger, joined twinned area. The interactions of co-zone pairs also give the appearance of coalescence due to the small misorientation (< 7°) as the EBSD boundary identification algorithms are unable to separate the two variants. As such, at -7.3% strain (Figure 39b), the twin volume fraction increases to 70.1% and the texture is clearly evolving such that the (0001) poles are aligning with the extruded direction. When examining the microstructural evolution closer, the expectations derived from the -3% compressive strain are realized by -7.3% strain. Two grains of almost the two ideal orientations are highlighted in Figure 41 that shows the development of twinning. In the "green" grain of Figure 41a, the four favored variants are identified. Parallel twins of the same variant coalesce and appear as a thicker individual twin. It is also noted that some twins grow from the boundary of others, as observed in the upper right corner of the highlighted grain, where T_1 grows from the end of a T_5 band. Additionally, twin-twin interactions hinder twin development in the grains containing multiple variants. In other "green" grains, fewer variants may activated, allowing for an increased degree of twinning. As a result, the "green" grains show a variable amount of twinning, especially when compared to "blue" grains that are more severely twinned. "Blue" grains are primarily twinned by one variant or by one co-zone pair. The specific grain highlighted in Figure 41b is twinned by only one variant allowing for easy nucleation, growth, and coalescence of multiple twin bands. This allows for the grain to be more rapidly twinned than the "green" grains containing multiple variants.

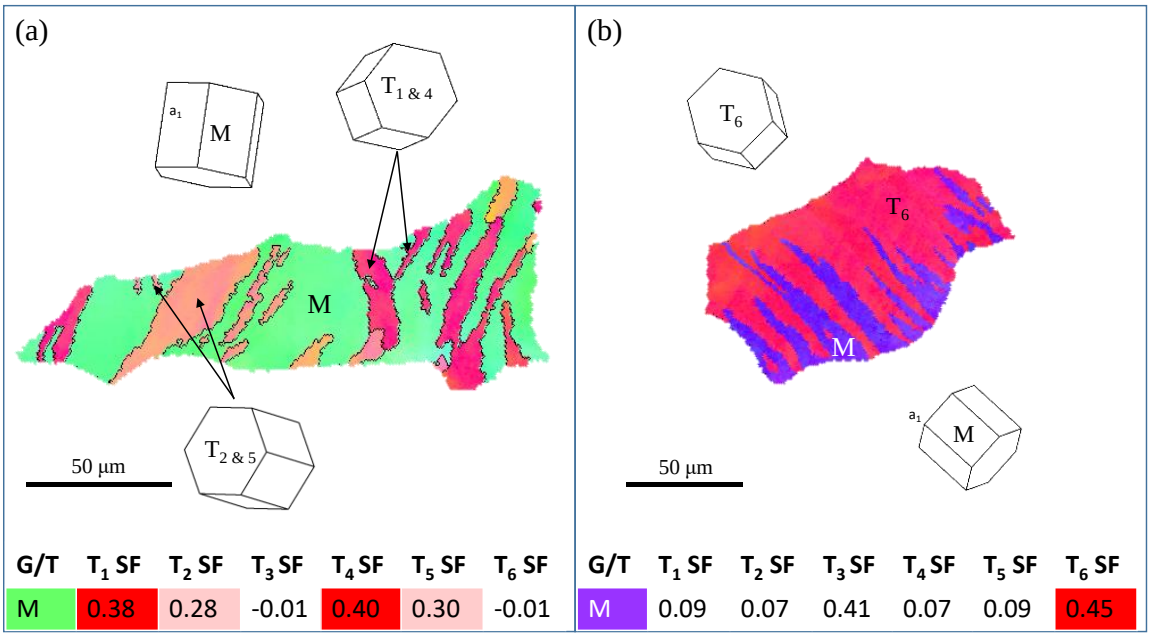

G/T	T_1 SF	T_2 SF	T_3 SF	T_4 SF	T_5 SF	T_6 SF
M	0.38	0.28	-0.01	0.40	0.30	-0.01

G/T	T_1 SF	T_2 SF	T_3 SF	T_4 SF	T_5 SF	T_6 SF
M	0.09	0.07	0.41	0.07	0.09	0.45

Figure 41: Representative grains at -7.3% compressive strain where (a) four twin variants are favorable and activated and (b) where two variants are favorable but only one variant is activated.

By -12.8% strain (Figure 39c), twinning is exhausted and the TVF increases to 94.1%. Based on the texture evolution, twins favoring a rotation of the c-axes towards the ED are favorable. Twins from originally prismatic "blue" grains are going to have their c-axes closely align with the ED. Twins originating from the *a*-axis "green" grains will be misaligned with the ED by ~ 30°. This is represented by the strong basal texture in the {0001} pole figure of Figure 39c, where the *c*-axes of most grains are now nearly aligned with the extrusion direction. More importantly, grains of both ideal orientations can be completely, or near completely, twinned. In a "green" grain, like that shown in Figure 42a, is still primarily twinned by four favorable twin variants. This grain also contains isolated "island" twins that operate as sub-grains resulting from co-zone variant pairs surrounding

a different twin variant. These sub-grain twins originate as the twins that nucleate and grow from other twin boundaries, as previously noted from the “green” grain in Figure 41a, and are halted at other barrier twins. As the strain increased, the nucleation, growth, and coalescence of the surrounding co-zone variant pair will encompass the isolated twin. It is also noted that the sub-grains formed in this manner tend to deviate from the often-found lenticular shape of tension twinning, instead appearing curved or wavy. More severe examples can be observed in Figure 39c, like the yellow twin variants being surrounded by red twin variants in the middle of the scan. These strong deviations are attributed to twin-twin interactions and the twin-twin boundaries that deviate from the coherent twin planes. Despite the multiple interactions that occur, the grain is still nearly completely twinned, as are the “blue” grains such the as the one highlighted in Figure 42b. As with lower strains, twinning in the nearly prismatic “blue” grains are dominated by the two highly favorable variants. In both grains, very small non-*SF* twins can be observed in the grains that are almost completely twinned. At the higher strain, the significant build-up of dislocations at the grain boundary increases the local stresses, thus allowing for the nucleation of non-favorable twin variants [61,214,215].

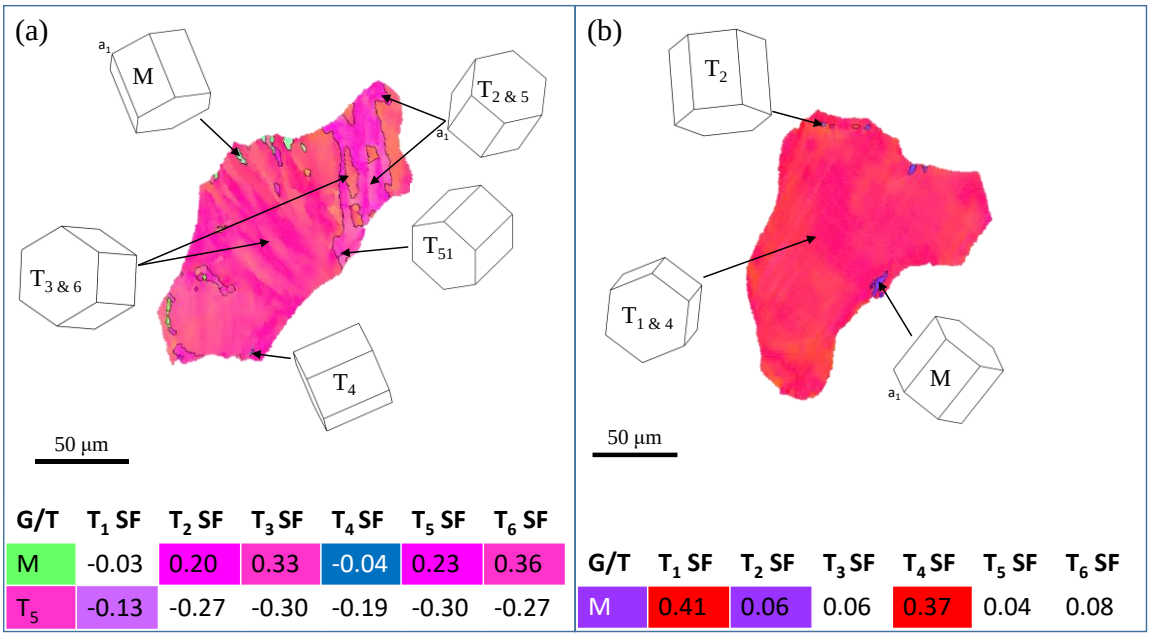

G/T	T_1 SF	T_2 SF	T_3 SF	T_4 SF	T_5 SF	T_6 SF
M	-0.03	0.20	0.33	-0.04	0.23	0.36
T_5	-0.13	-0.27	-0.30	-0.19	-0.30	-0.27

G/T	T_1 SF	T_2 SF	T_3 SF	T_4 SF	T_5 SF	T_6 SF
M	0.41	0.06	0.06	0.37	0.04	0.08

Figure 42: Representative grains at -12.8% compressive strain where (a) twinning is dominated by four favorable variants and (b) where twinning is dominated by two variants.

5.2.2 Tension to Failure Following Pre-Compression

Tension after -7.3% pre-compression strain results in both detwinning and secondary twinning. Two strain states are analyzed in Figure 43 corresponding to 3.2% and 12.1% tension strain applied following the pre-compression. At -4.1% strain, evidence of both detwinning and tension secondary twinning are observed. In the highlighted/circled grain (Figure 43c), three orientations are observed and designated as parent, primary tension twin, and secondary tension twin. The larger blue area is identified as the parent and easily twins to T_1 (the red variant) under the pre-compression load with a large *SF* of 0.498. The second, smaller blue area within the primary red twin is identified as the T_{16} secondary tension twin and is likely formed under tension based on its 0.492 *SF* value.

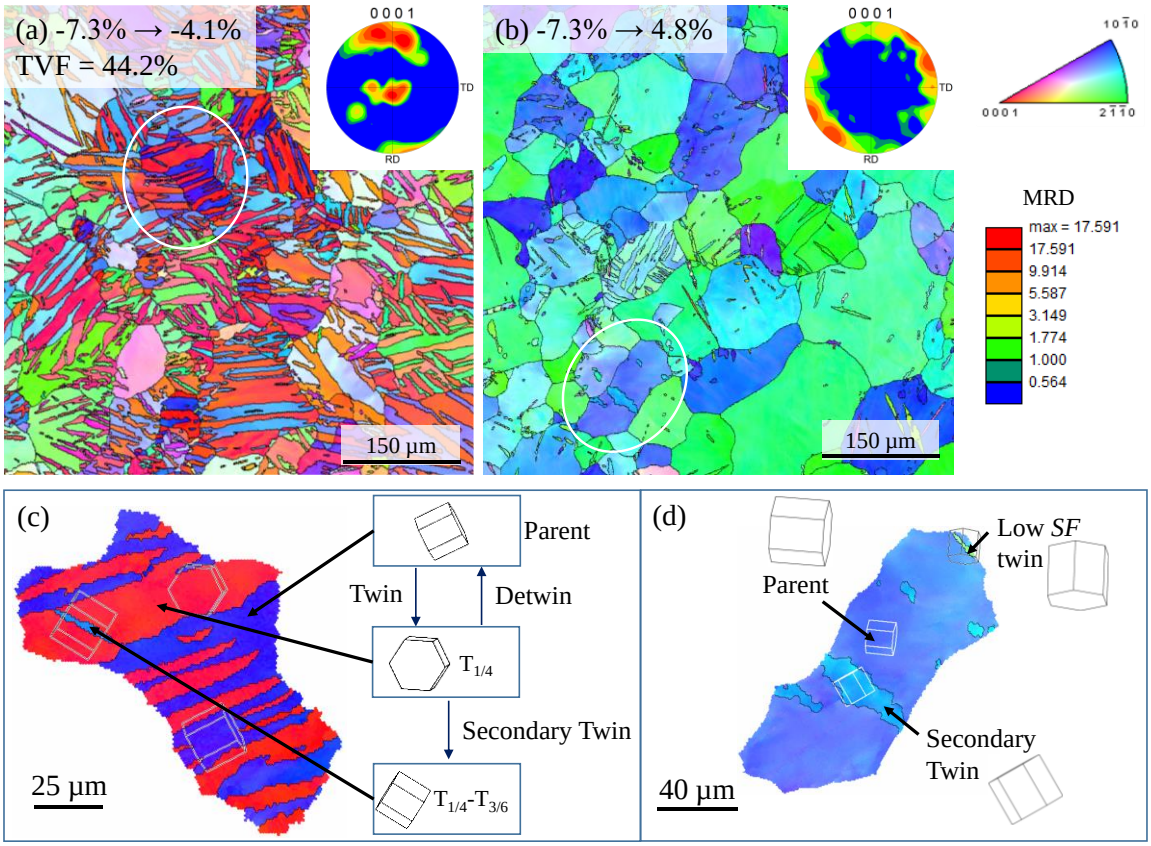

Figure 43: Inverse pole figure maps and (0001) pole figures for the results of tension from -7.3% strain after (a) 3.2% tension and (b) tension failure and (c,d) their corresponding representative grains [12]

Further applying tension until failure reveals that most grains are fully detwinned but contain twin-like sub-grains. Crystallographic analysis reveals that the bulk of the sub-grains are secondary tension twins based on a ~60° misorientation about the $\langle 10\bar{1}0 \rangle$ axis relative to the assumed parent orientation. This misorientation relationship is identical to that for non-co-zone twins, so treating the detwinned parent as its secondary twin equivalent and comparing it to T_{16} may assist in visualizing the relationship. In addition to these embedded secondary twins in the parent, low *SF* primary twins are also observed. Like with the non-*SF* twins observed in compression, these unfavorable twins are also

attributed to local stress effects caused by the build-up of dislocations at the grain boundary. Texturally, both the secondary twinning and low *SF* twinning can be misleading by suggesting that the material has strictly undergone detwinning. Microstructurally, both types of twinning result in an effect similar to grain refinement through the formation of sub-grain structures.

Tension following -12.8% pre-compression results in similar behavior but with minor differences compared to -7.3% pre-compression. Detailed microstructural analysis of the -12.8% to -9.4% companion specimen reveals less detwinning and significantly more secondary twinning compared to the -7.3% counterpart. One example is the grain shown in Figure 44c, where multiple secondary twins are observed within a heavily twinned grain. Compression of the speculated parent orientation results in three primary twins, T_1, T_2, and T_4 with T_2 being the dominant variant based on TVF. This is supported with T_2 having a large *SF* of 0.463 while T_1 and T_4 have lower *SF* values of 0.201 and 0.187, respectively. Because of the highly favorable orientation of T_2 for twinning under tension, three secondary twins are formed: T_{21}, T_{25}, and T_{26}. Additionally, T_{25} is the co-zone pair to the parent, which is the result of detwinning and can correspondingly be labeled as T_{22}. Based on crystallography, either T_{22} or T_{25} could be the parent orientation but for the analysis, both areas would yield the same microstructural analysis. Treating the detwinned area as a T_{22} secondary twin, the four *SF* values for these secondary twins are 0.446, 0.424, 0.399, and 0.431, respectively. At tensile failure, the effect of secondary twinning results in substantially more sub-grains within the detwinned grains. In terms of texture, the

additional secondary twin variants result in a more randomized *a*-axis texture compared to the lower pre-compression.

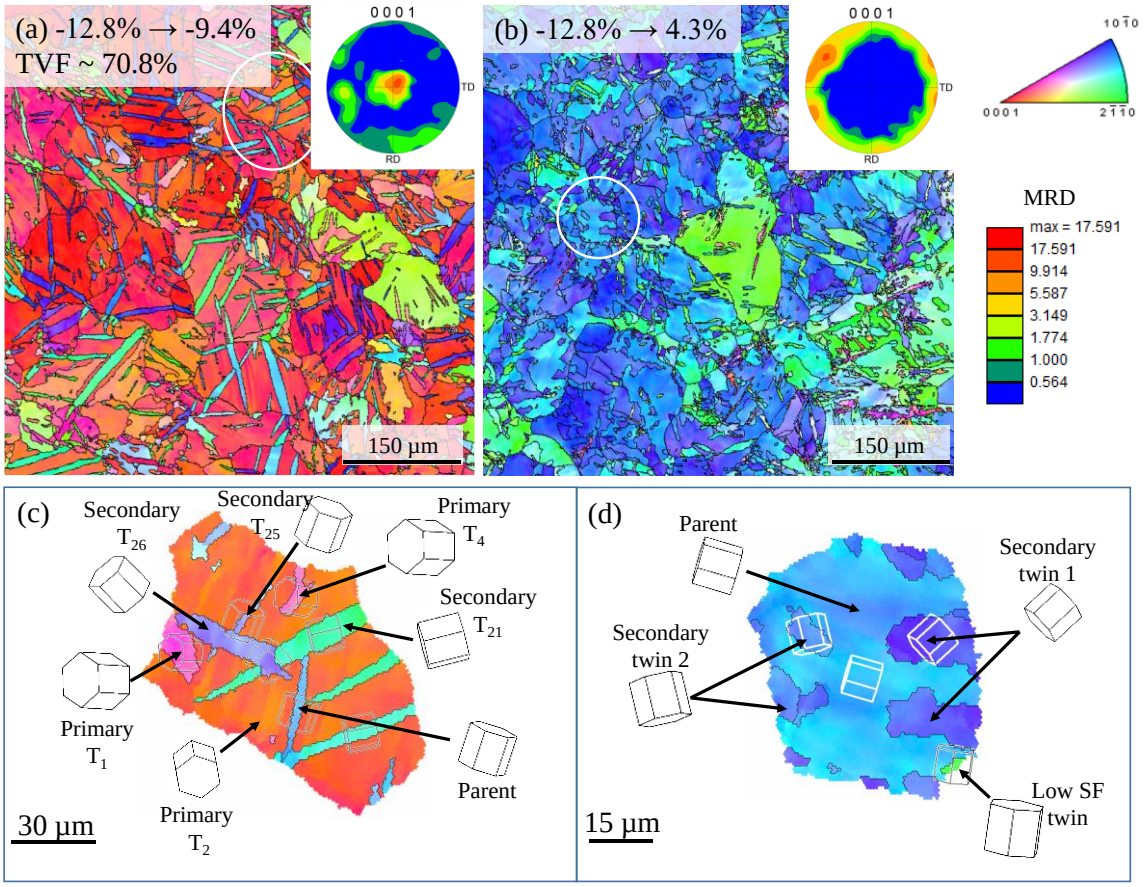

Figure 44: Inverse pole figure maps and (0001) pole figures for the results of tension from -12.8% strain after (a) 3.4% tension and (b) tension failure with (c,d) their corresponding representative grains [12]

The increased secondary twinning during the tension reversal has an additional effect in a small number of grains. Small non-*SF* twins are identified in some secondary twins forming tension-tension-tension tertiary twins. Two such cases are crystallographically identified and presented in Figure 45. During compression, the presumed matrix is highly favorable to twin by one co-zone pair, T_1 and/or T_4, yielding a unit cell crystallographically

similar to the highlighted red twin from a neighboring grain. The grain is fully twinned by -12.8% strain, so when the loading is reversed, secondary twinning will occur where all six variants, including the detwinning variant, are favorable. Four secondary variants, not including the assumed detwinning variant, can be identified, including the two "blue" secondary twins in which the tertiary twins are found. However, as with primary twinning under uniaxial monotonic loading, these twinned regions are unfavorably oriented for additional twinning. Yet, as with non-*SF* twinning in those cases, the build-up of dislocations at the boundaries can alter the local stresses for the unfavorable tertiary tension twins to nucleate.

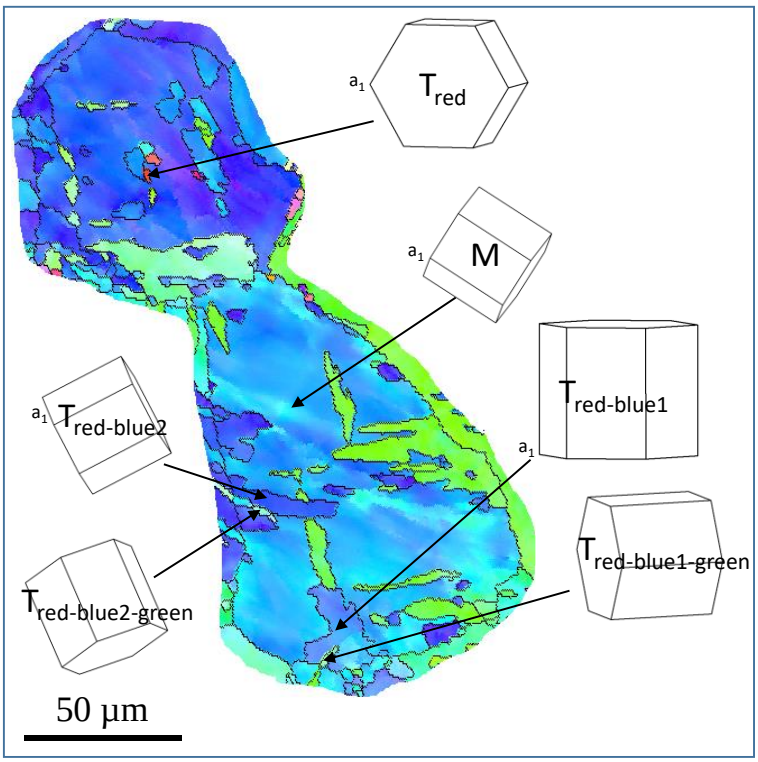

Figure 45: Tension-tension-tension tertiary twins identified after tensile failure after -12.8% pre-compressive strain.

5.2.3 Further Discussions and Analysis

A thorough crystallographic analysis reveals that detwinning is significantly affected by two factors: the extent of twinning and the number of primary twins activated resulting from pre-compression. First accounting for the extent of twinning, most grains are not completely twinned by -7.3% pre-strain whereas twinning is exhausted with -12.8% pre-strain. In the same way twin nucleation requires more stress than twin propagation and thickening, detwinning is easier to activate when the grain is not fully twinned [81]. An exhausted primary twin will behave as a new or reoriented grain, so detwinning of an exhausted twin is analogous to the nucleation and propagation of a secondary twin having the parent orientation. Thus, detwinning is easier to activate in grains subjected to -7.3% pre-strain while being more difficult to activate in grains subjected to -12.8% pre-strain.

In grains containing more than one twin variant, detwinning can become further complicated due to twin-twin interactions [214]. To detwin interacting twins, the process of interaction must be reversed. The twin-twin boundary dislocations must dissociate into twinning dislocations for the twin thickness to decrease. Based on the dislocation theory, though, dissociation is energetically unfavorable [214]. Contrary to the argument against detwinning, both pre-strain paths appear fully or nearly fully detwinned by tensile failure based on their respective inverse pole figure maps. The two possible explanations are that the local stress state allowed for detwinning to continue or that additional secondary twinning results in a similar microstructure to that by detwinning.

These factors also contribute to the tension-tension secondary twinning behavior. Fewer secondary twins are observed along the -7.3% pre-strain path where twinning is

incomplete. In the grain observed after 3.2% tension strain, only one secondary twin is observed within the primary twin despite its favorability for all six variants. Alternatively, three secondary twin variants, or four if the detwinning area is considered, are identified within the grain from the -12.8% pre-strain path after a similar tension re-load is applied. Furthermore, multiple twin-twin boundaries are formed as a result of these secondary twins, further afflicting the detwinning process. At tension failure, the difference is even more significant. From -7.3%, most grains contain only a few residual primary and/or secondary twins as sub-grains. Alternatively, every grain within the observed area taken from the -12.8% pre-strain path contain these sub-grains.

Based on the observations to this point, the process of twinning under compression followed by detwinning and secondary twinning under tension is proposed in Figure 46. Under compression (Figure 46a), primary twins (designated “T”) with large *SF*s nucleate, grow, and coalesce in a parent grain (designated “M”). If these twins are not of the same variant or co-zone pair, low angle twin-twin boundaries may form upon interaction. The loading direction is reversed to tension (Figure 46b), resulting in both detwinning of the primary twins and secondary tension twinning within the primary twins (designated “T-T”). However, due to both mechanisms occurring simultaneously, the growth of the secondary twins is limited as the primary twin shrinks from detwinning. The conflict between these mechanisms results in the irregular shaped secondary twins and sub-grains. By tensile failure (Figure 46c), the primary twins are significantly detwinned, leaving the tension-tension secondary twins as sub-grains either isolated within the parent grain or at

a grain boundary. The sub-grains affect the local stress state, which can result in low *SF* twins at large tensile strain.

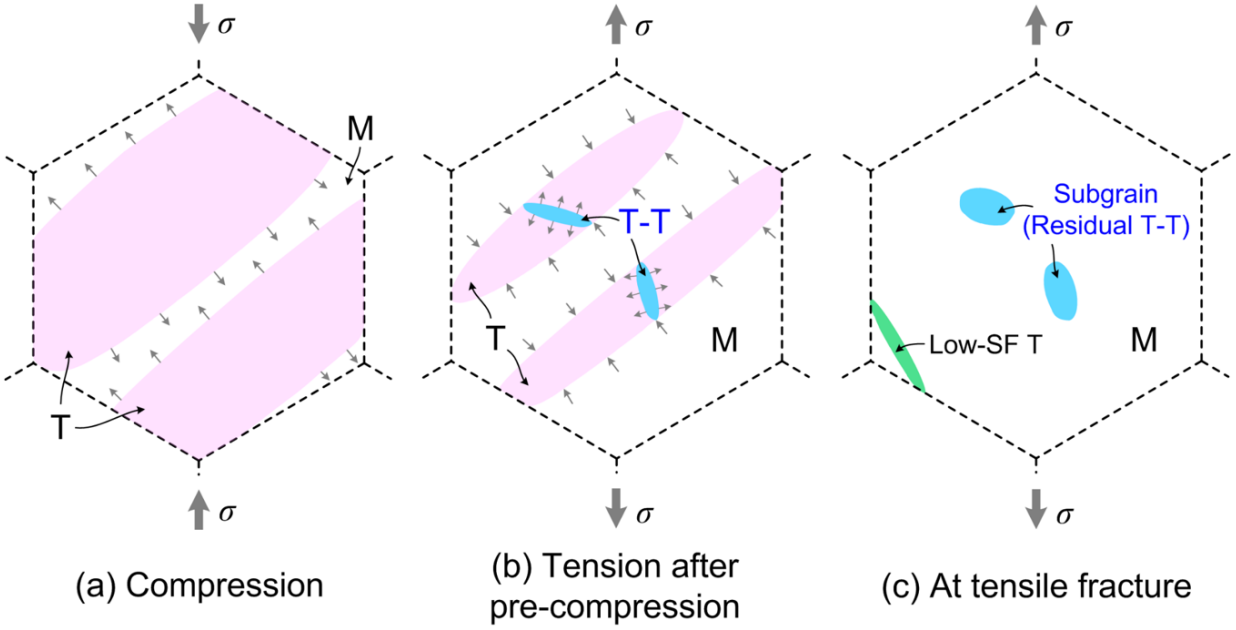

Figure 46: Schematic demonstrating the formation of sub-grains due to simultaneous detwinning and secondary twinning during the tensile loading after pre-compression [12]

Microstructurally and texturally, the effect of twinning, detwinning, and secondary twinning resulting from pre-strain have been examined thus far. Mechanically, the formation of the sub-grains may play a critical role in strengthening magnesium-based materials. In most traditional materials, grain refinement results in an overall strengthening of the material, and thus it may be hypothesized that the formation of sub-grains may also contribute to strengthening [97]. To confirm this, Figure 47 shows the microstructure as a result of tensile failure from 0% (no pre-strain), -7.3%, and -12.8% pre-strain, respectively. Monotonic tension reveals only non-*SF* twinning which occurs to a much larger degree

than the pre-strained microstructures but lacks the sub-grains formed from secondary twinning.

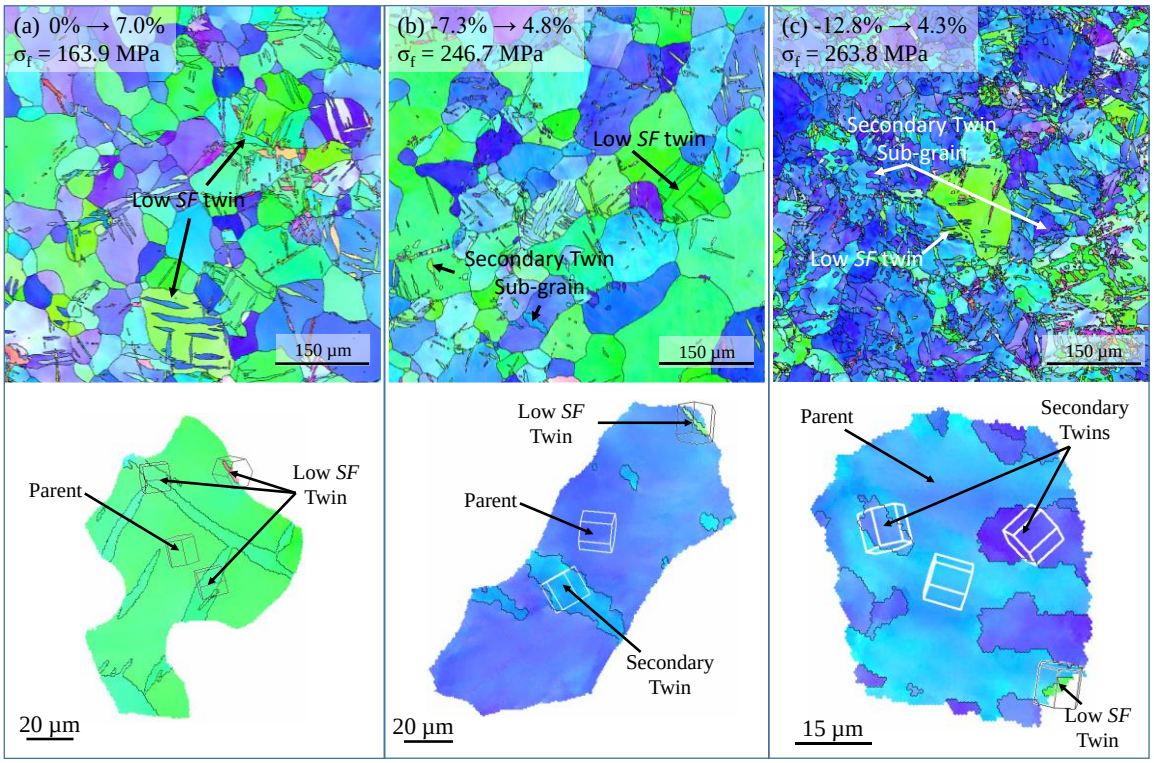

Figure 47: Inverse pole figure maps with highlighted grains for (a) pure monotonic tension failure, (b) tension failure from -7.3% strain, and (c) tension failure from -12.8% strain [12]

In the pre-strained specimens, the observations previously made conclude that the quantity of sub-grains is proportional to the amount of compressive pre-strain. The significant increase in fracture strength from 0% to -7.3% and -12.8% pre-strains indicate strengthening, supporting the claim that sub-grain formation by twinning can be analogous to grain refinement.

5.3 Monotonic Free-End Torsion about the Extrusion Direction

Torsion of a similar extruded pure polycrystalline magnesium yields a different mechanical and material response to that by compression or tension. The surface shear stress vs shear strain is given in Figure 48, along with the twin volume fraction (TVF) measured in the companion specimens. It is noted that, even at failure, the twin volume fraction is less than 60% as opposed to 94% from compression (Figure 39c). This is related to the texture and the difference in twin favorable orientations between the loading cases.

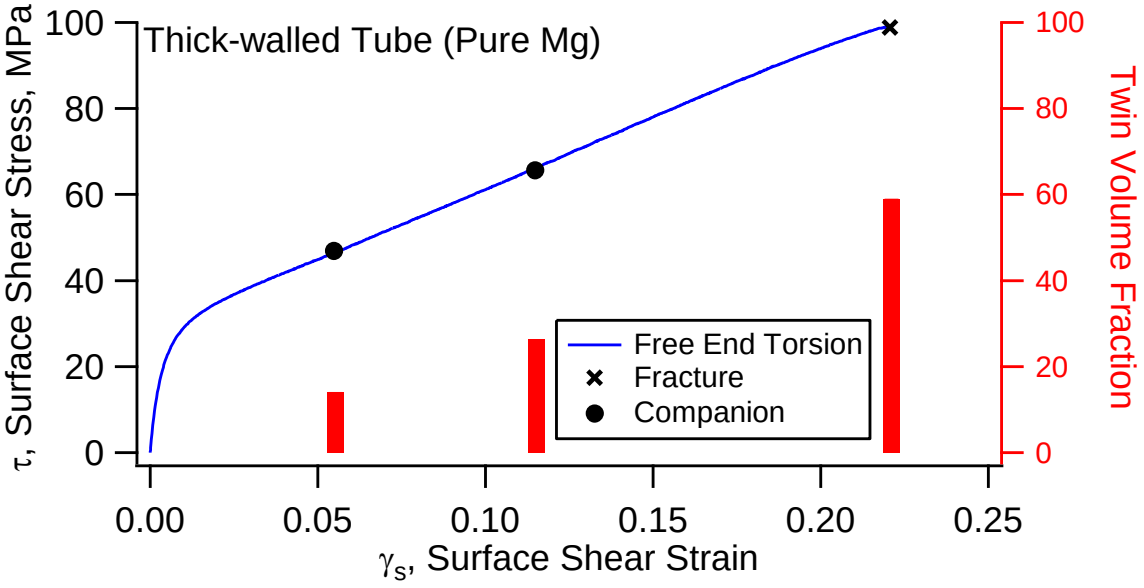

Figure 48: Free-end torsion surface shear stress-strain response

5.3.1 Tension Twin Favorability under Torsion

Under compression parallel to the extrusion direction, or even tension parallel to the normal direction of a rolled material, nearly all of the grains are favorably oriented for twinning. For torsion, it is currently impossible to have nearly all grains be uniformly distributed and be favorable for tension twinning. Figure 49 imposes the theoretical

maximum Schmid factor on a {0001} pole figure for a cross-sectional area. Because the loading is pure shear, it is possible to reach a Schmid factor of 1, where all of the applied shear can be achieved on a given twin system. Superimposing the untested cross-sectional {0001} pole figure from Figure 37b suggests that just more than half of the scanned grains would be considered favorable for twinning.

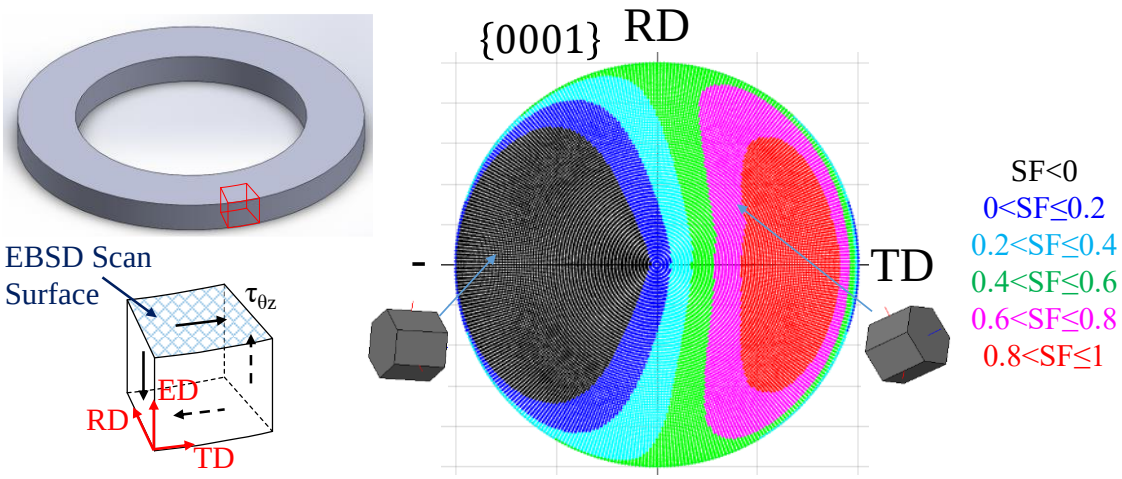

Figure 49: Tension twin maximum Schmid factor pole figure imposed on a {0001} pole figure for torsion. Two unit cells are included showing a twin favorable orientation with a maximum Schmid factor of ~ 0.8 and a unit cell very unfavorable orientation with a maximum Schmid factor of ~ -0.4.

As torsion is a multiaxial loading, traditional Schmid's law cannot be directly applied. There have been several reported methods of calculating an effective Schmid factor in literature [216–218], but a simple mechanics of materials approach is taken here. Two approaches were considered: superposition of two principal stresses and rotating the material stress state. To best visualize twin favorability, two "ideal" crystal orientations for torsion are shown in Figure 50. For discussion, it can be assumed that one principal stress

is tension parallel to the *c*-axis and the second principal stress is compression perpendicular to the *c*-axis. These ideal orientations are the superposition of *c*-axis tension (Figure 6a) with the two ideal crystals with compression perpendicular to the *c*-axis (Figure 6b and 6c). This results in all six tension twin variants being favorable (Schmid factor ≥ 0.499), but two or four variants will be more favorable depending on how the *a*-axis is oriented. Alternatively, the pure shear can be made into a stress tensor and can be rotated to a deformation system using a grain's Euler angles obtained by EBSD. This second method was chosen to calculate the *SF* of any twin variant discussed in this section. The detailed process of this method can be found in Appendix A.

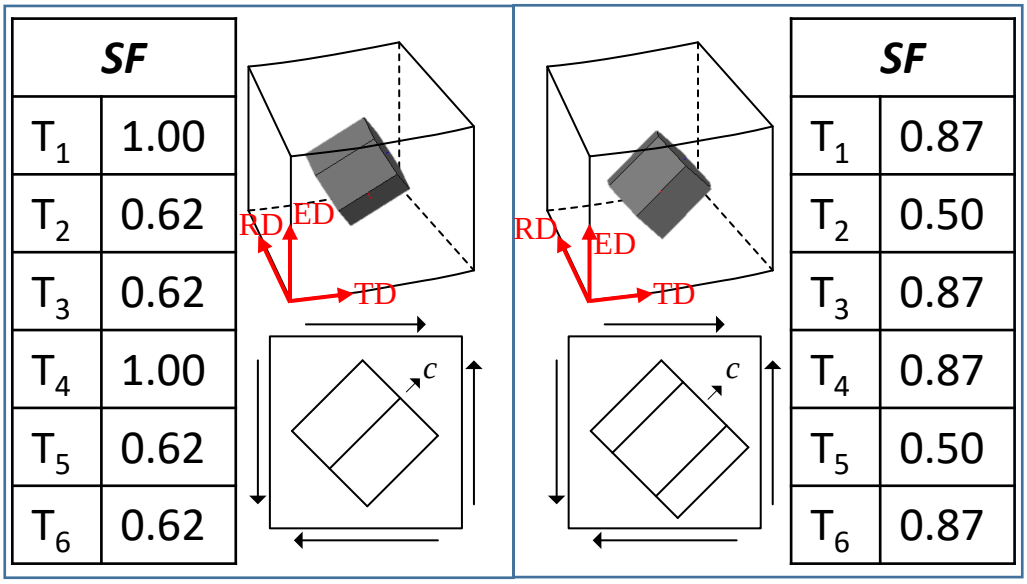

Figure 50: Ideal orientations for torsion where four variants are very favorable with two less favorable variants and four variants are very favorable with two less favorable variants.

5.3.2 Twinning after 5.8% Surface Plastic Shear Strain

Figure 51 shows the microstructure of the companion specimen after 5.8% plastic shear strain on the specimen surface. Numerical analysis of the scan revealed a twin volume

fraction of 14.1%, while more focused examination revealed three degrees of primary twinning based on favorability. These levels vary from severe, highly favorable twinning, to untwinned, with a highly variable middle level.

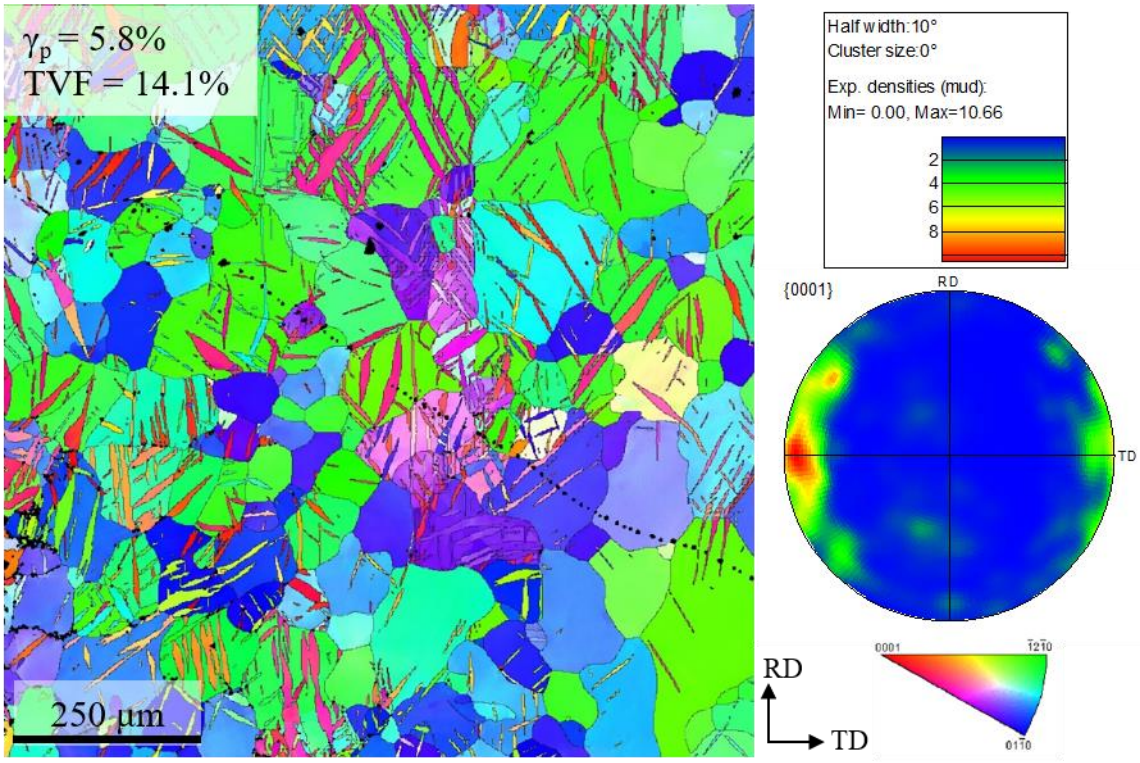

Figure 51: Inverse pole figure map of companion specimen taken at 5.8% plastic shear strain.

As with compression parallel to the extrusion direction, favorably oriented grains undergo significant twinning during torsion. Figure 52 highlights two grains favorably oriented for twinning. In the first grain, Figure 52a, all six variants are activated and are considered favorable to highly favorable. Similarly, the second grain, Figure 52b, is also highly favorable but only four or five variants are identified. T_2 and T_5 are crystallographically similar, but their traces are also very similar, so there is uncertainty in

claiming which twin is activated or if both are present. In both grains, individual variant twin volumes deviate strongly from the expectation. In the first grain, T_3 was the lowest ranked variant yet has the largest twin volume in the grain. Similarly, T_3 and T_6 are the lowest ranked variants in the second grain and encompass the most twin volume in the grain. Alternatively, the highest ranked co-zone pair, especially in the second grain, cover the least amount of twinned area. However, low- or non-*SF* primary twinning, such as T_3 in both grains, result in a more favorable orientation for additional twinning. The activated secondary twins in both grains are considered highly favorable with *SF* values over 0.4, suggesting that Schmid factor may adequately predict possible secondary twinning for torsion.

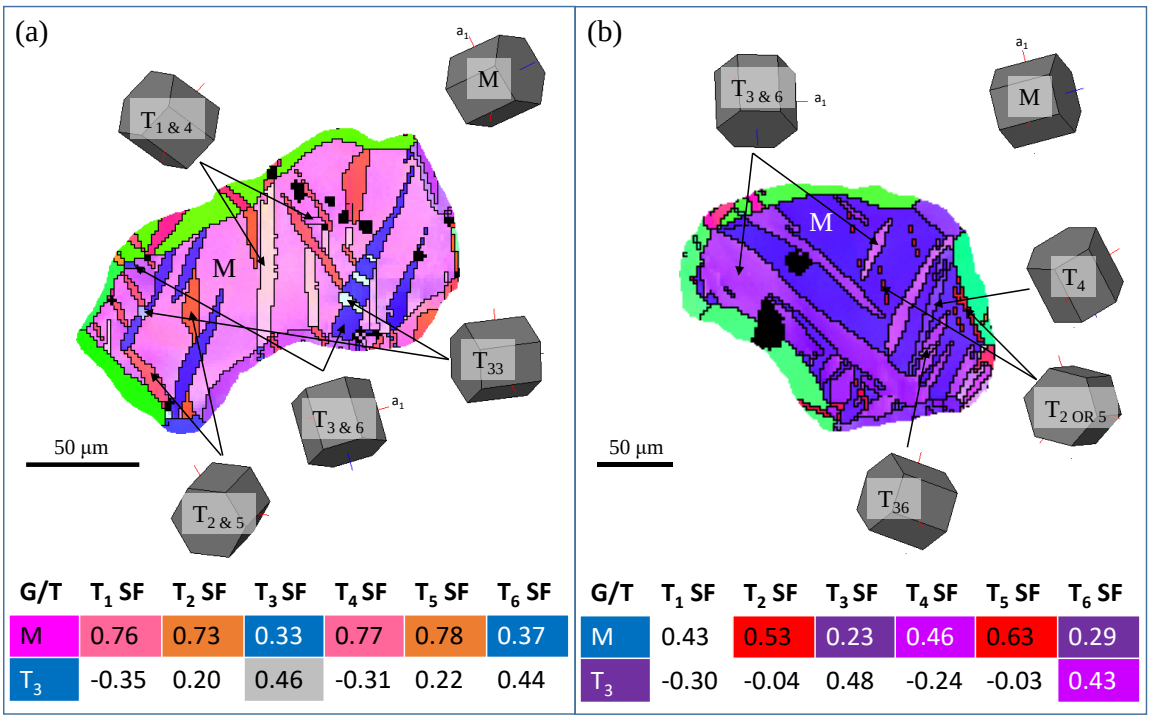

G/T	T_1 SF	T_2 SF	T_3 SF	T_4 SF	T_5 SF	T_6 SF
M	0.76	0.73	0.33	0.77	0.78	0.37
T_3	-0.35	0.20	0.46	-0.31	0.22	0.44

G/T	T_1 SF	T_2 SF	T_3 SF	T_4 SF	T_5 SF	T_6 SF
M	0.43	0.53	0.23	0.46	0.63	0.29
T_3	-0.30	-0.04	0.48	-0.24	-0.03	0.43

Figure 52: Two twin-favorable grains identified at 5.8% plastic shear strain where (a) a grain is twinned by all six tension twin variants and one secondary twin variant and (b) a

grain is twinned by five primary twin variants and a secondary twin variant. Schmid factor tables are color coded for activated variants by inverse pole figure map color. White background in the table indicates that the variant was not activated.

The second level of twinning shows more variability in twin severity. At 5.8% plastic shear strain, grains of this twin level are only moderately twinned compared to the highly favorable grains of Figure 52. As captured by the grains in Figure 53, most of the possible primary twin variants are still activated, despite the Schmid factors ranging from favorable ($SF \sim 0.3$) to unfavorable ($SF \sim -0.2$). This suggests that primary twin prediction by Schmid factor is less accurate in torsion loading, especially in this intermediate favorability range. This can be attributed to the complex stress effects induced at grain boundaries along with the oversimplified assumptions made in calculating the Schmid factor. However, secondary twinning is still adequately predicted by Schmid factor. Two secondary twin variants are identified in the first grain, Figure 53a, with one being unfavorable and the other being highly favorable. In the second grain, only an unfavorable secondary twin variant is identified. The unfavorable variants, T_{22} in (a) and T_{31} in (b), only encompass small areas of their respective primary twins. It is expected that with increasing strain, these secondary twin variants will not grow significantly. Alternatively, the favorable secondary twin, T_{33} or T_{36}, in the first grain almost entirely consumes the small area of its primary twin. As with the challenge in twin identification in Figure 52b, there is not enough evidence to claim which secondary twin is activated. With increasing strain, these types of secondary twins are expected to consume much of their primary twins. However, their low-Schmid factor primary twin volume will limit the overall area consumed by these secondary twins.

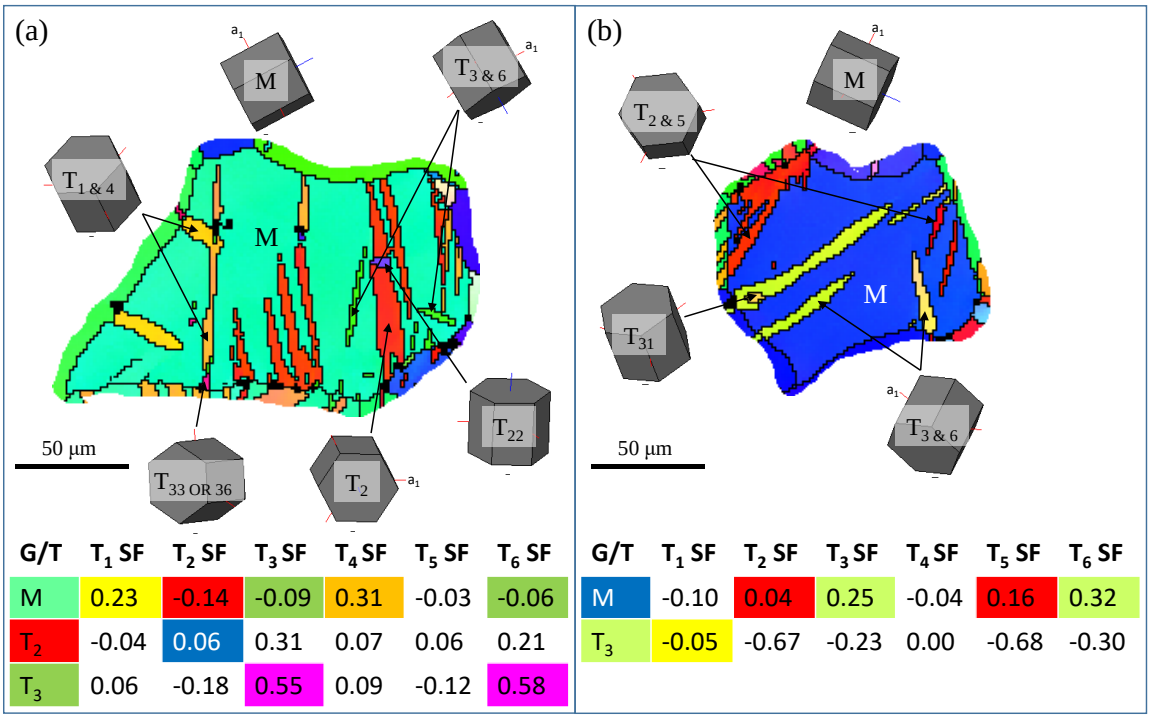

G/T	T_1 SF	T_2 SF	T_3 SF	T_4 SF	T_5 SF	T_6 SF
M	0.23	-0.14	-0.09	0.31	-0.03	-0.06
T_2	-0.04	0.06	0.31	0.07	0.06	0.21
T_3	0.06	-0.18	0.55	0.09	-0.12	0.58

G/T	T_1 SF	T_2 SF	T_3 SF	T_4 SF	T_5 SF	T_6 SF
M	-0.10	0.04	0.25	-0.04	0.16	0.32
T_3	-0.05	-0.67	-0.23	0.00	-0.68	-0.30

Figure 53: Two less twin-favorable grains identified at 5.8% plastic shear strain where (a) a grain is twinned by five primary twin variants and two secondary twin variants and (b) a grain twinned by four primary twin variants and one secondary twin variant. Schmid factor tables are color coded for activated variants by inverse pole figure map color. White background in the table indicates that the variant was not activated.

The third twin level corresponds to the highly unfavorable twins with all negative Schmid factors. The twin severity of this level ranges from completely untwinned to partially twinned grains. Figure 54a highlights an almost untwinned grain. Only small T_6 twin bands are observed, where the larger band is initiated from a cross-grain pair formation at the grain boundary. Applying a similar analysis as what was performed in Chapter 3, *m'* for this cross-grain pair is only 0.3, suggesting that both twins, which are individually unfavorable, form by isolated nucleation [132]. Thus, it is unlikely that one twin has a significant influence on the nucleation and growth of the other. In the second

grain, Figure 54b, four unfavorable primary twin variants are identified. This is significantly different from the non-*SF* twinning highlighted in the tension along the extrusion direction (Figure 47a), where only one or two non-*SF* twin variants are seen in a grain at failure. However, compared to the twins of the first two twin levels and to the non-*SF* twins from extrusion direction tension, the twins in this grain are much thinner. As a result, small twin sections often appear to be isolated within the grain by EBSD, as the narrow sections cannot be resolved by EBSD at this scale. In this grain, T_3 and T_6 bands are such examples, showing gaps within its own twin bands.

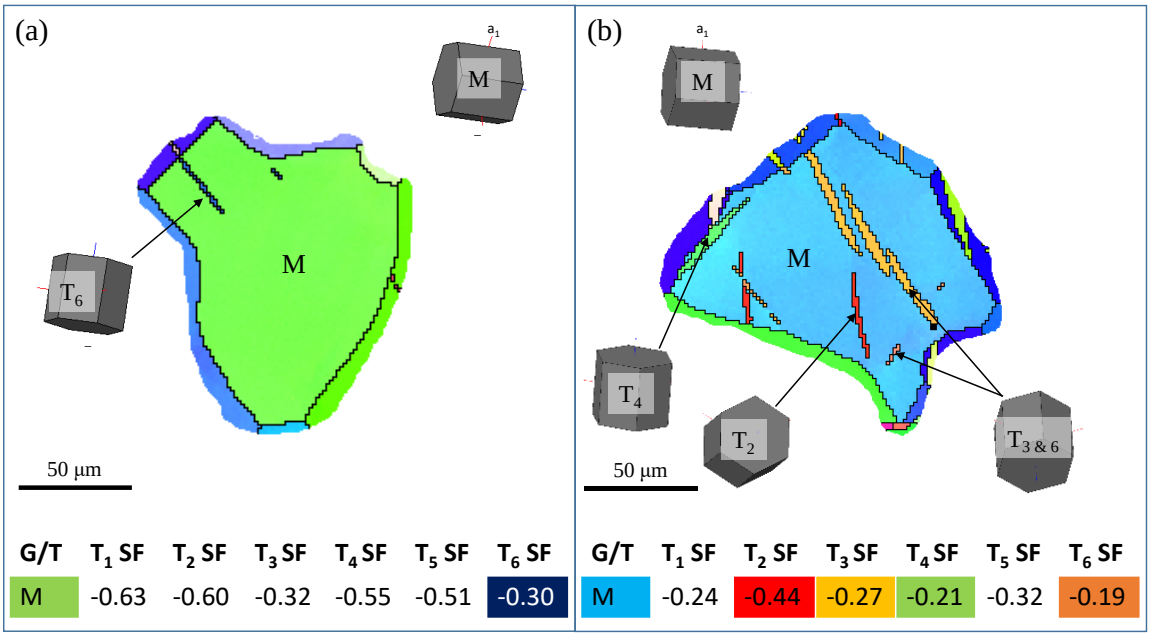

G/T	T_1 SF	T_2 SF	T_3 SF	T_4 SF	T_5 SF	T_6 SF
M	-0.63	-0.60	-0.32	-0.55	-0.51	-0.30

G/T	T_1 SF	T_2 SF	T_3 SF	T_4 SF	T_5 SF	T_6 SF
M	-0.24	-0.44	-0.27	-0.21	-0.32	-0.19

Figure 54: Two twin-unfavorable grains identified at 5.8% plastic shear strain where (a) a grain is twinned by one twin variant activated by twin propagation-assisted adjoining twin pair formation and (b) a grain twinned by four unfavorable primary twin variants. Schmid factor tables are color coded for activated variants by inverse pole figure map color. White background in the table indicates that the variant was not activated.

In addition to the few isolated cross-grain twin pairs, several twin chains and adjoining twin pairs can also be observed from the larger scan. In Chapter 3, ATP formation from tension suggested that both large Schmid factor (>0.37) and high geometric compatibility ($m' > 0.8$) were desirable, while the rank of individual twins is less significant. Figure 55 highlights a propagation-assisted twin chain spanning four grains formed by torsion. The *c*-axis misorientation from grain to grain is very small, however, the Schmid factors of each activated twin varies greatly. In M_1, the *SF* for T_5 is quite large at 0.46 and has a high compatibility with T_4 in M_2 ($m' = 0.90$). T_4 is the highest rank in M_2, but only has a *SF* of 0.05. Favorability continues to decrease in M_3, where the activated T_5 is ranked third and has a -0.26 *SF*. However, geometric compatibility between T_4 in M_2 and T_5 in M_3 is high with a value of 0.92. In the fourth grain, M_4, the activated twin, T_5, is even more unfavorable with a *SF* of -0.39 (rank 5). As with from M_2 to M_3, though, the geometric compatibility between the final two grains is the most favorable, with an m' of 0.94. Because of its unfavorability, the twin in the final grain does not grow very far, stopping well before reaching a barrier twin or grain boundary. Because *SF* is not ideal for discussing twin nucleation, confidence in using it for discussion here is low, but large geometric compatibility, m', is consistent in the ATP formations by twin assisted mechanisms.

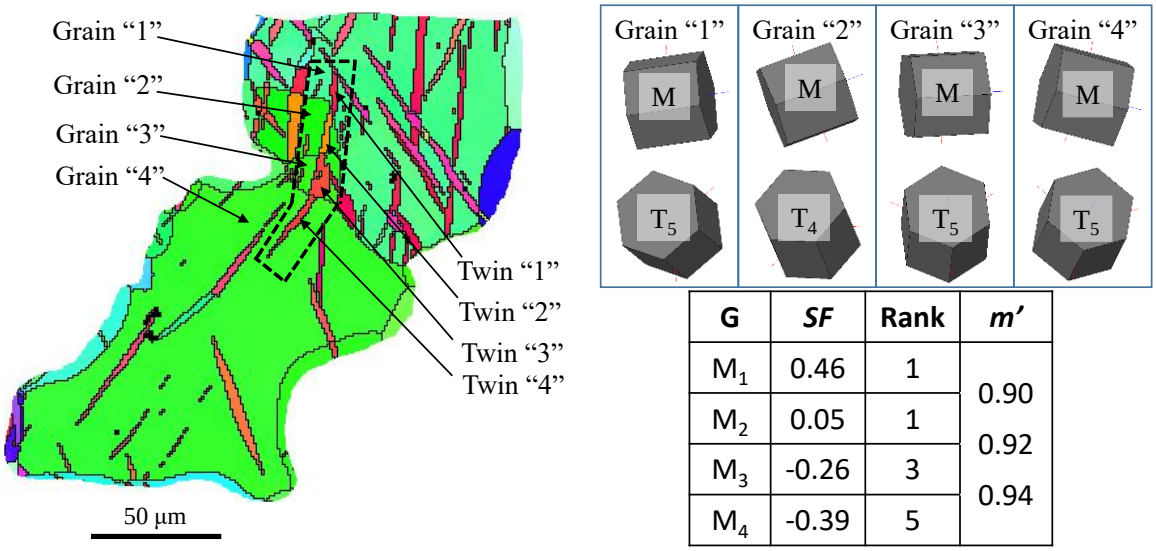

G	*SF*	Rank	*m’*
M_1	0.46	1	0.90
M_2	0.05	1	0.92
M_3	-0.26	3	0.94
M_4	-0.39	5	

Figure 55: Twin chain formation from a favorable grain/twin to progressively less favorable grains/twins

From these observations, several early distinctions can be made between the microstructural response from compression and from torsion. Under compression, twin variants with large *SF* are usually formed and grow significantly, whereas *SF* is a poor indicator of primary twin nucleation under torsion. Additionally, it is difficult to observe more than four activated variants under compression, whereas up to all six variants can be activated under torsion. Additionally, secondary twinning is prevalent in torsion, where low-*SF* primary twins are often favorable oriented for further twinning. With increasing strain, these distinctions become more prevalent.

5.3.3 Twinning after 11.5% Plastic Shear Strain

By 11.5% plastic shear strain, twin volume fraction has increased to 26.4% while maintaining similar trends observed at 5.8% plastic surface strain. The microstructure at

this second strain level is displayed in Figure 56, where the three levels of granular twinning can still be visually identified.

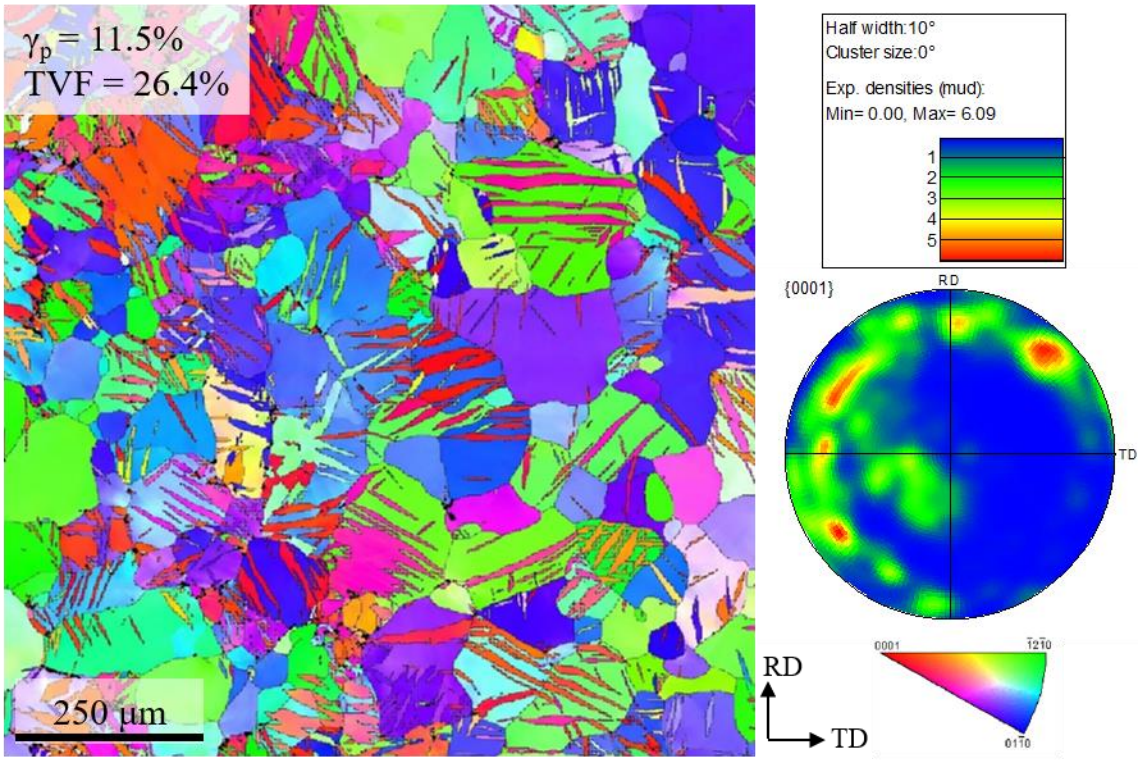

Figure 56: Inverse pole figure map of companion specimen taken at 11.5% plastic shear strain.

After the increase in strain, more variability in twin severity can be noticed in favorably oriented grains. Twinning in the first highlighted grain, Figure 57a, is dominated by a co-zone pair. The most favorable variant pair, T_2 and T_5, although not much more favorable than T_1 and T_4, consume most of the grain. As with compression parallel to the extrusion direction, twinning in this manner exhausts rapidly as the co-zone pair appear continue to nucleate and coalesce new twins. This case differs from compression because all six variants are activated by torsion. However, the four non-dominant variants consume

minimal area. T_6 cannot be visibly identified as its secondary twin T_{63} or T_{66} completely fills its twinned area, but the trace analysis of the secondary twinned area matches the trace of T_6. As with the secondary twins highlighted at the lower strain level, this secondary twin strongly follows Schmid's law where the two possible variants have the highest two ranks with Schmid factor values of 0.598 and 0.546, respectively.

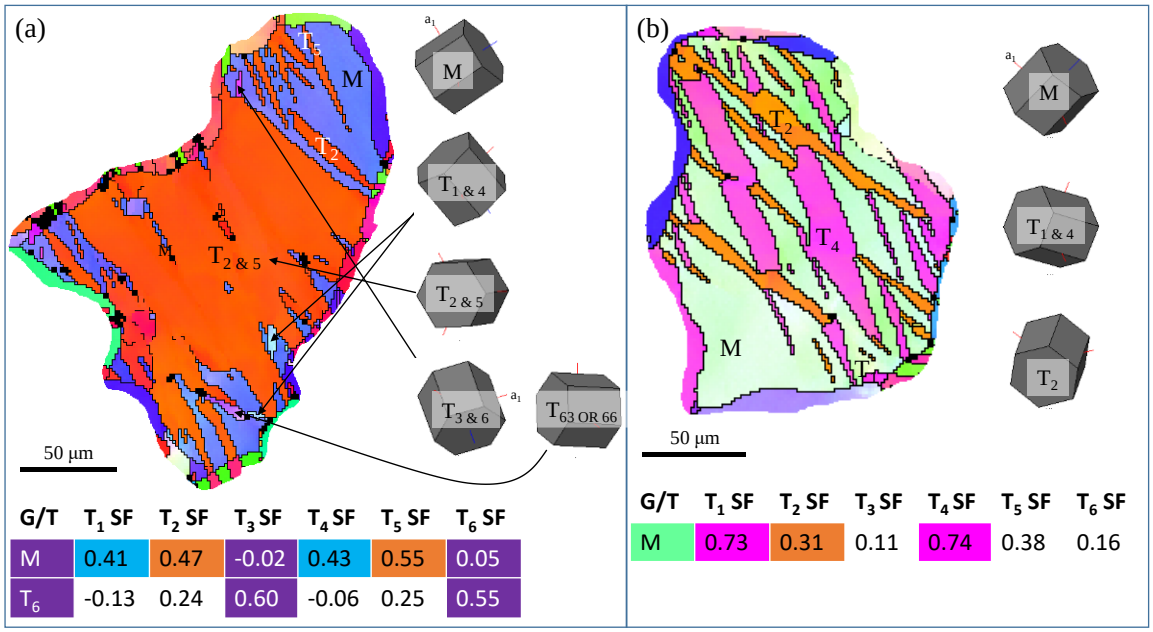

G/T	T_1 SF	T_2 SF	T_3 SF	T_4 SF	T_5 SF	T_6 SF
M	0.41	0.47	-0.02	0.43	0.55	0.05
T_6	-0.13	0.24	0.60	-0.06	0.25	0.55

G/T	T_1 SF	T_2 SF	T_3 SF	T_4 SF	T_5 SF	T_6 SF
M	0.73	0.31	0.11	0.74	0.38	0.16

Figure 57: Two favorable grains identified at 11.5% plastic surface shear strain where (a) a co-zone variant pair dominate twinning and (b) where Type II(b) interactions dominate twinning. Schmid factor tables are color coded for activated variants by inverse pole figure map color. White background in the table indicates that the variant was not activated.

Alternatively, grains containing multiple Type II twin-twin interactions are not consumed as rapidly. Figure 57b exhibits a grain containing branching Type II(b) interactions of both partial and complete apparent crossing structures. The structure is more dense in interactions than that reported in ref. [168] (Figure 34b) where a rolled AZ31B alloy was subjected to compression parallel to the rolling direction. However, the

incomplete structures provide additional insight into the formation process of the apparent crossing structure. From the previous single crystal work (Figure 35), the partial crossing structure was proposed where the formation of TTB_O dramatically shifts the twin boundaries of both interacting variants. Completion of the apparent crossing structure is achieved by the nucleation of the non-crossing twin on the other side of the interaction.

In the less favorably oriented grains, various levels of twinning can be observed, even in grains of similar favorability. Figure 58 highlights two grains of similar favorability but different levels of twinning. Figure 58a highlights a slightly twinned grain predominantly twinned by T_5 and T_6 while Figure 58b highlights a heavily twinned grain twinned primarily by T_2, T_3, and T_6. The first grain shows a granular twin volume close to the upper limit of the unfavorable twin range, but because of the higher resolved shear stress, twins are thicker. The second grain shows a twin volume close to the lower limit of the favorable twin range. The twinning in grains like this is irregular, often having heavy localized twinning in some area and much less in others. Of particular note, the twin-twin interactions between T_2 and the co-zone pair, T_3 and T_6, result in various partial penetrating structures. Towards the top of the grain, a red T_2 band bisects T_3 and T_6. In the middle of the grain, parallel Type II(b) interactions result in a saw blade shaped structure between T_2 and T_6 twins.

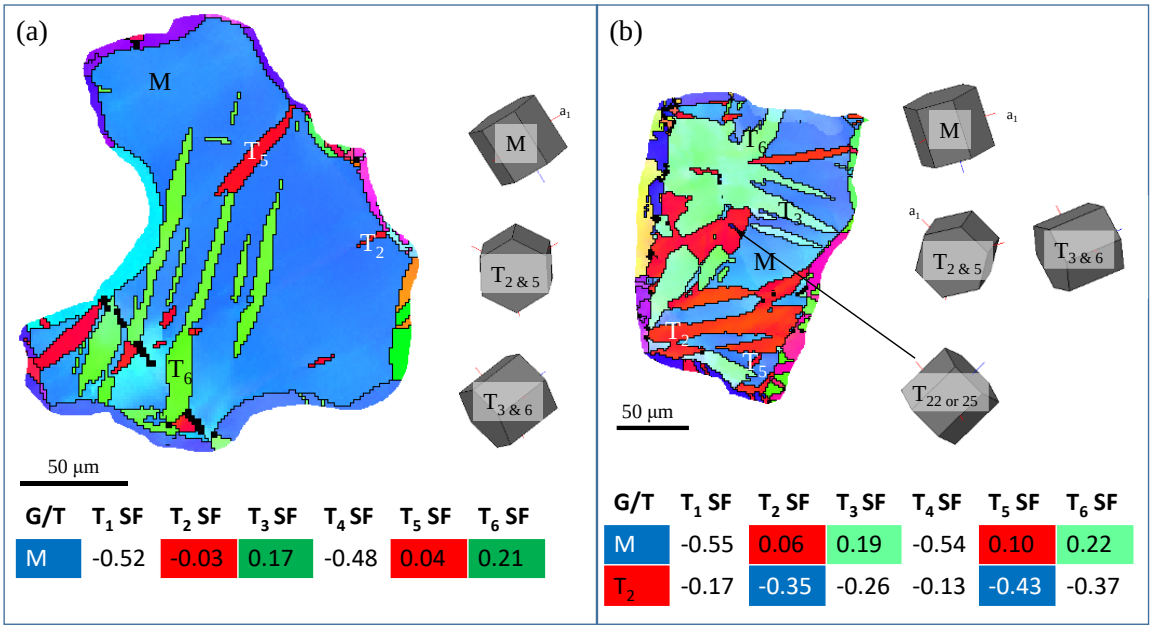

Figure 58: Two similarly less favorable grains identified at 11.5% plastic shear strain where (a) the grain is only slightly twinned and where (b) the grain is significantly twinned with a saw-blade like twin-twin structure. Schmid factor tables are color coded for activated variants by inverse pole figure map color. White background in the table indicates that the variant was not activated.

A schematic explaining the formation of a saw blade-like structure is presented in Figure 59. A pair of cyan T_6 twins grow in parallel towards a red T_2 twin. When the first T_6 twin impacts the T_2 twin, a TTB_O that bisects the two twin traces is formed, causing the shared boundary to shift diagonally down and to the right. TB_2 to the right of the interaction becomes strongly incoherent, rotating about 45° from its coherent trace. Locally, this area of T_2 appears as a saw- or shark-tooth. When the second T_6 twin impacts T_2, the same reaction occurs. These two reactions provide the base for the saw-tooth pattern. Additional thickening of the involved twins complete the transition from the schematic given in Figure 59 to the structure highlighted in Figure 58b.

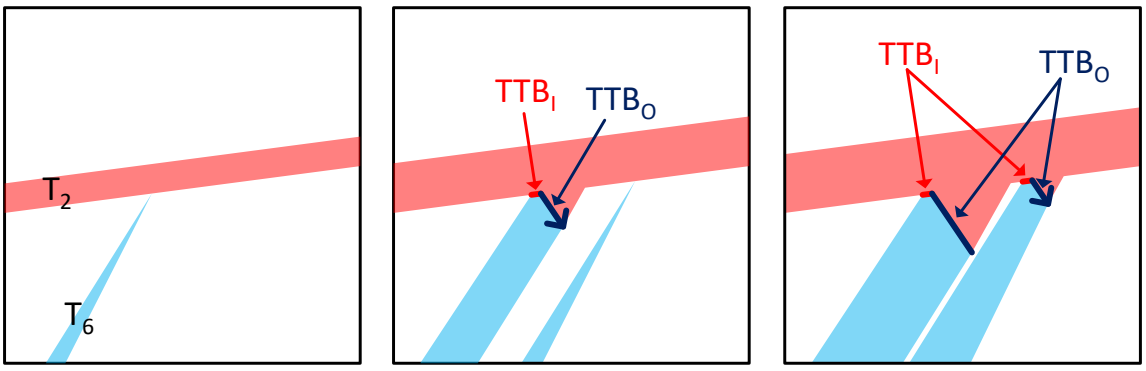

Figure 59: Possible formation process for the saw blade-like twin-twin structure

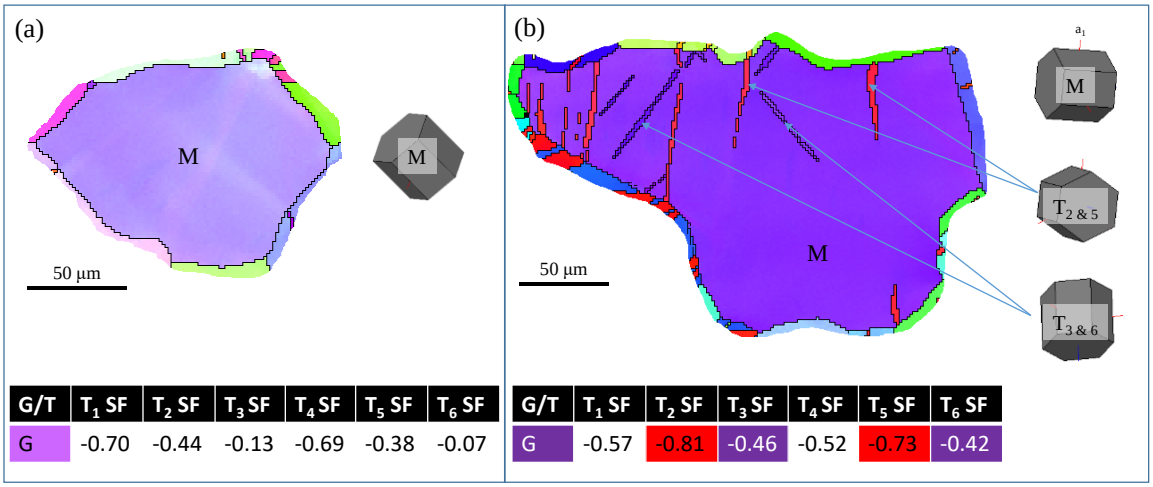

G/T	T_1 SF	T_2 SF	T_3 SF	T_4 SF	T_5 SF	T_6 SF
G	-0.70	-0.44	-0.13	-0.69	-0.38	-0.07

G/T	T_1 SF	T_2 SF	T_3 SF	T_4 SF	T_5 SF	T_6 SF
G	-0.57	-0.81	-0.46	-0.52	-0.73	-0.42

Figure 60: Two grains unfavorable for twinning at 11.5% plastic shear strain containing (a) no twins and (b) several very thin twins. Schmid factor tables are color coded for activated variants by inverse pole figure map color. White background in the table indicates that the variant was not activated.

As with the lower strain level, the highly unfavorable grains contain little to no twinning. Figure 60a shows a grain containing no twins where the *SF* values for all variants is less than zero. The second grain, highlighted in Figure 60b, is unfavorable for twinning yet four variants can be identified. As in the cases of non-Schmid factor twinning in the uniaxial loading, the unfavorable twins here remain thin and small. This supports the claims

by Beyerlein et al. [61] where unfavorable twins may be nucleated due to local stress concentrations but fail to grow much after they are formed.

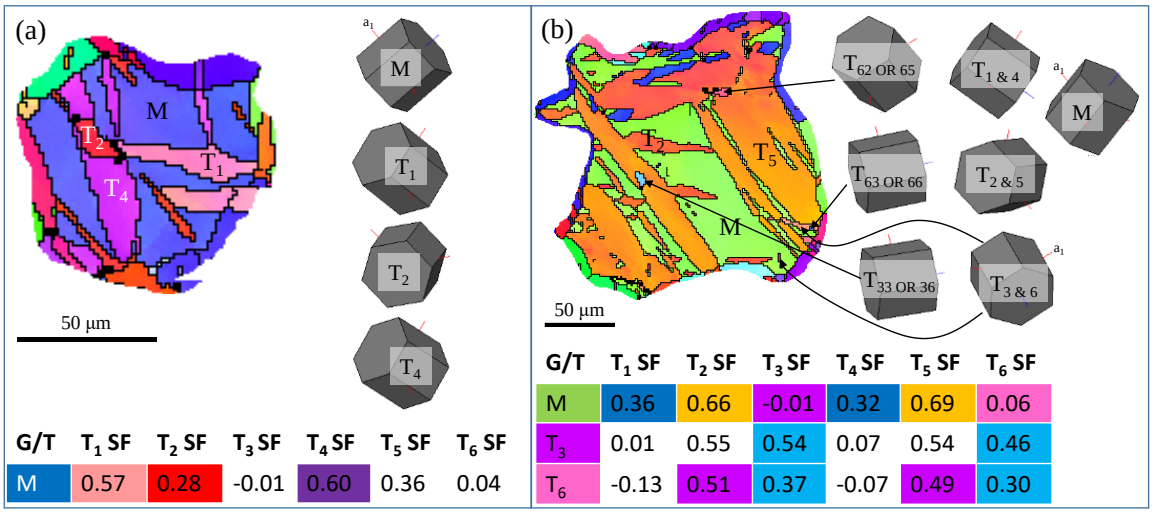

Figure 61: Two unique twin structures resulting from encapsulated primary twins; (a) example of an encapsulated primary twin and (b) an example of encapsulated secondary twins. Schmid factor tables are color coded for activated variants by inverse pole figure map color. White background in the table indicates that the variant was not activated.

It is also noted that twin analysis becomes slightly more difficult at this strain level. With the inconsistent twin nucleation and growth, examples of small, encapsulated twins can be observed. Figure 61a shows a case where a primary T_2 twin is surrounded mostly by a T_1 and T_4 variant roughly in the middle of the grain. As twinning nears exhaustion, these structures can be difficult to identify especially when the encapsulated primary twin is favorable for additional twinning as seen in Figure 61b. In this second case, the unfavorable T_3 and T_6 variants only cover a small space relative to the other four variants. More significantly, these small twins are completely encapsulated in larger primary twins. As with the secondary twins highlighted in Figure 53a and Figure 57a, non-Schmid factor

primary twins are oriented favorably for secondary twinning, so these encapsulated twins become completely twinned. The two examples of the encapsulated secondary twins in this grain are the T_{33} or T_{36} variant contained by T_5 and the T_{62} or T_{65} variant contained by T_2 and/or T_5. Neither secondary twin variant can be completely identified as they completely fill the initial primary twinned areas. As these grains continue twin, primary and secondary twin identification will become more difficult.

5.3.4 Twinning after 22.1% Plastic Shear Strain

Failure of the extruded polycrystalline pure magnesium occurs at 22.1% plastic surface strain with a twin volume fraction of 59.0%. Figure 62 shows the microstructure at failure and reveals the full spectrum of granular twin volume. As with the previous strains, twinning severity can still be described by three levels: highly favorable with severe twinning, less favorable with a large range of twin severity, and unfavorable with little to no twinning.

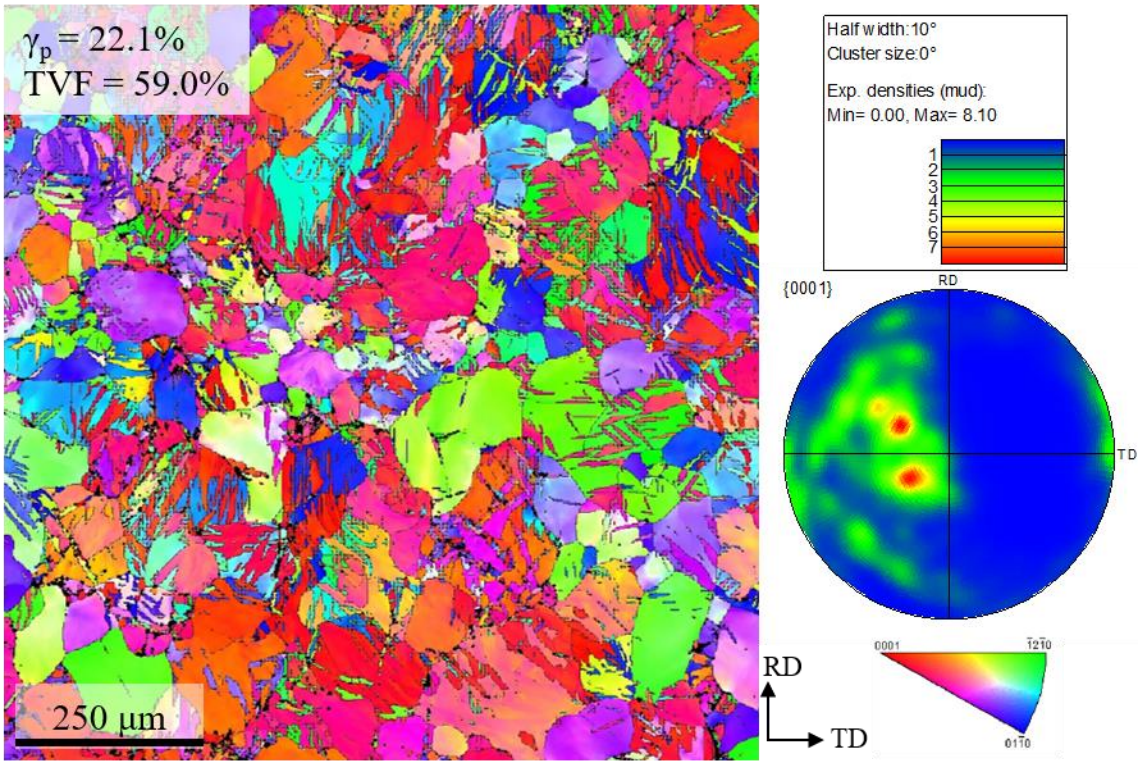

Figure 62: Inverse pole figure map of companion specimen taken at 22.1% plastic shear strain.

Twinning is nearly exhausted in the extremely favorable grains. Figure 63a shows a grain of similar twin structure that was captured at -12.8% compression strain (Figure 42). The grain is primarily twinned by T_1 and T_4, which give the appearance of coalescence due to the low misorientation angle between the co-zone pair. T_2 or T_5, as the trace of the red twin roughly bisects the two possible variants, is the other significant twin activated. However, unlike the structure observed in compression, multiple secondary twins are identified, including some that are the co-zone pair to the matrix material. The second grain, Figure 63b, is similar to the more heavily twinned grains from compression. The

highest ranked variant, T_5, consumes much of the matrix material with some other area consumed by the slightly less favorable T_3 or T_6 variant.

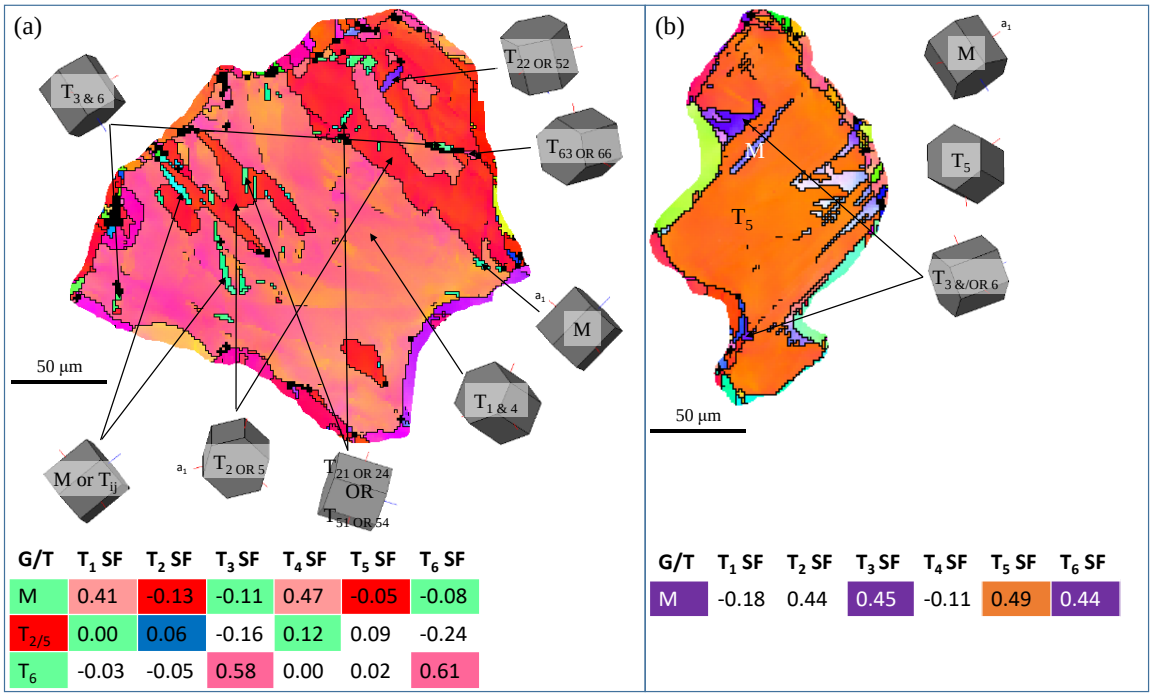

G/T	T_1 SF	T_2 SF	T_3 SF	T_4 SF	T_5 SF	T_6 SF
M	0.41	-0.13	-0.11	0.47	-0.05	-0.08
$T_{2/5}$	0.00	0.06	-0.16	0.12	0.09	-0.24
T_6	-0.03	-0.05	0.58	0.00	0.02	0.61

G/T	T_1 SF	T_2 SF	T_3 SF	T_4 SF	T_5 SF	T_6 SF
M	-0.18	0.44	0.45	-0.11	0.49	0.44

Figure 63: Two favorable grains identified at 22.1% plastic shear strain where (a) a grain is nearly completely twinned with multiple primary twin variants and secondary twins and where (b) a grain is almost completely twinned by one variant. Schmid factor tables are color coded for activated variants by inverse pole figure map color. White background in the table indicates that the variant was not activated.

In the less favorable grains, significant twinning can be observed and twin identification can become very difficult. Two such cases are highlighted in Figure 64. In the first grain, Figure 64a, all six primary variants are directly identified across three distinct twinned regions: the upper, the right, and the bottom left. The bottom left area is the least twinned area by volume to the left of the large T_5 twinned area and below the heavily secondary twinned T_6. Despite its limited area, it contains five primary twin

variants and two secondary twin variants. The small local twin volume is attributed to the unfavorability of T_1, T_2, T_3, and T_6, which are four of the five variants activated in the region. Only T_4 can be considered favorable, but the single band is pinned by the multiple T_2 and T_5 variants on either side. The upper area, defined as the region above the heavily secondary twinned T_6 and left of the T_5 dominated area, is more severely twinned but by fewer variants. T_4 is dominant in this area, with additional secondary twinning present. The right area is severely twinned by T_5, with an enclosed heavily secondary twinned T_3. Accounting for the entire grain, T_4 and T_5 are the most favorable and dominant variants. The less favorable variants, T_3 and T_6, are less active but undergo more significant secondary twinning. Multiple grains of this intermediate favorability show similar trends of unique twin regions. A second such case is presented in Figure 64b where all six variants are activated but a low-*SF* T_1 band bisects the grain. The bottom section is dominated by T_2 and T_5 twinning while the upper section is dominated by T_1 and T_4 twinning. Favorable secondary twinning is found in the low-*SF* T_1 band.

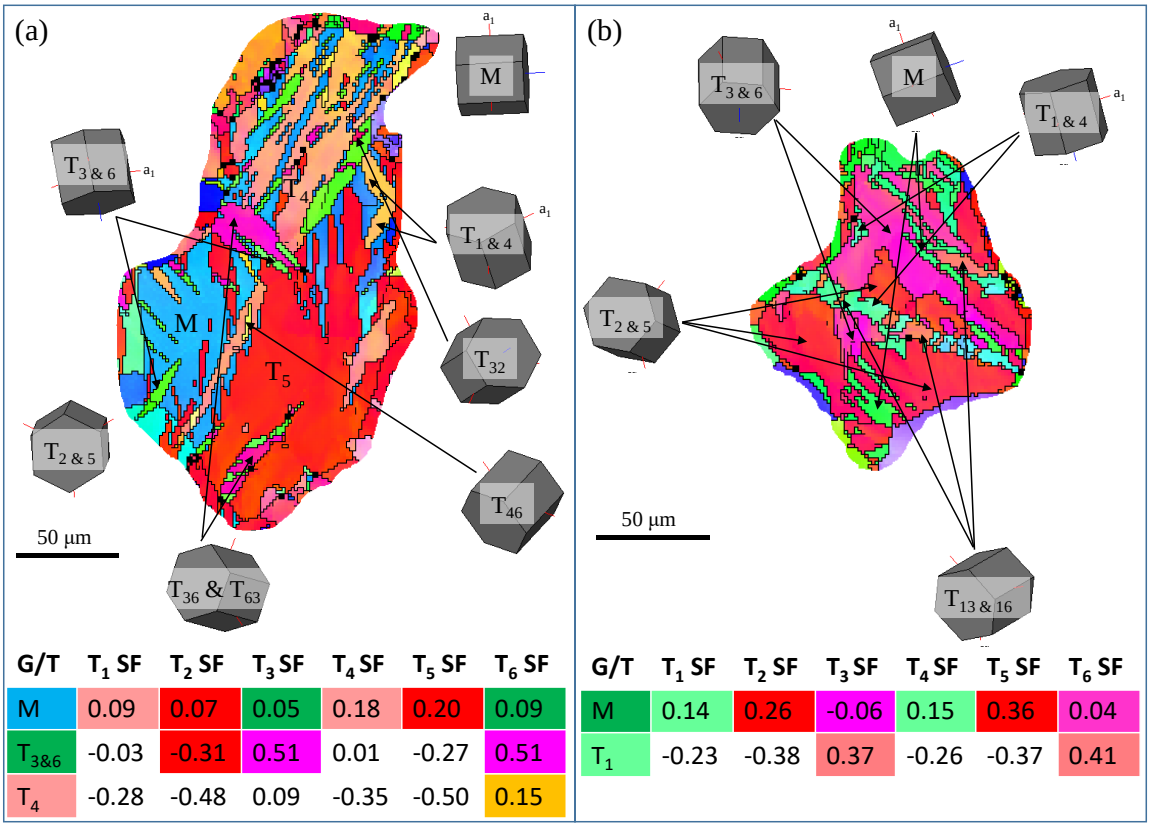

G/T	T_1 SF	T_2 SF	T_3 SF	T_4 SF	T_5 SF	T_6 SF
M	0.09	0.07	0.05	0.18	0.20	0.09
$T_{3\&6}$	-0.03	-0.31	0.51	0.01	-0.27	0.51
T_4	-0.28	-0.48	0.09	-0.35	-0.50	0.15

G/T	T_1 SF	T_2 SF	T_3 SF	T_4 SF	T_5 SF	T_6 SF
M	0.14	0.26	-0.06	0.15	0.36	0.04
T_1	-0.23	-0.38	0.37	-0.26	-0.37	0.41

Figure 64: Two less favorable grains identified at 22.1% plastic shear strain where (a) a grain is inhomogeneously twinned in roughly three separate sections and where (b) a grain is almost completely twinned. Schmid factor tables are color coded for activated variants by inverse pole figure map color. White background in the table indicates that the variant was not activated.

By failure, the range of twinning in the unfavorably oriented grains can be observed. Figure 65a shows an almost untwinned grain where a small band of highly unfavorable T_5 is completely further twinned to T_{53} or T_{56}. A second, small secondary twin is also identified near the grain boundary having a similar oriented as the identifiable secondary twin, suggesting that it may be T_{23} or T_{26}. The second grain, Figure 65b, highlights the upper limit of twinning in an extremely unfavorable grain where all six variants are

identified. In addition to activating all six primary variants, multiple secondary variants are also identified. With this diversity of twinning in unfavorable grains, twinning occurs across the entire spectrum under torsion.

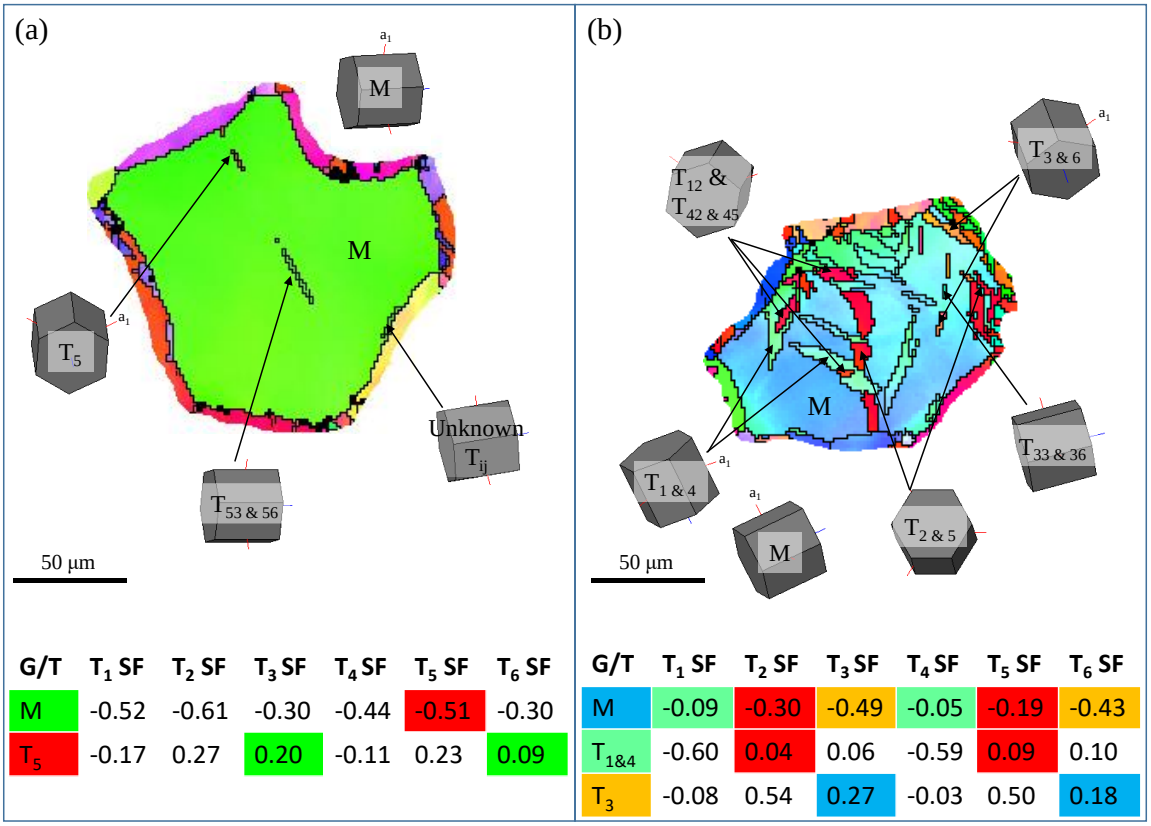

G/T	T_1 SF	T_2 SF	T_3 SF	T_4 SF	T_5 SF	T_6 SF
M	-0.52	-0.61	-0.30	-0.44	-0.51	-0.30
T_5	-0.17	0.27	0.20	-0.11	0.23	0.09

G/T	T_1 SF	T_2 SF	T_3 SF	T_4 SF	T_5 SF	T_6 SF
M	-0.09	-0.30	-0.49	-0.05	-0.19	-0.43
$T_{1\&4}$	-0.60	0.04	0.06	-0.59	0.09	0.10
T_3	-0.08	0.54	0.27	-0.03	0.50	0.18

Figure 65: Two twinning unfavorable grains identified at 22.1% plastic shear strain where (a) a grain is almost completely untwinned and where (b) a grain is moderately twinned. Schmid factor tables are color coded for activated variants by inverse pole figure map color. White background in the table indicates that the variant was not activated.

5.3.5 Further Discussion

Twinning due to monotonic torsion has two key distinctions from twinning under monotonic tension or compression: primary twinning due to highly distributed twin favorability of grains and favorability of further secondary twinning after reorientation.

The texture of rolled or extruded materials can allow for twin favorable orientations for most, if not all, grains for monotonic tension or compression. However, for monotonic torsion, these materials cannot be manipulated to allow all grains to be extremely favorable for twinning across the specimen. Instead, there will be significantly more variability in how favorable grains may be for twinning with a more distributed favorability texture. Three degrees of primary twin favorability have been highlighted for grains in the extruded material: highly favorable, less favorable, and unfavorable. The highly favorable grains are severely twinned by failure, but very few are fully twinned. Generally, the two most favored variants are the dominant active systems but all six variants may be identified even if a few have nearly no resolved shear stress. In few cases, such as the grain highlighted in Figure 63a, even non-*SF* variants can be prominent. The less favorable grains show more variability. At the upper limit, these less favorable grains can show twinning levels similar to that of the highly favorable grains, such as the grains in Figure 64. At the lower end of the spectrum, only moderate levels of twinning can be observed, even at failure. The most diverse twinning results can be observed in the unfavorable grains. In very few of these grains, compression twins or compression tension double twins may be observed, which differs even from torsion of rolled AZ31B where such twinning is observed more [71]. Alternatively, little to no tension twinning may be observed, such as the case shown in Figure 65a. At the most extreme, though, significant tension twinning has been observed such as in the grain highlighted in Figure 65b. When compared to uniaxial tension or compression, favorable twinning due to torsion most closely resembles favorable twinning due to compression. The grains highlighted in Figure 42a (compression) and Figure 63a

(torsion) share many similar features. Twinning is dominated by two co-zone pairs, with several, isolated "island" like twin structures. However, unlike the grain from compression, all six variants are activated by torsion, which is most similar to *c*-axis tension. At the other extreme, the unfavorable grains in torsion can be compared to the uniaxial tension results shown in Figure 47a. Tension parallel to the extrusion direction resulted in grains either remaining untwinned or containing non-*SF* twins. Under torsion, similar observations are made in Figure 65. However, as with the highly favorable grain comparison, torsion differs in two ways: up to all six variants can be identified as opposed to two to four, and the prevalence of secondary twins.

Secondary twinning is the second significant difference for twinning during torsion, especially of the tension-tension variety. No tension-tension double twinning was observed during compression parallel to the extrusion direction, and even minimal secondary twinning was observed during nearly *c*-axis tension of single-crystal magnesium. However, torsion is unique in that both the primary twin and secondary twin could be deemed favorable. Most of the highlighted cases presented for torsion show at least one case of tension-tension double twinning. Figure 66 highlights a grain with significant tension-tension double twinning. The parent material is highly favorable for primary twinning, activating five variants all of which have *SF* values greater than 0.3. The two "least" favorable variants, T_3 and T_6, are the most favorable for additional twinning. This is common in many of the secondary twins highlighted in the grains during torsion – the reorientation of lower ranked primary twins is often favorably oriented for the highly activated secondary twins. In some cases, such as those shown in Figure 66, the highly

favorable secondary twin variant can completely encompass the primary twin. This degree of tension-tension double twinning has not been reported in monotonic tension or compression.

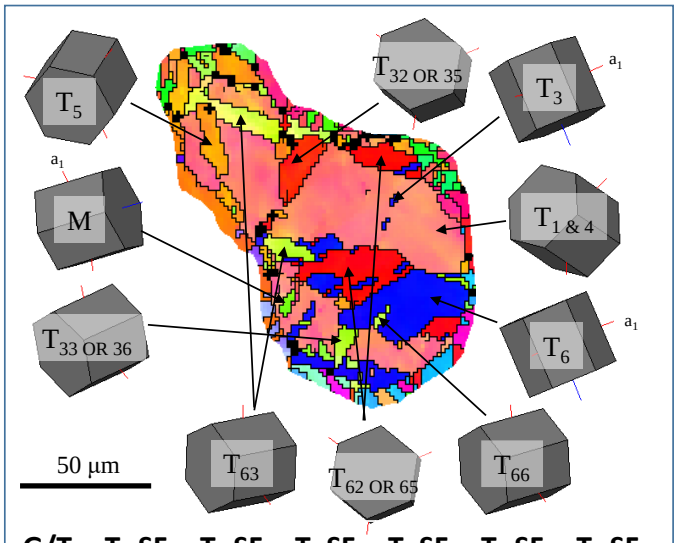

G/T	T_1 SF	T_2 SF	T_3 SF	T_4 SF	T_5 SF	T_6 SF
M	0.68	0.46	0.33	0.75	0.54	0.34
T_3	-0.38	0.10	0.42	-0.34	0.15	0.43
T_6	-0.40	-0.06	0.39	-0.38	-0.01	0.42

Figure 66: A grain at 22.1% plastic shear strain that is heavily twinned. Two of the primary twin variants are significantly twinned further, with some areas being completely consumed by secondary tension twinning.

5.4 Summary

A detailed microstructural analysis was performed of extruded pure polycrystalline magnesium subjected to compression, reversed compression-tension, and free-end torsion loading. Uniaxial compression-tension experiments were conducted parallel to the extrusion direction while torsion was conducted about the extrusion direction. The following conclusions can be made from the analysis:

1) Under compression parallel to the extrusion direction, the number of twins activated in a grain is dependent on the matrix orientation. Grains of nearly $\{10\bar{1}0\}$ orientation (blue colored grains in IPF maps) primarily nucleate one co-zone variant pair of large, similar Schmid factor. Alternatively, grains of nearly $\{2\bar{1}\bar{1}0\}$ orientation (green colored grains in IPF maps) may activate up to two co-zone variant pairs of similar Schmid factor. With fewer activated variants, the $\{10\bar{1}0\}$ grains twin quicker than the $\{2\bar{1}\bar{1}0\}$ grains as there are fewer twin-twin interactions inhibiting twin growth. Despite this, all favorably oriented grains are twinned to exhaustion by failure.
2) Reversed tension after compression result in a combined deformation process by low-Schmid factor twinning, secondary twinning, and detwinning. From large pre-compression strains, the nucleation and growth of favorable secondary tension twins are observed concurrent to the detwinning of primary twins. Low- or non-Schmid factor twins are observed at failure resulting from large local stress effects.
3) The number of secondary tension twin variants activated during the tension reversal is dependent on the amount of twinning produced during pre-compression. Fewer secondary tension twins are observed during tension from -7.3% compression strain, as grains are not completely twinned yet. Alternatively, tension twinning is exhausted by -12.8% compression strain and more secondary tension twin variants are observed from the tension reversal. These secondary twins form residual sub-grains within the detwinned grains, resulting in increased tensile strength.
4) The microstructural evolution of extruded magnesium subjected to torsion is a combination of what has been seen in twinning-favorable loading by compression and

tension. In favorably oriented grains, two to three variants dominate the twin volume per grain similar to the microstructural evolution under compression. However, all six variants can be activated, with the unfavorable variants only covering a very small area within the grain.

5) Twin severity per grain can be separated into three levels by twin favorability and twin volume: highly favorable grains undergo severe twinning, less favorable grains undergo minor to severe twinning, and unfavorable grains undergo either no or only very minor twinning. Microstructurally this is evidenced by the large diversity of visible twins, as compared to the twin exhaustion observed from compression parallel to the extrusion direction.
6) Primary twin nucleation during torsion is less than adequately predicted by Schmid factor for twin variants with Schmid factors ranging from ~ -0.2 to ~ 0.3. Highly favorable variants with Schmid factors greater than 0.4 are often observed. Extremely unfavorable variants with Schmid factors less than -0.3 can also be observed at small to moderate strains, but at a much less degree than the favorable grains. However, twin growth after nucleation is strongly correlated to Schmid factor where more favorable variants tend to encompass more of their parent grain.
7) Secondary tension twins are commonly observed in the torsion microstructures. Less favorable primary twins are often reoriented for favorable secondary twinning. These secondary twin variants often grow rapidly and can completely cover their primary twinned areas.

6 Conclusions

In this dissertation, the microstructural evolution of pure magnesium due to tension twinning activated by tension, compression, strain path change, and torsional loading was examined. The nucleation, growth, and interaction of different twin variants under favorable tension loading was observed by *in situ* methods and characterized by *ex situ* analysis in both single- and poly-crystalline magnesium. Additional analysis was done by *ex situ* methods on poly-crystalline magnesium subjected to compression, subsequent tension after pre-compression, and free-end torsion. From this work, the following conclusions can be made:

1) A hybrid *in situ* OM, *ex situ* EBSD testing procedure was designed to capture deformation of magnesium at high resolution and framerate while still allowing for orientation mapping by EBSD. Applying this method to single-crystal magnesium subjected to nearly *c*-axis tension revealed that basal slip occurs prior to any visible twinning within the observed area. As twinning occurs, the basal slip bands remained visible, although deflected within the twinned region. The measured deflection angle was used to confirm the twin shear value of 0.1295.
2) Schmid factor, while not perfect, provides a strong estimate of the dominant primary twin variants activated during monotonic tension and compression. *C*-axis tension of single crystal magnesium resulted in the activation of all six variants by 3.83% plastic strain. In extruded polycrystalline magnesium subjected to tension, only a few variants are activated in favorably oriented grains despite most variants being favorable due to limited grain size. Under compression, the number of activated variants was dependent

on the orientation of individual grains. $\{10\bar{1}0\}$ Grains predominantly twinned by one variant (or one co-zone variant pair) while $\{1\bar{2}10\}$ grains often contained multiple variants and interactions. However, while secondary tension twins are rare in these monotonic experiments, Schmid factor was a poor indicator of activated secondary twins. The opposite was true for torsion, where the assumptions for Schmid's law are less accurate than those in the uniaxial loading cases. In the torsion cases, Schmid factor is an adequate predictor of activated variants in extremely favorable grains. However, variants with a Schmid factor of less than or roughly equal to 0 can also be observed in less favorably oriented grains. Generally, the very unfavorable variants with negative Schmid factors that are activated do not grow very large while the other variants can consume much more of the matrix. Thus, all six variants can be identified in both highly favorable and slightly unfavorable oriented grains. Schmid factor is a strong indicator for secondary twins from torsion, and due to the more unique favorable orientations compared to the uniaxial cases, secondary twins can accommodate much larger volumes.

3) Cross-grain twin pair, or adjoining twin pair, formation is predominantly driven by high geometric compatibility, *m'*, of the twins across the grain boundary. In extruded polycrystalline pure magnesium subjected to tension, initial twin formation follows Schmid's law where variants of significantly large Schmid factor greater than 0.4 are activated. Cross grain pairs were also found to be highly favorable on their own, but also were geometrically favorable having *m'* values larger than 0.9. Under torsion where low and negative Schmid factor twins can be observed, geometric compatibility

factor is shown to be a much stronger indicator of cross-grain twin pair formation. It is proposed that a favorable twin is first nucleated and grown in a favorably oriented grain. This twin assists in the nucleation of a similarly oriented, although unfavorable twin in an adjacent grain from the grain boundary.

4) Intrusion-like twin-twin structures can result from both Type I co-zone and Type II non-co-zone twin-twin interactions. A sharp intrusion Type I interaction was observed by *in situ* methods in single-crystal magnesium. The penetrating appearance is due to the acute angle boundary formation and energetically favorable, non-twin-twin boundary development on the obtuse angle side. Intrusion-like structures from Type II interactions involve parallel interactions of the same type. In single-crystal, intrusion-like structures result from the nucleation, growth, and coalescence of one of the interacting twins, migrating the twin boundary further down the barrier twin. In torsion, saw-blade like twin-twin structures result from parallel Type II(b) interactions.
5) The effect of pre-twinning by compression on subsequent reversed loading was detailed for the first time. At significant levels of pre-twinning (TVF > 70%), the reversed loading results in a combination of both detwinning and secondary twinning depending on the severity. When twinning was exhausted during pre-compression, more secondary twinning was observed during tension than the less severe twinned state. Regardless of twinned state, the initial primary twins are almost completely detwinned or secondary twinned by tensile fracture. Additional non-Schmid factor twins are observed in the detwinned regions, along with forming tension-tension-tension tertiary twins in the secondary twinned regions.

6) Free-end torsion of the extruded pure polycrystalline magnesium revealed a full spectrum of twinning based on twin favorable orientations: extremely favorable, less favorable, and unfavorable. All six tension twin variants could be observed in the extremely favorable and less favorable grains, although the unfavorable variants may not be twinned to significant degree. The extremely favorable grains are rapidly twinned. The less favorable grains show a more varied response, with some grains being twinned quickly and some being twinned slowly. The unfavorable grains show no to moderate twinning by failure. As such, the twin volume cannot reach similar values of monotonic tension or compression. Additionally, because of the multiaxial loading, some primary twins are oriented favorably for additional twinning, so secondary tension twinning occurs to a more significant degree than other monotonic loading cases. Favorable secondary twins can completely encompass their primary twins.

6.1 Future Work

The work in this dissertation has examined the process of twinning involving nucleation, propagation, thickening, and interaction in both polycrystalline and single-crystalline magnesium. To perform this work, a method of manufacturing single-crystal specimens was developed along with a hybrid *in situ* observation – *ex situ* analysis testing procedure to capture live deformation processes. The work provided in this study have created a groundwork that can be further expanded upon, including:

1. Develop a digital image correlation method of measuring strain in the small dog-bone shaped specimens to improve the *in situ* OM, *ex situ* EBSD testing procedure. With a

more accurate strain measurement, the experimental results can be better correlated with the key microstructural development that was recorded *in situ*.

2. The grip device used in the hybrid testing procedure can be further modified to easily allow compression loading. This will allow for better study of compression and reversed loading that could not be adequately studied for this dissertation. Additional single-crystal orientations can be tested to better study other twin and slip systems.
3. With an improved grip system, strain path change experiments utilizing the *in situ* OM, *ex situ* EBSD testing procedure can be performed to better capture the process of detwinning and secondary twinning. This may be performed on both single-crystalline and polycrystalline materials to best capture the process of detwinning and secondary twinning when the loading is reversed.
4. Revisit the cross-grain twin pair formation experiments using a different etchant to reveal grain boundaries and a different loading rate to slow down the nucleation process. Both will allow a clearer observation of the adjoining twin pair nucleation process during the *in situ* loading.

Appendix A

A. Schmid's Law and Calculating Schmid Factor

The activation of any slip or twin system is assumed when the resolved shear stress on a given deformation system exceeds its associated critical resolved shear stress – this is known as Schmid's law [219]. Schmid's law is expressed as:

$$\tau = m\sigma \tag{A1}$$

where τ is the resolved shear stress, m is Schmid factor, and σ is the applied axial load. Schmid factor is dependent on the slip (or twin) plane normal and slip (or twin) direction relative to the loading axis. The simplified term for m is given as:

$$m = \cos(\phi)cos(\lambda) \tag{A2}$$

where ϕ is the angle between the loading direction and the shear plane normal and λ is the angle between the loading direction and the shear direction of a given deformation system. Physically, these relationships can be visualized in Figure A1.

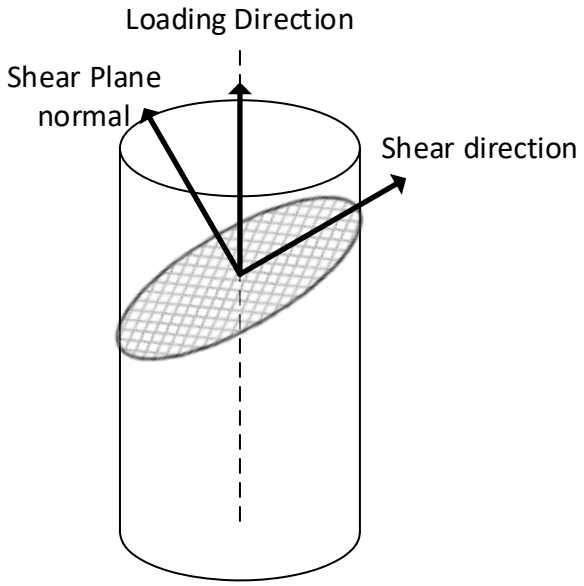

Figure A1: Visualization of the key angles used in calculating Schmid factor

For a uniaxial load, the maximum Schmid factor can be 0.5 for when the angle between the loading axis and both the shear plane normal and shear direction is 45°. However, torsional loading is a multiaxial loading case. To use this method, the torsion load must be transformed to two principal stresses. The Schmid factor is then the superposition of the Schmid factors of the two principal stresses. Alternatively, Schmid factor can be calculated by the rotation of a unit sample stress tensor to the shear plane. This allows for Schmid factor or resolved shear stress calculations of both simple and complex loading cases. This was the method used for calculating Schmid factors in this dissertation.

The method for rotating the stress tensor requires transforming the stress tensor from the sample coordinate system to the deformation system coordinate system. To do this, a careful rotation of coordinate systems is required. This transformation process will be

explained here specifically for hcp magnesium materials assuming that the sample stress state is known.

With the sample stress tensor, σ^{sam}, known, the first rotation converts the sample stress to the crystal unit cell stress, σ^{cry}, using the three Euler angles, (φ_1, ϕ, φ_2) of the crystal as provided by EBSD, where the angles represent a Z-X-Z series of rotations. It is important to note that different EBSD systems will have a different base coordinate system from which the Euler angles are derived. Additionally, further manipulations may be required to correctly represent the actual crystal orientation of a given point [220].

$$\sigma^{cry} = \begin{bmatrix} \sigma_x & \tau_{xy} & \tau_{xz} \\ \tau_{yx} & \sigma_y & \tau_{yz} \\ \tau_{zx} & \tau_{zy} & \sigma_z \end{bmatrix} \tag{A3}$$

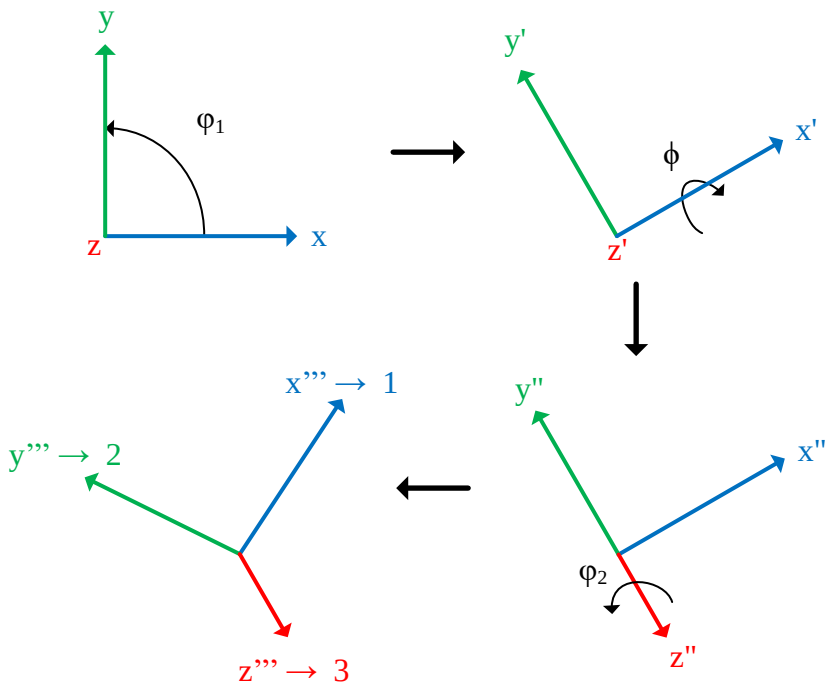

Figure A2: Euler angle rotations for the hcp crystal structure

Figure A2 shows the Euler angle rotations, assuming no additional manipulations are required. The three individual rotations from Euler angles can be defined as R_z, $R_{x'}$, and $R_{z''}$ and are performed in that order to yield the combined singular rotation matrix, **R**. The crystal unit cell stress, σ^{cry}, can then be calculated using **R** and σ^{sam}.

$$R_z = \begin{bmatrix} \cos(\varphi_1) & \sin(\varphi_1) & 0 \\ -\sin(\varphi_1) & \cos(\varphi_1) & 0 \\ 0 & 0 & 1 \end{bmatrix} \quad \text{(A4a)}$$

$$R_{x'} = \begin{bmatrix} 1 & 0 & 0 \\ 0 & \cos(\phi) & \sin(\phi) \\ 0 & -\sin(\phi) & \cos(\phi) \end{bmatrix} \quad \text{(A4b)}$$

$$R_{z''} = \begin{bmatrix} \cos(\varphi_2) & \sin(\varphi_2) & 0 \\ -\sin(\varphi_2) & \cos(\varphi_2) & 0 \\ 0 & 0 & 1 \end{bmatrix} \quad \text{(A4c)}$$

$$\mathbf{R} = R_{z''} * R_{x'} * R_z \quad \text{(A4d)}$$

$$\sigma_{ij}^{cry} = \mathbf{R} * \sigma_{ij} * \mathbf{R^{-1}} \quad \text{(A4e)}$$

The slip/twin plane and slip/twin direction must then be transformed from magnesium's hexagonal indices to an orthonormal coordinate system based on **x**, **y**, and **z**. Both the plane and direction must first be transformed from the hexagonal base to a rhombohedral base before finally be transformed to an orthonormal base. In the hexagonal basis, an arbitrary direction can be defined as **D** using Miller-Bravais indices [*u v t w*] with respect to four basis vectors $\mathbf{a_1}$, $\mathbf{a_2}$, $\mathbf{a_3}$, and **c**. In the rhombohedral system, **D** can be defined using Miller indices [*U V W*] with respect to the three basis vectors $\mathbf{a_1}$, $\mathbf{a_2}$, and **c**.

$$\mathbf{D} = u\boldsymbol{a_1} + v\boldsymbol{a_2} + t\boldsymbol{a_3} + w\mathbf{c} \quad \text{(A5a)}$$

$$\mathbf{D} = U\boldsymbol{a_1} + V\boldsymbol{a_2} + W\mathbf{c} \quad \text{(A5b)}$$

The transformation of the Miller-Bravais indices in the hexagonal system to the Miller indices in the rhombohedral system is:

$$U = u - t, \quad V = v - t, \quad W = w \tag{A6a}$$

$$u = \frac{1}{3}(2U - V), \quad v = \frac{1}{3}(2V - U), \quad t = -(U + V), \quad w = W \tag{A6b}$$

For a plane, **P**, Miller-Bravais indices (*h k i l*) are used in the hexagonal basis while Miller indices (*H K L*) are used in the rhombohedral system. The plane is expressed in terms of reciprocal vectors $\mathbf{a_1^*}$, $\mathbf{a_2^*}$, $\mathbf{a_3^*}$, $\mathbf{c}^*$, for the hexagonal system and $\mathbf{A_1^*}$, $\mathbf{A_2^*}$, $\mathbf{C}^*$ for the rhombohedral system:

$$\mathbf{P} = h\mathbf{a_1^*} + k\mathbf{a_2^*} + i\mathbf{a_3^*} + l\mathbf{c}^* \tag{A7a}$$

$$\mathbf{P} = H\mathbf{A_1^*} + K\mathbf{A_2^*} + L\mathbf{C}^* \tag{A7b}$$

The relationship between the Miller-Bravais hexagonal indices and the Miller rhombohedral indices are as follows:

$$H = h, \quad K = k, \quad L = l \tag{A8a}$$

$$h = H, \quad k = K, \quad i = -(h + k), \quad l = L \tag{A8b}$$

Thus, the slip/twin planes and the slip/twin shear directions can be transformed from the four basis hexagonal system to a three basis rhombohedral system. If the direction **D** lies on plane **P**, orthogonality must be satisfied such that $\mathbf{P} \cdot \mathbf{D} = \mathbf{0}$. To transform the plane and direction from the rhombohedral ($\mathbf{a}_1$, $\mathbf{a}_2$, $\mathbf{c}$) system to an orthogonal ($\mathbf{e}_1$, $\mathbf{e}_2$, $\mathbf{e}_3$) system, a transformation matrix, **L**, must be used [221]:

$$L = \begin{pmatrix} 1 & -\frac{1}{2} & 0 \\ 0 & \frac{\sqrt{3}}{2} & 0 \\ 0 & 0 & \frac{c}{a} \end{pmatrix} \tag{A9}$$

where *a* and *c* are the lattice parameters for magnesium previously defined in Chapter 2.1. Transforming the rhombohedral system using **L**, the slip/twin direction and plane in the orthogonal system can be determined by:

$$\mathbf{D}_{[e_1e_2e_3]} = \mathbf{L}\mathbf{D}_{[UVW]} \tag{A10a}$$

$$\mathbf{P}_{[e_1e_2e_3]} = \mathbf{P}_{[HKL]}\mathbf{L}^{-1} \tag{A10b}$$

where both **D** vectors are column vectors and both **P** vectors are row vectors.

The orthogonal plane **P** and direction **D** are aligned with the local coordinates **z** and **x** on the slip/twin plane, respectively. Converting these to unit vectors will transform the coordinate system from orthogonal to orthonormal by:

$$\mathbf{n} = \frac{\mathbf{P}}{\sqrt{\mathbf{P}\cdot\mathbf{P}}} \tag{A11a}$$

$$\mathbf{b} = \frac{\mathbf{D}}{\sqrt{\mathbf{D}\cdot\mathbf{D}}} \tag{A11a}$$

where **n** and **b** are the unit vectors for the shear plane normal and shear direction. To complete the coordinate system, the third basis vector can be obtained by cross product of the **n** and **b**, where both are column vectors.

$$\mathbf{t} = \mathbf{n} \times \mathbf{b} \tag{A12}$$

A second rotation matrix, **A**, is the compilation of the orthonormal basis vectors and corresponds to the rotation from crystal coordinates to the slip/twin system coordinates:

$$\mathbf{A} = \begin{pmatrix} \mathbf{b_1} & \mathbf{t_1} & \mathbf{n_1} \\ \mathbf{b_2} & \mathbf{t_2} & \mathbf{n_2} \\ \mathbf{b_3} & \mathbf{t_3} & \mathbf{n_3} \end{pmatrix} \tag{A13}$$

where the subscript numbers are indices from the basis vectors **b**, **t**, and **n**. The crystal stress tensor can be rotated to the slip/twin system by:

$$\sigma_{ij}^{sys} = \mathbf{A} * \sigma_{ij}^{cry} * \mathbf{A^{-1}} \tag{A14}$$

The new coordinate system can be visualized in Figure A3. The final stress tensor achieved from Equation A14 is aligned such that the diagonal terms correspond to axial stresses along the shear direction, transverse shear direction, and shear plane normal, respectively. The upper and lower triangular terms correspond to the shear stress terms. Thus, the resolved shear stress term corresponding to the shear direction on the shear plane is σ_{13}^{sys}.

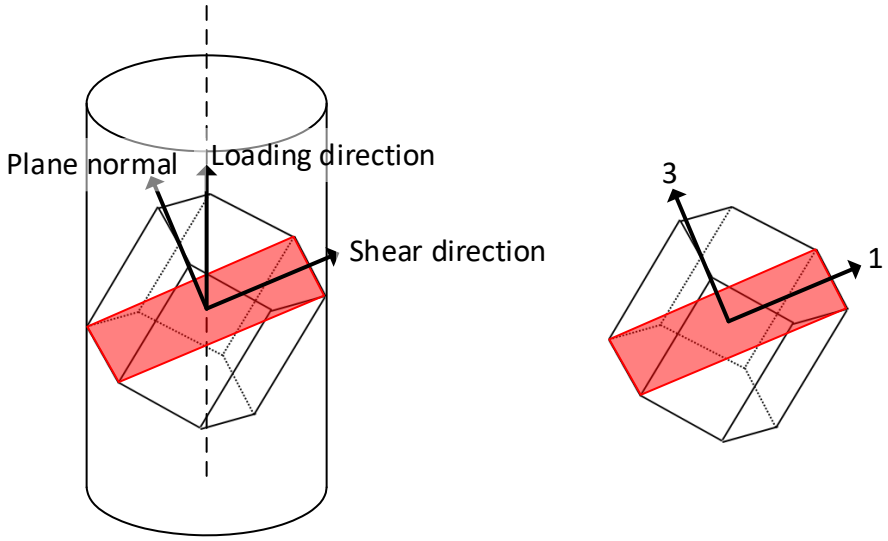

Figure A3: The coordinate system for the final stress tensor relative to the shear plane and shear direction. Axis "1" is aligned along the shear direction while axis "3" is aligned with the shear plane normal.

References

[1] B.L. Mordike, T. Ebert, Magnesium Properties - applications - potential, Mater. Sci. Eng. A. 302 (2001) 37–45. https://doi.org/10.1016/S0921-5093(00)01351-4.

[2] A.A. Luo, Magnesium: Current and potential automotive applications, Jom. 54 (2002) 42–48. https://doi.org/10.1007/BF02701073.

[3] F.H. Froes, Advanced metals for aerospace and automotive use, Mater. Sci. Eng. A. 184 (1994) 119–133. https://doi.org/https://doi.org/10.1016/0921-5093(94)91026-X.

[4] F.H. Froes, D. Eliezer, E. Aghion, The Science , Technology , and Applications of Magnesium, (1998).

[5] D. Eliezer, E. Aghion, F.H. Froes, Magnesium Science, Technology, and Applications, Adv. Perform. Mater. 5 (1998) 201–212. https://doi.org/https://doi.org/10.1023/A:1008682415141.

[6] A.A. Luo, Magnesium casting technology for structural applications, J. Magnes. Alloy. 1 (2013) 2–22. https://doi.org/10.1016/j.jma.2013.02.002.

[7] H.T. Kang, T. Ostrom, Mechanical behavior of cast and forged magnesium alloys and their microstructures, 490 (2008) 52–56. https://doi.org/10.1016/j.msea.2008.02.030.

[8] C.J. Bettles, M.A. Gibson, Current wrought magnesium alloys: Strengths and weaknesses, Jom. 57 (2005) 46–49. https://doi.org/10.1007/s11837-005-0095-0.

[9] S.R. Agnew, Wrought magnesium: A 21st century outlook, Jom. 56 (2004) 20–21.

https://doi.org/10.1007/s11837-004-0120-8.

[10] D. Culbertson, Q. Yu, Y. Jiang, In situ observation of cross-grain twin pair formation in pure magnesium, Philos. Mag. Lett. 98 (2018) 139–146. https://doi.org/10.1080/09500839.2018.1498599.

[11] D. Culbertson, Q. Yu, Y. Jiang, On the intrusion-like co-zone twin-twin structure: an in situ observation, Mater. Lett. 286 (2020) 129140. https://doi.org/10.1016/j.matlet.2020.129140.

[12] D. Culbertson, Q. Yu, J. Wang, Y. Jiang, Pre-compression effect on microstructure evolution of extruded pure polycrystalline magnesium during reversed tension load, Mater. Charact. 134 (2017) 41–48. https://doi.org/10.1016/j.matchar.2017.10.003.

[13] P.G. Partridge, The crystallography and deformation modes of hexagonal close-packed metals, Metall. Rev. 12 (1967) 169–194. https://doi.org/10.1179/mtlr.1967.12.1.169.

[14] J.W. Christian, S. Mahajan, Deformation twinning, Prog. Mater. Sci. 39 (1995) 1–157. https://doi.org/10.1016/0079-6425(94)00007-7.

[15] R. V. Mises, Mechanik der plastischen Formänderung von Kristallen, ZAMM - Zeitschrift Für Angew. Math. Und Mech. 8 (1928) 161–185. https://doi.org/10.1002/zamm.19280080302.

[16] M.H. Yoo, Slip, twinning, and fracture in hexagonal close-packed metals, Metall. Trans. A. 12 (1981) 409–418. https://doi.org/10.1007/BF02648537.

[17] K.Y. Xie, Z. Alam, A. Caffee, K.J. Hemker, Pyramidal I slip in c-axis compressed Mg single crystals, Scr. Mater. 112 (2016) 75–78.

https://doi.org/10.1016/j.scriptamat.2015.09.016.

[18] E.C. Burke, W.R. Hibbard, Plastic Deformation of Magnesium Single Crystals, J. Met. 4 (1952) 295–303. https://doi.org/10.1007/bf03397694.

[19] P.W. Bakarian, C.H. Mathewson, Slip and Twinning in Magnesium single Crystals at Elevated Temperatures, Trans. Am. Inst. Min. Metall. Eng. 152 (1943) 226–254. https://archive.org/details/in.ernet.dli.2015.155681/page/n229/mode/2up.

[20] H. Asada, H. Yoshinaga, Temperature and orientation dependence of the plasticity of magnesium single crytsals, J. Japan Inst. Met. 23 (1959) 649–652.

[21] E. Schmid, W. Boas, Plasticity of crystals with special reference to metals, Chapman & Hall, London, 1968.

[22] B. Bhattacharya, M. Niewczas, Work-hardening behaviour of Mg single crystals oriented for basal slip, Philos. Mag. 91 (2011) 2227–2247. https://doi.org/10.1080/14786435.2011.555783.

[23] A. Chapuis, J.H. Driver, Temperature dependency of slip and twinning in plane strain compressed magnesium single crystals, Acta Mater. 59 (2011) 1986–1994. https://doi.org/10.1016/j.actamat.2010.11.064.

[24] B.C. Wonsiewicz, Plasticity of Magnesium Crystals, Massachusetts Institute of Technology, 1966.

[25] R.E. Reed-Hill, W.D. Robertson, Deformation of magnesium single crystals by nonbasal slip, JOM. 9 (1957) 496–502. https://doi.org/10.1007/bf03397907.

[26] T. Obara, H. Yoshinga, S. Morozumi, {11-22}〈1123〉 Slip system in magnesium, Acta Metall. 21 (1973) 845–853. https://doi.org/10.1016/0001-6160(73)90141-7.

[27] Q. Yu, J. Zhang, Y. Jiang, Direct observation of twinning-detwinning-retwinning on magnesium single crystal subjected to strain-controlled cyclic tension-compression in [0 0 0 1] direction, Philos. Mag. Lett. 91 (2011) 757–765. https://doi.org/10.1080/09500839.2011.617713.

[28] R. Abbaschian, R.E. Reed-Hill, Physical Metallurgy Principles, 4th ed., Cengage Learning, 2008.

[29] U.F. Kocks, D.G. Westlake, The Importance of Twinning for the Ductility of CPH Polycrystals, Trans. Metall. Soc. AIME. 239 (1967) 1107–1109.

[30] R.W. Cahn, Plastic deformation of alpha-uranium; twinning and slip, Acta Metall. 1 (1953) 49–52. https://doi.org/10.1016/0001-6160(53)90009-1.

[31] R.E. Reed-Hill, W.D. Robertson, Additional modes of deformation twinning in magnesium, Acta Metall. 5 (1957) 717–727.

[32] H. Miura, X. Yang, T. Sakai, H. Nogawa, S. Miura, Y. Watanabe, J.J. Jonas, High temperature deformation and extended plasticity in Mg single crystals, Philos. Mag. 85 (2005) 3553–3565. https://doi.org/10.1080/14786430500228440.

[33] H. Yoshinaga, Ryo Horiuchi, Deformation Mechanisms in Magnesium Single Crystals Compressed in the Direction Parallel to Hexagonal Axis, Trans. Japan Inst. Met. 4 (1963) 1–8.

[34] M.H. Yoo, J.K. Lee, Deformation twinning in h.c.p. metals and alloys, Philos. Mag. A. 63 (1991) 987–1000. https://doi.org/10.1080/01418619108213931.

[35] F. Mokdad, D.L. Chen, D.Y. Li, Single and double twin nucleation, growth, and interaction in an extruded magnesium alloy, Mater. Des. 119 (2017) 376–396.

https://doi.org/10.1016/j.matdes.2017.01.072.

[36] N. Stanford, R.K.W. Marceau, M.R. Barnett, The effect of high yttrium solute concentration on the twinning behaviour of magnesium alloys, Acta Mater. 82 (2015) 447–456. https://doi.org/10.1016/j.actamat.2014.09.022.

[37] K.H. Eckelmeyer, R.W. Hertzberg, Deformation in wrought Mg-9Wt Pct Y, Metall. Trans. 1 (1970) 3411–3414. https://doi.org/10.1007/BF03037872.

[38] N. Stanford, Observation of {1121} twinning in a Mg-based alloy, Philos. Mag. Lett. 88 (2008) 379–386. https://doi.org/10.1080/09500830802070793.

[39] H. Yoshinaga, T. Obara, S. Morozumi, Twinning deformation in magnesium compressed along the C-axis, Mater. Sci. Eng. 12 (1973) 255–264. https://doi.org/10.1016/0025-5416(73)90036-0.

[40] R. Aghababaei, S.P. Joshi, Micromechanics of tensile twinning in magnesium gleaned from molecular dynamics simulations, Acta Mater. 69 (2014) 326–342. https://doi.org/10.1016/j.actamat.2014.01.014.

[41] S.G. Song, G.T. Gray, Structural interpretation of the nucleation and growth of deformation twins in Zr and Ti-I. Application of the coincidence site lattice (CSL) theory to twinning problems in h.c.p. structures, Acta Metall. Mater. 43 (1995) 2325–2337. https://doi.org/10.1016/0956-7151(94)00433-1.

[42] J. Wang, I.J.J. Beyerlein, C.N.N. Tomé, An atomic and probabilistic perspective on twin nucleation in Mg, Scr. Mater. 63 (2010) 741–746. https://doi.org/10.1016/j.scriptamat.2010.01.047.

[43] H. El Kadiri, C.D. Barrett, C.N. Tome, Why are {10-12} twins profuse in

magnesium ?, 85 (2015) 354–361. https://doi.org/10.1016/j.actamat.2014.11.033.

[44] A. Khosravani, D.T.T. Fullwood, B.L.L. Adams, T.M.M. Rampton, M.P.P. Miles, R.K.K. Mishra, Nucleation and propagation of { 1 0 -1 2 } twins in AZ31 magnesium alloy, Acta Mater. 100 (2015) 202–214. https://doi.org/10.1016/j.actamat.2015.08.024.

[45] X. Wang, P. Mao, Z. Liu, Z. Wang, F. Wang, L. Zhou, Z. Wei, Nucleation and growth analysis of {10-12} extension twins in AZ31 magnesium alloy, J. Alloys Compd. 817 (2020) 152967. https://doi.org/10.1016/j.jallcom.2019.152967.

[46] C.N. Tomé, I.J. Beyerlein, J. Wang, R.J. McCabe, A multi-scale statistical study of twinning in magnesium, JOM. 63 (2011) 19–23. https://doi.org/10.1007/s11837-011-0038-x.

[47] J. Li, X. Li, M. Yu, M. Sui, Nucleation mechanism of {$10\bar{1}2$} twin with low Schmid factor in hexagonal close-packed metals, Mater. Sci. Eng. A. 791 (2020) 139542. https://doi.org/10.1016/j.msea.2020.139542.

[48] J. Wang, S.K. Yadav, J.P. Hirth, C.N. Tomé, I.J. Beyerlein, Pure-Shuffle Nucleation of Deformation Twins in Hexagonal-Close-Packed Metals, Mater. Res. Lett. 1 (2013) 126–132. https://doi.org/10.1080/21663831.2013.792019.

[49] S.R. Agnew, C.N. Tomé, D.W. Brown, T.M. Holden, S.C. Vogel, Study of slip mechanisms in a magnesium alloy by neutron diffraction and modeling, Scr. Mater. 48 (2003) 1003–1008. https://doi.org/10.1016/S1359-6462(02)00591-2.

[50] M.R. Barnett, Z. Keshavarz, A.G. Beer, D. Atwell, Influence of grain size on the compressive deformation of wrought Mg-3Al-1Zn, Acta Mater. 52 (2004) 5093–

5103. https://doi.org/10.1016/j.actamat.2004.07.015.

[51] M.A. Meyers, O. Vöhringer, V.A. Lubarda, The onset of twinning in metals: A constitutive description, Acta Mater. 49 (2001) 4025–4039. https://doi.org/10.1016/S1359-6454(01)00300-7.

[52] J. Wang, J.P. Hirth, C.N. Tomé, (1¯0 1 2) Twinning nucleation mechanisms in hexagonal-close-packed crystals, Acta Mater. 57 (2009) 5521–5530. https://doi.org/10.1016/j.actamat.2009.07.047.

[53] M. Arul Kumar, A.K. Kanjarla, S.R. Niezgoda, R.A. Lebensohn, C.N. Tomé, Numerical study of the stress state of a deformation twin in magnesium, Acta Mater. 84 (2015) 349–358. https://doi.org/10.1016/j.actamat.2014.10.048.

[54] P.G. Partridge, Cyclic twinning in fatigued close-packed hexagonal metals, Philos. Mag. 12 (1965) 1043–1054. https://doi.org/10.1080/14786436508228133.

[55] B.M. Morrow, R.J. McCabe, E.K. Cerreta, C.N. Tomé, Observations of the Atomic Structure of Tensile and Compressive Twin Boundaries and Twin–Twin Interactions in Zirconium, Metall. Mater. Trans. A Phys. Metall. Mater. Sci. 45 (2014) 5891–5897. https://doi.org/10.1007/s11661-014-2481-0.

[56] B.M. Morrow, E.K. Cerreta, R.J. McCabe, C.N. Tomé, Toward understanding twin-twin interactions in hcp metals: Utilizing multiscale techniques to characterize deformation mechanisms in magnesium, Mater. Sci. Eng. A. 613 (2014) 365–371. https://doi.org/10.1016/j.msea.2014.06.062.

[57] S. Godet, L. Jiang, A.A. Luo, J.J. Jonas, Use of Schmid factors to select extension twin variants in extruded magnesium alloy tubes, 55 (2006) 1055–1058.

https://doi.org/10.1016/j.scriptamat.2006.07.059.

[58] S. Hong, S. Hyuk, C. Soo, Role of { 10 – 12 } twinning characteristics in the deformation behavior of a polycrystalline magnesium alloy, Acta Mater. 58 (2010) 5873–5885. https://doi.org/10.1016/j.actamat.2010.07.002.

[59] J. He, T. Liu, Y. Zhang, J. Tan, Twin characteristics and flow stress evolution in extruded magnesium alloy AZ31 subjected to multiple loads, J. Alloys Compd. 578 (2013) 536–542. https://doi.org/10.1016/j.jallcom.2013.07.001.

[60] Q. Yu, J. Wang, Y. Jiang, R.J. McCabe, N. Li, C.N. Tomé, Twin-twin interactions in magnesium, Acta Mater. 77 (2014) 28–42. https://doi.org/10.1016/j.actamat.2014.05.030.

[61] I.J. Beyerlein, R.J. McCabe, C.N. Tomé, Effect of microstructure on the nucleation of deformation twins in polycrystalline high-purity magnesium: A multi-scale modeling study, J. Mech. Phys. Solids. 59 (2011) 988–1003. https://doi.org/10.1016/j.jmps.2011.02.007.

[62] P. Chen, B. Li, D. Culbertson, Y. Jiang, Negligible effect of twin-slip interaction on hardening in deformation of a Mg-3Al-1Zn alloy, Mater. Sci. Eng. A. 729 (2018). https://doi.org/10.1016/j.msea.2018.05.067.

[63] C. Guillemer, M. Clavel, G. Cailletaud, Cyclic behavior of extruded magnesium : Experimental , microstructural and numerical approach, Int. J. Plast. 27 (2011) 2068–2084. https://doi.org/10.1016/j.ijplas.2011.06.002.

[64] Y. Xiong, Q. Yu, Y. Jiang, Cyclic deformation and fatigue of extruded AZ31B magnesium alloy under different strain ratios, Mater. Sci. Eng. A. 649 (2016) 93–

103. https://doi.org/10.1016/j.msea.2015.09.084.

[65] M.R. Barnett, Twinning and the ductility of magnesium alloys. Part I: “Tension” twins, Mater. Sci. Eng. A. 464 (2007) 1–7. https://doi.org/10.1016/j.msea.2006.12.037.

[66] L. Lu, J.W. Huang, D. Fan, B.X. Bie, T. Sun, K. Fezzaa, X.L. Gong, S.N. Luo, Anisotropic deformation of extruded magnesium alloy AZ31 under uniaxial compression: A study with simultaneous in situ synchrotron x-ray imaging and diffraction, Acta Mater. 120 (2016) 86–94. https://doi.org/10.1016/j.actamat.2016.08.029.

[67] Y. Xiong, Q. Yu, Y. Jiang, Deformation of extruded ZK60 magnesium alloy under uniaxial loading in different material orientations, Mater. Sci. Eng. A. 710 (2018) 206–213. https://doi.org/10.1016/j.msea.2017.10.059.

[68] S.H. Park, S. Hong, W. Bang, C.S. Lee, Effect of anisotropy on the low-cycle fatigue behavior of rolled AZ31 magnesium alloy, Mater. Sci. Eng. A. 527 (2010) 417–423. https://doi.org/10.1016/j.msea.2009.08.044.

[69] F. Lv, F. Yang, Q.Q. Duan, Y.S. Yang, S.D. Wu, S.X. Li, Z.F. Zhang, Fatigue properties of rolled magnesium alloy (AZ31) sheet: Influence of specimen orientation, Int. J. Fatigue. 33 (2011) 672–682. https://doi.org/10.1016/j.ijfatigue.2010.10.013.

[70] F. Lv, F. Yang, Q.Q. Duan, T.J. Luo, Y.S. Yang, S.X. Li, Z.F. Zhang, Tensile and low-cycle fatigue properties of Mg-2.8% Al-1.1% Zn-0.4% Mn alloy along the transverse and rolling directions, Scr. Mater. 61 (2009) 887–890.

https://doi.org/10.1016/j.scriptamat.2009.07.023.

[71] L. Carneiro, D. Culbertson, Q. Yu, Y. Jiang, Twinning in rolled AZ31B magnesium alloy under free-end torsion, Mater. Sci. Eng. A. 801 (2021) 140405. https://doi.org/10.1016/j.msea.2020.140405.

[72] Y. Wang, D. Culbertson, Y. Jiang, An experimental study of anisotropic fatigue behavior of rolled AZ31B magnesium alloy, Mater. Des. 186 (2020). https://doi.org/10.1016/j.matdes.2019.108266.

[73] S.H. Park, S. Hong, B. Ho Lee, W. Bang, C. Soo Lee, Low-cycle fatigue characteristics of rolled Mg–3Al–1Zn alloy, Int. J. Fatigue. 32 (2010) 1835–1842. https://doi.org/10.1016/j.ijfatigue.2010.05.002.

[74] P.A. Lynch, M. Kunz, N. Tamura, M.R. Barnett, Time and spatial resolution of slip and twinning in a grain embedded within a magnesium polycrystal, Acta Mater. 78 (2014) 203–212. https://doi.org/10.1016/j.actamat.2014.06.030.

[75] L. Jiang, J.J. Jonas, A.A. Luo, A.K. Sachdev, S. Godet, Influence of {10-12} extension twinning on the flow behavior of AZ31 Mg alloy, Mater. Sci. Eng. A. 445–446 (2007) 302–309. https://doi.org/10.1016/j.msea.2006.09.069.

[76] M. Knezevic, A. Levinson, R. Harris, R.K. Mishra, R.D. Doherty, S.R. Kalidindi, Deformation twinning in AZ31: Influence on strain hardening and texture evolution, Acta Mater. 58 (2010) 6230–6242. https://doi.org/10.1016/j.actamat.2010.07.041.

[77] H. Fan, S. Aubry, A. Arsenlis, J.A. El-Awady, The role of twinning deformation on the hardening response of polycrystalline magnesium from discrete dislocation dynamics simulations, Acta Mater. 92 (2015) 126–139.

https://doi.org/10.1016/j.actamat.2015.03.039.

[78] P.D. Wu, X.Q. Guo, H. Qiao, S.R. Agnew, D.J. Lloyd, J.D. Embury, On the rapid hardening and exhaustion of twinning in magnesium alloy, Acta Mater. 122 (2017) 369–377. https://doi.org/10.1016/j.actamat.2016.10.016.

[79] A.A. Salem, S.R. Kalidindi, R.D. Doherty, Strain hardening of titanium: Role of deformation twinning, Acta Mater. 51 (2003) 4225–4237. https://doi.org/10.1016/S1359-6454(03)00239-8.

[80] E.W. Kelley, F. Hosford, Plane-Strain Compression of Magnesium and Magnesium Alloy Crystals, Trans. Metall. Soc. AIME. 242 (1968) 5–13.

[81] X.Y. Lou, M. Li, R.K. Boger, S.R. Agnew, R.H. Wagoner, Hardening evolution of AZ31B Mg sheet, Int. J. Plast. 23 (2007) 44–86. https://doi.org/10.1016/j.ijplas.2006.03.005.

[82] R. Stevenson, J.. Vander Sande, The cyclic deformation of magnesium single crystals, Acta Metall. 22 (1974) 1079–1086.

[83] L. Song, B. Wu, L. Zhang, X. Du, Y. Wang, C. Esling, M.J. Philippe, Detwinning-related Bauschinger effect of an extruded magnesium alloy AZ31B, Mater. Charact. 148 (2019) 63–70. https://doi.org/10.1016/j.matchar.2018.12.005.

[84] A. Vinogradov, E. Vasilev, M. Linderov, D. Merson, In situ observations of the kinetics of twinning–detwinning and dislocation slip in magnesium, Mater. Sci. Eng. A. 676 (2016) 351–360. https://doi.org/10.1016/j.msea.2016.09.004.

[85] Q. Yu, J. Wang, Y. Jiang, Inverse Slip Accompanying Twinning and Detwinning during Cyclic Loading of Magnesium Single Crystal, J. Mater. 2013 (2013) 1–8.

https://doi.org/10.1155/2013/903786.

[86] C.H. Cáceres, T. Sumitomo, M. Veidt, Pseudoelastic behaviour of cast magnesium AZ91 alloy under cyclic loading-unloading, Acta Mater. 51 (2003) 6211–6218. https://doi.org/10.1016/S1359-6454(03)00444-0.

[87] L. Wang, G. Huang, Q. Quan, P. Bassani, E. Mostaed, M. Vedani, F. Pan, The effect of twinning and detwinning on the mechanical property of AZ31 extruded magnesium alloy during strain-path changes, Mater. Des. 63 (2014) 177–184. https://doi.org/10.1016/j.matdes.2014.05.056.

[88] W. Wu, S. Yeol, A.M. Paradowska, Y. Gao, P.K. Liaw, Twinning – detwinning behavior during fatigue-crack propagation in a wrought magnesium alloy AZ31B, Mater. Sci. Eng. A. 556 (2012) 278–286. https://doi.org/10.1016/j.msea.2012.06.088.

[89] D. Sarker, D.L. Chen, Dependence of compressive deformation on pre-strain and loading direction in an extruded magnesium alloy: Texture, twinning and de-twinning, Mater. Sci. Eng. A. 596 (2014) 134–144. https://doi.org/10.1016/j.msea.2013.12.038.

[90] Q. Yu, Y. Jiang, J. Wang, Cyclic deformation and fatigue damage in single-crystal magnesium under fully reversed strain-controlled tension-compression in the [1010] direction, Scr. Mater. 96 (2015) 41–44. https://doi.org/10.1016/j.scriptamat.2014.10.020.

[91] P. Chen, F. Wang, J. Ombogo, B. Li, Formation of 60° $\langle 01\bar{1}0 \rangle$ boundaries between $\{10\bar{1}2\}$ twin variants in deformation of a magnesium alloy, Mater. Sci. Eng.

A. 739 (2019) 173–185. https://doi.org/10.1016/j.msea.2018.10.029.

[92] A. Jager, A. Ostapovets, P. Molnár, P. Lejček, {[10$\bar{1}$2]}-{[10$\bar{1}$2]} Double Twinning in Magnesium, Philos. Mag. Lett. 91 (2011) 537–544. https://doi.org/10.1080/09500839.2011.593576.

[93] M.Z. Bian, K.S. Shin, {1012} Twinning Behavior in Magnesium Single Crystal, Met. Mater. Int. 19 (2013) 999–1004. https://doi.org/10.1007/s12540-013-5012-4.

[94] K.D. Molodov, T. Al-Samman, D.A. Molodov, G. Gottstein, Mechanisms of exceptional ductility of magnesium single crystal during deformation at room temperature: Multiple twinning and dynamic recrystallization, Acta Mater. 76 (2014) 314–330. https://doi.org/10.1016/j.actamat.2014.04.066.

[95] Z.Z. Shi, Y. Zhang, F. Wagner, T. Richeton, P.A. Juan, J.S. Lecomte, L. Capolungo, S. Berbenni, Sequential double extension twinning in a magnesium alloy: Combined statistical and micromechanical analyses, Acta Mater. 96 (2015) 333–343. https://doi.org/10.1016/j.actamat.2015.06.029.

[96] S. Mu, J.J. Jonas, G. Gottstein, Variant selection of primary, secondary and tertiary twins in a deformed Mg alloy, Acta Mater. 60 (2012) 2043–2053. https://doi.org/10.1016/j.actamat.2012.01.014.

[97] Y. Xin, M. Wang, Z. Zeng, M. Nie, Q. Liu, Strengthening and toughening of magnesium alloy by {1 0 -1 2} extension twins, Scr. Mater. 66 (2012) 25–28. https://doi.org/10.1016/j.scriptamat.2011.09.033.

[98] É. Martin, L. Capolungo, L. Jiang, J.J. Jonas, Variant selection during secondary twinning in Mg-3%Al, Acta Mater. 58 (2010) 3970–3983.

https://doi.org/10.1016/j.actamat.2010.03.027.

[99] J. Jain, J. Zou, C.W. Sinclair, W.J. Poole, Double tensile twinning in a Mg-8Al-0.5Zn alloy, J. Microsc. 242 (2011) 26–36. https://doi.org/10.1111/j.1365-2818.2010.03434.x.

[100] Q. Ma, H. El Kadiri, A.L. Oppedal, J.C. Baird, M.F. Horstemeyer, M. Cherkaoui, Twinning and double twinning upon compression of prismatic textures in an AM30 magnesium alloy, Scr. Mater. 64 (2011) 813–816. https://doi.org/10.1016/j.scriptamat.2011.01.003.

[101] T. Al-Samman, G. Gottstein, Room temperature formability of a magnesium AZ31 alloy: Examining the role of texture on the deformation mechanisms, Mater. Sci. Eng. A. 488 (2008) 406–414. https://doi.org/10.1016/j.msea.2007.11.056.

[102] D. Ando, J. Koike, Y. Sutou, Relationship between deformation twinning and surface step formation in AZ31 magnesium alloys, Acta Mater. 58 (2010) 4316–4324. https://doi.org/10.1016/j.actamat.2010.03.044.

[103] M. Lentz, M. Risse, N. Schaefer, W. Reimers, I.J. Beyerlein, Strength and ductility with {10 11}-{1012} double twinning in a magnesium alloy, Nat. Commun. 7 (2016) 1–7. https://doi.org/10.1038/ncomms11068.

[104] I.J. Beyerlein, J. Wang, M.R. Barnett, C.N. Tomé, Double twinning mechanisms in magnesium alloys via dissociation of lattice dislocations, Proc. R. Soc. A Math. Phys. Eng. Sci. 468 (2012) 1496–1520. https://doi.org/10.1098/rspa.2011.0731.

[105] M.R. Barnett, Z. Keshavarz, A.G. Beer, X. Ma, Non-Schmid behaviour during secondary twinning in a polycrystalline magnesium alloy, Acta Mater. 56 (2008) 5–

15. https://doi.org/10.1016/j.actamat.2007.08.034.

[106] T. Al-Samman, K.D. Molodov, D.A. Molodov, G. Gottstein, S. Suwas, Softening and dynamic recrystallization in magnesium single crystals during c-axis compression, Acta Mater. 60 (2012) 537–545. https://doi.org/10.1016/j.actamat.2011.10.013.

[107] S. Yi, I. Schestakow, S. Zaefferer, Twinning-related microstructural evolution during hot rolling and subsequent annealing of pure magnesium, Mater. Sci. Eng. A. 516 (2009) 58–64. https://doi.org/10.1016/j.msea.2009.03.015.

[108] A.G. Crocker, Double twinning, Philos. Mag. 7 (1962) 1901–1924. https://doi.org/10.1080/14786436208213854.

[109] R.E. Reed-Hill, W.D. Robertson, The crystallographic characteristics of fracture in magnesium single crystals, Acta Metall. 5 (1957) 728–737. https://doi.org/10.1016/0001-6160(57)90075-5.

[110] J. Koike, Y. Sato, D. Ando, Origin of the anomalous {10$\bar{1}$2} twinning during tensile deformation of mg alloy sheet, Mater. Trans. 49 (2008) 2792–2800. https://doi.org/10.2320/matertrans.MRA2008283.

[111] M.R. Barnett, Twinning and the ductility of magnesium alloys. Part II. “Contraction” twins, Mater. Sci. Eng. A. 464 (2007) 8–16. https://doi.org/10.1016/j.msea.2007.02.109.

[112] Q. Yu, Cyclic Plastic Deformation, Fatigue, and the Associated Micro-Mechanisms in Magnesium: from Single Crystal to Polycrystal, University of Nevada, Reno, 2014. https://doi.org/10.1080/14768320500230185.

[113] Q. Yu, Y. Jiang, J. Wang, Tension-compression-tension tertiary twins in coarse-grained polycrystalline pure magnesium at room temperature, Philos. Mag. Lett. 95 (2015) 194–201. https://doi.org/10.1080/09500839.2015.1022621.

[114] M.D. Nave, M.R. Barnett, Microstructures and textures of pure magnesium deformed in plane-strain compression, Scr. Mater. 51 (2004) 881–885. https://doi.org/10.1016/j.scriptamat.2004.07.002.

[115] Q. Yu, J. Wang, Y. Jiang, R.J. McCabe, C.N. Tomé, Co-zone (1012) twin interaction in magnesium single crystal, Mater. Res. Lett. 2 (2014) 82–88. https://doi.org/10.1080/21663831.2013.867291.

[116] E. Roberts, P.G. Partridge, The accommodation around {10-12}<-1011> twins in magnesium, Acta Metall. 14 (1966) 513–527.

[117] M. Gong, S. Xu, Y. Jiang, Y. Liu, J. Wang, Structural characteristics of {1¯012} non-cozone twin-twin interactions in magnesium, Acta Mater. 159 (2018) 65–76. https://doi.org/10.1016/j.actamat.2018.08.004.

[118] X. Yang, L. Zhang, Twinning and twin intersection in AZ31 Mg alloy during warm deformation, Acta Metall. Sin. 45 (2009) 1303–1308.

[119] H. El Kadiri, J. Kapil, A.L. Oppedal, L.G. Hector, S.R. Agnew, M. Cherkaoui, S.C. Vogel, The effect of twin-twin interactions on the nucleation and propagation of { 1 0 1¯ 2 } twinning in magnesium, Acta Mater. 61 (2013) 3549–3563. https://doi.org/10.1016/j.actamat.2013.02.030.

[120] B.E. Reed-Hill, E.R. Buchanan, Zig-zag twins in zirconium, Acta Metall. 11 (1963) 73–75. https://doi.org/10.1016/0001-6160(63)90133-0.

[121] S.H. Park, S.G. Hong, J.H. Lee, C.S. Lee, Multiple twinning modes in rolled Mg-3Al-1Zn alloy and their selection mechanism, Mater. Sci. Eng. A. 532 (2012) 401–406. https://doi.org/10.1016/j.msea.2011.11.003.

[122] Q. Ma, H. El Kadiri, A.L. Oppedal, J.C. Baird, B. Li, M.F. Horstemeyer, S.C. Vogel, Twinning effects in a rod-textured AM30 Magnesium alloy, Int. J. Plast. 29 (2012) 60–76. https://doi.org/10.1016/j.ijplas.2011.08.001.

[123] A.L. Oppedal, H. El Kadiri, C.N. Tomé, G.C. Kaschner, S.C. Vogel, J.C. Baird, M.F. Horstemeyer, Effect of dislocation transmutation on modeling hardening mechanisms by twinning in magnesium, Int. J. Plast. 30–31 (2012) 41–61. https://doi.org/10.1016/j.ijplas.2011.09.002.

[124] N. Ecob, B. Ralph, The effect of grain size on deformation twinning in a textured zinc alloy, J. Mater. Sci. 18 (1983) 2419–2429. https://doi.org/10.1007/BF00541848.

[125] L. Wang, P. Eisenlohr, Y. Yang, T.R. Bieler, M.A. Crimp, Nucleation of paired twins at grain boundaries in titanium, Scr. Mater. 63 (2010) 827–830. https://doi.org/10.1016/j.scriptamat.2010.06.027.

[126] R. Xin, C. Guo, Z. Xu, G. Liu, X. Huang, Q. Liu, Characteristics of long {10-12} twin bands in sheet rolling of a magnesium alloy, Scr. Mater. 74 (2014) 96–99. https://doi.org/10.1016/j.scriptamat.2013.11.008.

[127] H. Chen, T. Liu, D. Hou, D. Shi, Study on the paired twinning behavior in a hot rolled AZ31 magnesium alloy via interrupted in situ compression, Mater. Sci. Eng. A. 667 (2016) 402–408. https://doi.org/10.1016/j.msea.2016.05.006.

[128] D. Shi, T. Liu, T. Wang, D. Hou, S. Zhao, S. Hussain, {10–12} Twins across twin boundaries traced by in situ EBSD, J. Alloys Compd. 690 (2017) 699–706. https://doi.org/10.1016/j.jallcom.2016.08.076.

[129] G. Liu, R. Xin, F. Liu, Q. Liu, Twinning characteristic in tension of magnesium alloys and its effect on mechanical properties, Mater. Des. 107 (2016) 503–510. https://doi.org/10.1016/j.matdes.2016.06.073.

[130] C. Guo, R. Xin, J. Xu, B. Song, Q. Liu, Strain compatibility effect on the variant selection of connected twins in magnesium, Mater. Des. 76 (2015) 71–76. https://doi.org/10.1016/j.matdes.2015.03.041.

[131] C. Guo, R. Xin, C. Ding, B. Song, Q. Liu, Understanding of variant selection and twin patterns in compressed Mg alloy sheets via combined analysis of Schmid factor and strain compatibility factor, Mater. Sci. Eng. A. 609 (2014) 92–101. https://doi.org/10.1016/j.msea.2014.04.103.

[132] Z.Z. Shi, Compound cross-grain boundary extension twin structure and its related twin variant selection in a deformed Mg alloy, J. Alloys Compd. 716 (2017) 128–136. https://doi.org/10.1016/j.jallcom.2017.05.020.

[133] I.J.J. Beyerlein, L. Capolungo, P.E.E. Marshall, R.J.J. McCabe, C.N. Tomé, C.N. Tome, Statistical analyses of deformation twinning in magnesium, Philos. Mag. 90 (2010) 2161–2190. https://doi.org/10.1080/14786431003630835.

[134] M. Arul Kumar, I.J. Beyerlein, R.J. McCabe, C.N. Tomé, Grain neighbour effects on twin transmission in hexagonal close-packed materials, Nat. Commun. 7 (2016) 1–9. https://doi.org/10.1038/ncomms13826.

[135] S. Xu, T.M. Liu, Y. Zhang, J.J. He, W. Zeng, J.X. Wang, Continuation of twins across grain boundary in extruded Mg-3Al-1Zn alloy, Mater. Sci. Technol. (United Kingdom). 29 (2013) 1144–1147. https://doi.org/10.1179/1743284713Y.0000000266.

[136] J. Luster, M.A. Morris, Compatibility of deformation in two-phase Ti-Al alloys: Dependence on microstructure and orientation relationships, Metall. Mater. Trans. A. 26 (1995) 1745–1756. https://doi.org/10.1007/BF02670762.

[137] A. Akhtar, E. Teghtsoonian, Solid solution strengthening of magnesium single crystals-I alloying behaviour in basal slip, Acta Metall. 17 (1969) 1339–1349. https://doi.org/10.1016/0001-6160(69)90151-5.

[138] H. Yoshinaga, R. Horiuchi, Work Hardening Characteristics of the Basal Slip of Magnesium Single Crystals, Trans. Japan Inst. Met. 3 (1962) 220–226. https://doi.org/10.2320/matertrans1960.3.220.

[139] H. Yoshinaga, R. Horiuchi, On the Nonbasal Slip in Magnesium Crystals, Trans. Japan Inst. Met. 5 (1964) 14–21. https://doi.org/10.2320/matertrans1960.5.14.

[140] P.B. Hirsch, J.S. Lally, The deformation of magnesium single crystals, Philos. Mag. 12 (1965) 595–648. https://doi.org/10.1080/14786436508218903.

[141] S. Ando, H. Tonda, Non-Basal Slips in Magnesium and Magnesium-Lithium Alloy Single Crystals, Mater. Sci. Forum. 350–351 (2000) 43–48. https://doi.org/10.4028/www.scientific.net/MSF.350-351.65.

[142] T. Kitahara, S. Ando, M. Tsushida, H. Kitahara, H. Tonda, Deformation behavior of magnesium single crystals in C-axis compression, Key Eng. Mater. 345-346 I (2007)

129–132. https://doi.org/10.4028/www.scientific.net/kem.345-346.129.

[143] S. Ando, M. Tsushida, H. Kitahara, Deformation behavior of magnesium single crystal in c-axis compression and a-axis tension, Mater. Sci. Forum. 654–656 (2010) 699–702. https://doi.org/10.4028/www.scientific.net/MSF.654-656.699.

[144] B. Syed, J. Geng, R.K. Mishra, K.S. Kumar, [0 0 0 1] Compression response at room temperature of single-crystal magnesium, Scr. Mater. 67 (2012) 700–703. https://doi.org/10.1016/j.scriptamat.2012.06.036.

[145] Q. Li, Microstructure and deformation mechanism of 0001 magnesium single crystal subjected to quasistatic and high-strain-rate compressiveloadings, Mater. Sci. Eng. A. 568 (2013) 96–101. https://doi.org/10.1016/j.msea.2013.01.028.

[146] S. Wang, H. Pan, A. He, P. Wang, F. Zhang, Amorphous structure in single-crystal magnesium under compression along the c axis with ultrahigh strain rate, Phys. Rev. B. 100 (2019) 1–8. https://doi.org/10.1103/PhysRevB.100.214106.

[147] J.H. Shin, S.H. Kim, T.K. Ha, K.H. Oh, I.S. Choi, H.N. Han, Nanoindentation study for deformation twinning of magnesium single crystal, Scr. Mater. 68 (2013) 483–486. https://doi.org/10.1016/j.scriptamat.2012.11.030.

[148] B.Y. Liu, J. Wang, B. Li, L. Lu, X.Y. Zhang, Z.W. Shan, J. Li, C.L. Jia, J. Sun, E. Ma, Twinning-like lattice reorientation without a crystallographic twinning plane, Nat. Commun. 5 (2014). https://doi.org/10.1038/ncomms4297.

[149] N. Dixit, L. Farbaniec, K.T. Ramesh, Twinning in single crystal Mg under microsecond impact along the (a) axis, Mater. Sci. Eng. A. 693 (2017) 22–25. https://doi.org/10.1016/j.msea.2017.03.074.

[150] V. Kannan, K. Hazeli, K.T. Ramesh, The mechanics of dynamic twinning in single crystal magnesium, J. Mech. Phys. Solids. 120 (2018) 154–178. https://doi.org/10.1016/j.jmps.2018.03.010.

[151] R. Kwadjo, L.M. Brown, Cyclic hardening of magnesium single crystals, Acta Metall. 26 (1978) 1117–1132. https://doi.org/10.1016/0001-6160(78)90139-6.

[152] Q. Li, Fatigue behavior and microstructure of 0001 and 1^{-} 014 magnesium single crystals under compression – compression cyclic loading, Mater. Sci. Eng. A. 556 (2012) 301–308. https://doi.org/10.1016/j.msea.2012.06.091.

[153] N.M. Della Ventura, S. Kalácska, D. Casari, T.E.J. Edwards, A. Sharma, J. Michler, R. Logé, X. Maeder, {$101^{-}2$} twinning mechanism during in situ micro-tensile loading of pure Mg: Role of basal slip and twin-twin interactions, Mater. Des. 197 (2021) 109206. https://doi.org/10.1016/j.matdes.2020.109206.

[154] K.E. Prasad, K. Rajesh, U. Ramamurty, Micropillar and macropillar compression responses of magnesium single crystals oriented for single slip or extension twinning, Acta Mater. 65 (2014) 316–325. https://doi.org/10.1016/j.actamat.2013.10.073.

[155] K.D. Molodov, T. Al-Samman, D.A. Molodov, S. Korte-Kerzel, On the twinning shear of {$101^{-}2$} twins in magnesium – Experimental determination and formal description, Acta Mater. 134 (2017) 267–273. https://doi.org/10.1016/j.actamat.2017.05.041.

[156] K.E. Prasad, K.T. Ramesh, In-situ observations and quantification of twin boundary mobility in polycrystalline magnesium, Mater. Sci. Eng. A. 617 (2014) 121–126.

https://doi.org/10.1016/j.msea.2014.08.043.

[157] N. Dixit, L. Farbaniec, K.T. Ramesh, Twinning in single crystal Mg under microsecond impact along the (a) axis, Mater. Sci. Eng. A. 693 (2017) 22–25. https://doi.org/10.1016/j.msea.2017.03.074.

[158] J. Bauschinger, Changes of the elastic limit and the modulus of elasticity on various metals, Zivilingenieur. 27 (1881) 289–348.

[159] J.B. Jordon, M.F. Horstemeyer, K. Solanki, Y. Xue, Damage and stress state influence on the Bauschinger effect in aluminum alloys, Mech. Mater. 39 (2007) 920–931. https://doi.org/10.1016/j.mechmat.2007.03.004.

[160] I. Karaman, H. Sehitoglu., Y.I. Chumlyakov, H.J. Maier, I. V. Kireeva, The effect of twinning and slip on the bauschinger effect of hadfield steel single crystals, Metall. Mater. Trans. A Phys. Metall. Mater. Sci. 32 (2001) 695–706. https://doi.org/10.1007/s11661-001-1005-x.

[161] A.A. Mamun, R.J. Moat, J. Kelleher, P.J. Bouchard, Origin of the Bauschinger effect in a polycrystalline material, Mater. Sci. Eng. A. 707 (2017) 576–584. https://doi.org/10.1016/j.msea.2017.09.091.

[162] E. Demir, D. Raabe, Mechanical and microstructural single-crystal Bauschinger effects: Observation of reversible plasticity in copper during bending, Acta Mater. 58 (2010) 6055–6063. https://doi.org/10.1016/j.actamat.2010.07.023.

[163] J.K. Mahato, P.S. De, A. Sarkar, A. Kundu, P.C. Chakraborti, Effect of deformation mode and grain size on Bauschinger behavior of annealed copper, Int. J. Fatigue. 83 (2015) 42–52. https://doi.org/10.1016/j.ijfatigue.2015.04.023.

[164] L. Wu, S.R. Agnew, D.W. Brown, G.M. Stoica, B. Clausen, A. Jain, D.E. Fielden, P.K. Liaw, Internal stress relaxation and load redistribution during the twinning-detwinning-dominated cyclic deformation of a wrought magnesium alloy, ZK60A, Acta Mater. 56 (2008) 3699–3707. https://doi.org/10.1016/j.actamat.2008.04.006.

[165] Q. Sun, A. Ostapovets, X. Zhang, L. Tan, Q. Liu, Investigation of twin–twin interaction in deformed magnesium alloy, Philos. Mag. 98 (2018) 741–751. https://doi.org/10.1080/14786435.2017.1417648.

[166] Q. Sun, X.Y. Zhang, Y. Ren, L. Tan, J. Tu, Observations on the intersection between {101¯2} twin variants sharing the same zone axis in deformed magnesium alloy, Mater. Charact. 109 (2015) 160–163. https://doi.org/10.1016/j.matchar.2015.09.024.

[167] M. Arul Kumar, M. Gong, I.J. Beyerlein, J. Wang, C.N. Tomé, Role of local stresses on co-zone twin-twin junction formation in HCP magnesium, Acta Mater. 168 (2019) 353–361. https://doi.org/10.1016/j.actamat.2019.02.037.

[168] H. Chen, T. Liu, S. Xiang, Y. Liang, Abnormal migration of twin boundaries in rolled AZ31 alloy containing intersecting {101¯2} extension twins, J. Alloys Compd. 690 (2017) 376–380. https://doi.org/10.1016/j.jallcom.2016.08.154.

[169] M. Gong, W. Wu, Atomic-level study of twin-twin interactions in hexagonal metals, J. Mater. Res. 35 (2020) 1647–1659. https://doi.org/10.1557/jmr.2020.65.

[170] D. Sarker, J. Friedman, D.L. Chen, De-twinning and Texture Change in an Extruded AM30 Magnesium Alloy during Compression along Normal Direction, J. Mater. Sci. Technol. 31 (2015) 264–268. https://doi.org/10.1016/j.jmst.2014.11.018.

[171] H. Watanabe, A. Takara, H. Somekawa, T. Mukai, K. Higashi, Effect of texture on tensile properties at elevated temperatures in an AZ31 magnesium alloy, Scr. Mater. 52 (2005) 449–454. https://doi.org/10.1016/j.scriptamat.2004.11.011.

[172] S.B. Yi, C.H.J. Davies, H.G. Brokmeier, R.E. Bolmaro, K.U. Kainer, J. Homeyer, Deformation and texture evolution in AZ31 magnesium alloy during uniaxial loading, Acta Mater. 54 (2006) 549–562. https://doi.org/10.1016/j.actamat.2005.09.024.

[173] J. Jiang, A. Godfrey, W. Liu, Q. Liu, Microtexture evolution via deformation twinning and slip during compression of magnesium alloy AZ31, Mater. Sci. Eng. A. 483–484 (2008) 576–579. https://doi.org/10.1016/j.msea.2006.07.175.

[174] J. Jiang, A. Godfrey, W. Liu, Q. Liu, Identification and analysis of twinning variants during compression of a Mg-Al-Zn alloy, Scr. Mater. 58 (2008) 122–125. https://doi.org/10.1016/j.scriptamat.2007.09.047.

[175] Y. Chino, K. Kimura, M. Hakamada, M. Mabuchi, Mechanical anisotropy due to twinning in an extruded AZ31 Mg alloy, Mater. Sci. Eng. A. 485 (2008) 311–317. https://doi.org/10.1016/j.msea.2007.07.076.

[176] J. Sun, L. Jin, S. Dong, Z. Zhang, J. Dong, Asymmetry strain hardening behavior in Mg-3%Al-1%Zn and Mg-8%Gd-3%Y alloy tubes, Mater. Lett. 107 (2013) 197–201. https://doi.org/10.1016/j.matlet.2013.06.007.

[177] D. Sarker, J. Friedman, D.L. Chen, Twin growth and texture evolution in an extruded AM30 magnesium alloy during compression, J. Mater. Sci. Technol. 30 (2014) 884–887. https://doi.org/10.1016/j.jmst.2014.06.011.

[178] L. Wu, S.R. Agnew, Y. Ren, D.W. Brown, B. Clausen, G.M. Stoica, H.R. Wenk, P.K. Liaw, The effects of texture and extension twinning on the low-cycle fatigue behavior of a rolled magnesium alloy, AZ31B, Mater. Sci. Eng. A. 527 (2010) 7057–7067. https://doi.org/10.1016/j.msea.2010.07.047.

[179] M. Huppmann, M. Lentz, S. Chedid, W. Reimers, Analyses of deformation twinning in the extruded magnesium alloy AZ31 after compressive and cyclic loading, J. Mater. Sci. 46 (2011) 938–950. https://doi.org/10.1007/s10853-010-4838-0.

[180] Q. Yu, J. Zhang, Y. Jiang, Q. Li, An experimental study on cyclic deformation and fatigue of extruded ZK60 magnesium alloy, Int. J. Fatigue. 36 (2012) 47–58. https://doi.org/10.1016/j.ijfatigue.2011.08.016.

[181] S. Dong, Q. Yu, Y. Jiang, J. Dong, F. Wang, W. Ding, Electron backscatter diffraction observations of twinning-detwinning evolution in a magnesium alloy subjected to large strain amplitude cyclic loading, Mater. Des. 65 (2015) 762–765. https://doi.org/10.1016/j.matdes.2014.09.079.

[182] G. Proust, C.N. Tomé, A. Jain, S.R. Agnew, Modeling the effect of twinning and detwinning during strain-path changes of magnesium alloy AZ31, Int. J. Plast. 25 (2009) 861–880. https://doi.org/10.1016/j.ijplas.2008.05.005.

[183] F. Mokdad, D.L. Chen, D.Y. Li, Twin-twin interactions and contraction twin formation in an extruded magnesium alloy subjected to an alteration of compressive direction, J. Alloys Compd. 737 (2018) 549–560. https://doi.org/10.1016/j.jallcom.2017.12.043.

[184] J. He, T. Liu, S. Xu, Y. Zhang, The effects of compressive pre-deformation on yield

asymmetry in hot-extruded Mg-3Al-1Zn alloy, Mater. Sci. Eng. A. 579 (2013) 1–8. https://doi.org/10.1016/j.msea.2013.04.115.

[185] Y. Xin, J. Jiang, A. Chapuis, M. Wang, Q. Liu, Plastic deformation behavior of AZ31 magnesium alloy under multiple passes cross compression, Mater. Sci. Eng. A. 532 (2012) 50–57. https://doi.org/10.1016/j.msea.2011.10.061.

[186] B. Song, R. Xin, Y. Liang, G. Chen, Q. Liu, Twinning characteristic and variant selection in compression of a pre-side-rolled Mg alloy sheet, Mater. Sci. Eng. A. 614 (2014) 106–115. https://doi.org/10.1016/j.msea.2014.07.026.

[187] D. Sarker, J. Friedman, D.L. Chen, Influence of pre-strain on de-twinning activity in an extruded AM30 magnesium alloy, Mater. Sci. Eng. A. 605 (2014) 73–79. https://doi.org/10.1016/j.msea.2014.03.046.

[188] Z. Long, T. Liu, Y. Wu, Y. Zhang, Improving the anisotropy of rolled Mg-3Al-1Zn alloy by pre-strain and annealing, Mater. Sci. Eng. A. 616 (2014) 240–245. https://doi.org/10.1016/j.msea.2014.08.005.

[189] D. Sarker, J. Friedman, D.L. Chen, Influence of pre-deformation and subsequent annealing on strain hardening and anisotropy of AM30 magnesium alloy, J. Alloys Compd. 611 (2014) 341–350. https://doi.org/10.1016/j.jallcom.2014.05.133.

[190] A. Chapuis, Y. Xin, X. Zhou, Q. Liu, {10-12} Twin variants selection mechanisms during twinning, re-twinning and detwinning, Mater. Sci. Eng. A. 612 (2014) 431–439. https://doi.org/10.1016/j.msea.2014.06.088.

[191] B. Song, R. Xin, X. Zheng, G. Chen, Q. Liu, Activation of multiple twins by pre-tension and compression to enhance the strength of Mg-3Al-1Zn alloy plates, Mater.

Sci. Eng. A. 621 (2015) 100–104. https://doi.org/10.1016/j.msea.2014.10.061.

[192] C. Lou, X. Zhang, R. Wang, Q. Liu, Mechanical behavior and microstructural characteristics of magnesium alloy containing {10-12} twin lamellar structure, J. Mater. Res. 28 (2013) 733–739. https://doi.org/10.1557/jmr.2012.394.

[193] S.-F. Chen, L. Zheng, S.-H. Zhang, H.-W. Song, M. Cheng, Deformation Mechanism of AZ31B Magnesium Alloy Under Different Loading Paths, Acta Metall. Sin. (English Lett. 28 (2015) 1426–1434. https://doi.org/10.1007/s40195-015-0342-5.

[194] J.Y. Kang, B. Bacroix, R. Brenner, Evolution of microstructure and texture during planar simple shear of magnesium alloy, Scr. Mater. 66 (2012) 654–657. https://doi.org/10.1016/j.scriptamat.2012.01.040.

[195] H. Zhang, G. Huang, L. Wang, H.J. Roven, Z. Xu, F. Pan, Improved ductility of magnesium alloys by a simple shear process followed by annealing, Scr. Mater. 69 (2013) 49–52. https://doi.org/10.1016/j.scriptamat.2013.03.011.

[196] A.S. Khan, A. Pandey, T. Gnäupel-Herold, R.K. Mishra, Mechanical response and texture evolution of AZ31 alloy at large strains for different strain rates and temperatures, Int. J. Plast. 27 (2011) 688–706. https://doi.org/10.1016/j.ijplas.2010.08.009.

[197] H. Pan, F. Wang, M. Feng, L. Jin, J. Dong, P. Wu, Mechanical behavior and microstructural evolution in rolled Mg-3Al-1Zn-0.5Mn alloy under large strain simple shear, Mater. Sci. Eng. A. 712 (2018) 585–591. https://doi.org/10.1016/j.msea.2017.11.123.

[198] B. Beausir, L.S. Tóth, F. Qods, K.W. Neale, Texture and mechanical behavior of magnesium during free-end torsion, J. Eng. Mater. Technol. Trans. ASME. 131 (2009) 0111081–01110815. https://doi.org/10.1115/1.3030973.

[199] B. Song, C. Wang, N. Guo, H. Pan, R. Xin, Improving tensile and compressive properties of an extruded AZ91 rod by the combined use of torsion deformation and aging treatment, Materials (Basel). 10 (2017) 3–8. https://doi.org/10.3390/ma10030280.

[200] N. Guo, B. Song, C. Guo, R. Xin, Q. Liu, Improving tensile and compressive properties of magnesium alloy rods via a simple pre-torsion deformation, Mater. Des. 83 (2015) 270–275. https://doi.org/10.1016/j.matdes.2015.06.071.

[201] J. Wang, X.Y. Yang, Y. Li, Z.Y. Xiao, D.X. Zhang, T. Sakai, Enhanced ductility and reduced asymmetry of Mg-2Al-1Zn alloy plate processed by torsion and annealing, Trans. Nonferrous Met. Soc. China (English Ed. 25 (2015) 3928–3935. https://doi.org/10.1016/S1003-6326(15)64040-7.

[202] F. Kabirian, A.S. Khan, T. Gnäupel-Herlod, Visco-plastic modeling of mechanical responses and texture evolution in extruded AZ31 magnesium alloy for various loading conditions, Int. J. Plast. 68 (2015) 1–20. https://doi.org/10.1016/j.ijplas.2014.10.012.

[203] B. Song, N. Guo, R. Xin, H. Pan, C. Guo, Strengthening and toughening of extruded magnesium alloy rods by combining pre-torsion deformation with subsequent annealing, Mater. Sci. Eng. A. 650 (2016) 300–304. https://doi.org/10.1016/j.msea.2015.10.069.

[204] P.D. Wu, H. Wang, K.W. Neale, On the large strain torsion of HCP polycrystals, Int. J. Appl. Mech. 4 (2012) 1–27. https://doi.org/10.1142/S175882511250024X.

[205] J. Hu, H. Gao, Y. Meng, Z. Zhang, L. Gao, Effects of free-end torsion on the microstructure evolution and fatigue properties in an extruded AZ31 rod, Mater. Sci. Eng. A. 726 (2018) 215–222. https://doi.org/10.1016/j.msea.2018.04.078.

[206] A.A. Roostaei, H. Jahed, Multiaxial cyclic behaviour and fatigue modelling of AM30 Mg alloy extrusion, Int. J. Fatigue. 97 (2017) 150–161. https://doi.org/10.1016/j.ijfatigue.2016.12.037.

[207] D. Toscano, S.B. Behravesh, S.K. Shaha, H. Jahed, B. Williams, Characterization of closed-die forged AZ31B under pure axial and pure shear loading, Int. J. Fatigue. 139 (2020) 105754. https://doi.org/10.1016/j.ijfatigue.2020.105754.

[208] A. Gryguć, S.B. Behravesh, S.K. Shaha, H. Jahed, M. Wells, B. Williams, X. Su, Multiaxial cyclic behaviour of extruded and forged AZ80 Mg alloy, Int. J. Fatigue. 127 (2019) 324–337. https://doi.org/10.1016/j.ijfatigue.2019.06.015.

[209] S. Biswas, B. Beausir, L.S. Toth, S. Suwas, Evolution of texture and microstructure during hot torsion of a magnesium alloy, Acta Mater. 61 (2013) 5263–5277. https://doi.org/10.1016/j.actamat.2013.05.018.

[210] X.Q. Guo, W. Wu, P.D. Wu, H. Qiao, K. An, P.K. Liaw, On the Swift effect and twinning in a rolled magnesium alloy under free-end torsion, Scr. Mater. 69 (2013) 319–322. https://doi.org/10.1016/j.scriptamat.2013.05.010.

[211] J. Wang, D. Zhang, Y. Li, Z. Xiao, J. Fouse, X. Yang, Effect of initial orientation on the microstructure and mechanical properties of textured AZ31 Mg alloy during

torsion and annealing, Mater. Des. 86 (2015) 526–535. https://doi.org/10.1016/j.matdes.2015.07.113.

[212] B. Beausir, L.S. Tóth, K.W. Neale, Ideal orientations and persistence characteristics of hexagonal close packed crystals in simple shear, Acta Mater. 55 (2007) 2695–2705. https://doi.org/10.1016/j.actamat.2006.12.021.

[213] H.W. Swift, Length changes in metals under torsional overstrain, Engineering. 163 (1947) 253.

[214] K.D. Molodov, T. Al-Samman, D.A. Molodov, G. Gottstein, On the role of anomalous twinning in the plasticity of magnesium, Acta Mater. 103 (2016) 711–723. https://doi.org/10.1016/j.actamat.2015.10.043.

[215] D. Liu, R. Xin, Y. Hongni, Z. Liu, X. Zheng, Q. Liu, Comparative examinations on the activity and variant selection of twinning during tension and compression of magnesium alloys, Mater. Sci. Eng. A. 658 (2016) 229–237. https://doi.org/10.1016/j.msea.2016.01.098.

[216] S.F. Chen, H.W. Song, S.H. Zhang, M. Cheng, C. Zheng, M.G. Lee, An effective Schmid factor in consideration of combined normal and shear stresses for slip/twin variant selection of Mg-3Al-1Zn alloy, Scr. Mater. 167 (2019) 51–55. https://doi.org/10.1016/j.scriptamat.2019.03.026.

[217] D. Xia, X. Chen, G. Huang, B. Jiang, A. Tang, H. Yang, S. Gavras, Y. Huang, N. Hort, F. Pan, Calculation of Schmid factor in Mg alloys: Influence of stress state, Scr. Mater. 171 (2019) 31–35. https://doi.org/10.1016/j.scriptamat.2019.06.014.

[218] G.M. Hommer, A.L. Pilchak, A.P. Stebner, Normalized resolved shear stress

calculations for single crystals subjected to multiaxial loading, Materialia. 2 (2018) 53–57. https://doi.org/10.1016/j.mtla.2018.06.009.

[219] E. Schmid, W. Boas, Plasticity of Crystals, F.A. Hughes & Co., London, 1950.

[220] T.B. Britton, J. Jiang, Y. Guo, A. Vilalta-clemente, D. Wallis, L.N. Hansen, A. Winkelmann, A.J. Wilkinson, Tutorial : Crystal orientations and EBSD — Or which way is up?, Mater. Charact. 117 (2016) 113–126. https://doi.org/10.1016/j.matchar.2016.04.008.

[221] M. Niewczas, Lattice correspondence during twinning in hexagonal close-packed crystals, Acta Mater. 58 (2010) 5848–5857. https://doi.org/10.1016/j.actamat.2010.06.059.

Duke Culbertson's Publications

1) L. Carneiro, **D. Culbertson**, X. Zhu, Q. Yu, Y. Jiang, Twinning Characteristics in rolled AZ31B magnesium alloy under three stress states, Mater. Charact. 175 (2021) 111050
2) L. Carneiro, **D. Culbertson**, Q. Yu, Y. Jiang, Twinning in rolled AZ31B magnesium alloy under free-end torsion, Mater. Sci. Eng. A. 801 (2021) 140405. https://doi.org/10.1016/j.msea.2020.140405
3) **D. Culbertson**, Q. Yu, Y. Jiang, On the intrusion-like co-zone twin-twin structure: an in situ observation, Mater. Lett. 286 (2020) 129140. https://doi.org/10.1016/j.matlet.2020.129140
4) Y. Wang, **D. Culbertson**, Y. Jiang, An experimental study of anisotropic fatigue behavior of rolled AZ31B magnesium alloy, Mater. Des. 186 (2020). https://doi.org/10.1016/j.matdes.2019.108266
5) **D. Culbertson**, Q. Yu, Y. Jiang, In situ observation of cross-grain twin pair formation in pure magnesium, Philos. Mag. Lett. 98 (2018) 139–146. https://doi.org/10.1080/09500839.2018.14985992.
6) P. Chen, B. Li, **D. Culbertson**, Y. Jiang, Negligible effect of twin-slip interaction on hardening in deformation of a Mg-3Al-1Zn alloy, Mater. Sci. Eng. A. 729 (2018) 285–293

7) P. Chen, B. Li, **D. Culbertson**, Y. Jiang, Contribution of extension twinning to plastic strain at low stress stage deformation of a Mg-3Al-1Zn alloy, Mater. Sci. Eng. A. 709 (2018) 40–45

8) **D. Culbertson**, Q. Yu, J. Wang, Y. Jiang, Pre-compression effect on microstructure evolution of extruded pure polycrystalline magnesium during reversed tension load, Mater. Charact. 134 (2017) 41–48. https://doi.org/10.1016/j.matchar.2017.10.003

9) **D. Culbertson**, Y. Jiang, An experimental study of the orientation effect on fatigue crack propagation in rolled AZ31B magnesium alloy, Mater. Sci. Eng. A. 676 (2016). https://doi.org/10.1016/j.msea.2016.08.088